Sediment Mobility Modelling and Hydrodynamic Properties of Maerl

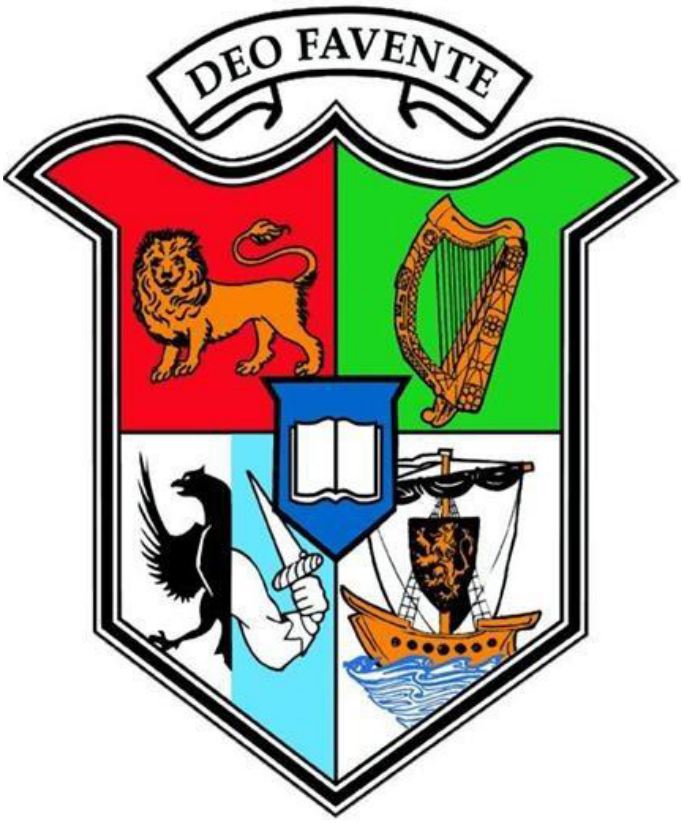

Siddhi Joshi MSc BSc (Hons)

Supervisors: Prof. Colin Brown, Dr. Garret Duffy

A thesis submitted for the degree Doctor of Philosophy (PhD)

Earth and Ocean Sciences

School of Natural Sciences

National University of Ireland, Galway

November 2016

Table of Contents

Table of Contents **1**
Declaration **4**
Examination Committee **5**
Acknowledgements **8**
Abstract **10**
List of Figures **11**
List of Tables **19**
1. Introduction **22**
1.1. Motivation and Literature Review 22
1.1.1. Why Model Sediment Mobility? 22
1.1.2. Maerl/Rhodolith Beds 23
1.1.3. Why Study Hydrodynamic Properties? 26
1.1.4. Abiotic Surrogacy 28
1.1.5. Patch Theory and Disturbance Regimes 28
1.1.6. Ecologically or Biologically Significant Areas (CBD, 2016) 29
1.1.7. Rhodoliths as Carbonate Producers 30
1.2. Study Site 31
1.3. Research Questions 35
1.3.1. Hydrodynamic Properties of Maerl 35
1.3.2. Coupled Modelling 35
1.3.3. Wider implications of Research 36
1.4. Structure of Thesis and Summary of Papers 38
1.4.1. Paper 1 Summary 38
1.4.2. Paper 2 Summary 39
1.4.3. Paper 3 Summary 40
2. Settling Velocity and Grain Shape of Maerl Biogenic Gravel **41**
2.1. Abstract 42
2.2. Introduction 43
2.2.1. Maerl 45
2.2.2. Previous Studies 46

2.2.3. Study Site 47
2.3. Materials and Methods 49
2.3.1. Settling-Velocity Methodology 49
2.3.2. Grain-Shape Methodology 51
2.3.3. Sediment Density 53
2.4. Results and Analysis 55
2.5. Discussion 63
3. Critical Bed Shear Stress of Maerl 66
3.1. Abstract 67
3.2. Introduction 68
3.2.1. Maerl 68
3.2.2. General Theory 70
3.3. Materials and Methods 71
3.3.1. Introduction to Experiment 71
3.3.2. Law of the Wall 72
3.3.3. Turbulent Kinetic Energy 73
3.3.4. Reynolds Stress 74
3.3.5. Critical Shields Parameter 75
3.3.6. Experiment 76
3.3.7. Data Processing 84
3.4. Results and Analysis 85
3.4.1. Velocity Profiles 85
3.4.2. Turbulence Characteristics 87
3.4.3. Critical Bed Shear Stress and Shields Parameters 91
3.5. Discussion 94
3.5.1. Experimental results 94
3.5.2. Implications for mobility 95
4. Mobility of maerl-siliciclastic mixtures: Impact of waves, currents and storm events 99
4.1. Abstract 100
4.2. Introduction 101
4.2.1. Study Site 106
4.3. Materials and Methods 111
4.3.1. Mesh and domain optimisation 111
4.3.2. Hydrodynamic Model 112

4.3.3. Spectral Wave Model 113
4.3.4. Sediment Transport Model 114
4.3.5. Sediment Mobility Computation 115
4.4. Results and Analysis 118
4.5. Discussion 130
5. Conclusions 136
6. Appendices 141
6.1. Appendix 1- Paper 2 141
6.1.1. Pangaea Database 141
6.1.2. Summary of Error Analysis 141
6.1.3. TKE and Reynolds Stress Errors 142
6.1.4. Sensitivity to Elevation 143
6.1.5. Extrapolation and Analysis of the Principal Reynolds Stress 145
6.1.6. Law of the Wall (LotW) with Replicates 149
6.1.7. Law of the Wall Error using Wilkinson (1983) 152
6.1.8. Grain Size Distribution 153
6.2. Appendix 2- Paper 3 156
6.2.1. Tidal Information- Galway Bay 156
6.2.2. Computational Mesh 157
6.3.3. Box Plots 158
6.3.4. Sensitivity Analysis 161
7. References 166

Declaration

EOG 020

OLLSCOIL NA hÉIREANN, GAILLIMH

NATIONAL UNIVERSITY OF IRELAND, GALWAY

THE PhD / MD DEGREE

APPROVAL FOR EXAMINATION

To: The Registrar & Deputy President, the National University of Ireland, Galway

Please tick (√) as appropriate: **PhD** _√_ **MD** ____

Thesis Titled:

Sediment Mobility Modelling and Hydrodynamic Properties of Maerl

Submitted by Candidate (please write in caps or type)

SIDDHI JOSHI

I, the **Candidate**, certify that the Thesis is all my own work and that I have not obtained a degree in this University or elsewhere on the basis of any of this work. (If the thesis is based on a group project, then the student must indicate the extent of his/her contribution, with reference to any other theses submitted or published by each collaborator in the project, and a declaration to this effect must be included in the thesis. This declaration should follow the Table of Contents).

Signed: ---------- Date: 4TH August 2016----------

I, the Candidate's **Primary Supervisor**, hereby confirm that I have inspected, and approve for examination, the final draft of the PhD thesis, of title above:

Signed: ---------- Date: 4TH August 2016----------

1. I, a member of the candidate's Graduate Research Committee, hereby approve for examination the final draft of the PhD/MD thesis of title above

2. For candidates in structured research programmes, I also confirm that the minimum requirements for the taught modules under the Structured PhD/MD, as required by College, have been successfully completed by the candidate.

Signed: ---------- Date: 4TH August 2016----------

N.B. This form should be forwarded to the Examinations Office, by the candidate, together with two gum or spiral-bound copies of the thesis.

Fees Office use only:

Student can submit, no fee issues: Yes: [ ], No: [ ]

Student owes €___ submission fee to NUI Dublin: Yes [ ], No: [ ]
http://www.nuigalway.ie/fees/

Examination Committee

Supervisor: Prof. Colin Brown, Director, Ryan Institute, NUI Galway

Chair: Prof. Mark Johnson, Marine Ecology, Ryan Institute, NUI Galway

External Examiner: Dr. Peter Harris, Director, GRID Arundel, Norway

Internal Examiner: Dr. Stephen Nash, Marine Modelling, Civil Engineering, NUI Galway

For Harsha Joshi, Kashyap Joshi and Surekha Jani

“The Coral Strand too is silvery, glimmery, moon-pale, and it crunches underfoot pleasantly; pick up a handful of its beach and you see it is composed of tiny twiglike bits of something like unglazed pottery, white, cream-coloured, pale green or faintly violet-flushed. This is not strictly coral, but fragments broken off a coraline alga.. ”

Tim Robinson—

Connemara- the Last Pool of Darkness

Acknowledgements

This research was funded by the Griffiths Geoscience Project (PI Prof. Colin Brown, NUI Galway). The funding for the award was established in Ireland as part of the National Geoscience Programme 2007–2013 and the Geological Survey of Ireland administers the award. Thanks go to DHI for the student labkit license for DHI MIKE 21/3™ and their kind assistance. We acknowledge the use of data from the INFOMAR Project, a joint seabed mapping project between the Geological Survey of Ireland and the Marine Institute.

Thanks to Dermot McDermott, Edward Kilcullen, and Mary O'Brien, Senior Technicians in College of Engineering and Informatics (NUI Galway) for their assistance and advice on the technicalities of the experiments. Acknowledgments to Dave McCarthy of University College Cork for providing his script in Mathematica for grain-shape analysis, Zoe Elliott in NUI Galway Geography for her participation in the settling-velocity experiment, Jazmin Hernandez-Kantun in NUI Galway Plant Science for information on rhodolith, and Fabio Sacchetti of University of Ulster and the crew of *Celtic Voyager* cruise CV11029 for the maerl sample from Aran. We thank reviewers Mike Church, Brandon McIlroy, JSR Associate Editor Paul Myrow, and Co-Editor Eugene Rankey, whose input resulted in much improvement to the final first paper.

For the second paper, additional funding was provided by the Thomas Crawford Hayes Trust Research Award, NUI Galway. We thank Prof. Wim Uijttewaal for use of the facilities in the Laboratory for Fluid Mechanics, Delft University of Technology (TU Delft); Sander de Vree, Jaap van Duin, Arie den Toom and Hans Tas of TU Delft; Prof. Leo van Rijn for valuable suggestions regarding experimental methodology; Fabio Sacchetti, Marine Institute for maerl sample collection.

For the final paper we thank the Marine Institute for oceanographic data, the National Parks and Wildlife Service, and the Department of Arts, Heritage and the Gaeltacht for providing data on the spatial distribution of maerl in Galway Bay, and the Office of Public Works for providing data on river

inputs to Galway Bay. We acknowledge the assistance of Martin White, Vera Van Lancker, John Coyne, Shane Rooney, Jazmin Hernandez-Kantun, Joe Breen, Mike Guiry, Prof. Christine Maggs, Prof. Jason Hall- Spencer, Scottish Natural Heritage, Kieran Lyons, Brian Sheridan and a special thanks to Sarah Knight.

Special thanks go to Colin Brown and Garret Duffy, the supervisors for their guidance and hard work in making this thesis possible and for the moral support during write up stages. Special thanks go to the external examiner Peter Harris and internal examiner Stephen Nash for constructive comments to improve the final thesis. Last but not least I would like to thank all the wonderful postgraduate (and undergraduate) students and staff in Earth and Ocean Science, NUI Galway whom I have had an opportunity to share an office over the years. It has been a joy to come to Galway to do my PhD, based in the quadrangle building and to visit and discover some of the most beautiful places of the west of Ireland.

Abstract

Sediment mobility modelling is a useful tool for scientifically robust marine spatial planning and characterisation of the benthic disturbance regime. As a prerequisite to modelling sediment transport of free living coralline algae habitats known as maerl or rhodolith, it is necessary to know fundamental hydrodynamic properties of this biogenic sediment. Two hydrodynamic properties, settling velocity and critical bed shear stress of maerl from three contrasting hydrodynamic regimes, have been determined. In Chapter 2, the settling velocity of maerl has been experimentally measured and rigorously compared with theoretical models of settling velocity and detailed grain shape parameters. Quantitative modifications of the Ferguson and Church (2004) equation for settling velocity have been made by allowing the drag coefficient C_2 parameter, which equates to the reciprocal of the convexity of the maerl grain, to vary with grain size. In Chapter 3, the critical bed shear stress of maerl is experimentally determined using three techniques; Law of the Wall, Turbulent Kinetic Energy and Reynolds Stress. The results show that maerl has a lower critical Shields parameter than quartz grains of an equivalent sieve diameter primarily due to their highly-irregular grain shape leading to greater drag experienced by the maerl grains and the relative grain protrusion. In Chapter 4, coupled hydrodynamic-wave-sediment transport models are computed using the DHI MIKE 21 suite of modelling tools and subsequently utilised to compute the spatially-varying tidally-induced sediment mobility and combined wave-current induced sediment mobility during calm and storm conditions. A grid of spatially-varying critical Shields parameter is computed for maerl areas and areas of Galway Bay with quartz siliciclastic sediments. Maerl is present at the periphery of wave-induced residual current gyres during storm conditions. The peak combined wave-current induced Mobilization Frequency Index during storm conditions is the key hydrodynamic parameter governing the distribution of maerl and siliciclastic sediments and is the most useful physical surrogate for maerl in predictive habitat suitability modelling studies. The thesis concludes by evaluating the utility of sediment mobility indices for marine spatial planning and for the design of Marine Protected Areas (MPAs).

List of Figures

A disc with the electronic copy of the thesis, including thesis figures, and high resolution copies of all individual maps, can be found in the sleeve in the back cover.

Chapter 1

Figure 1.1 and 1.2: Typical branched maerl from the North Atlantic beds.

Figure 1.3 and 1.4: *Lithothamnion glaciale* maerl bed in the Caol Scotnish rapids with common brittlestars *Ophiothrix fragilis* and the smaller black brittlestar *Ophiocomina nigra* (1.3) and Seven armed starfish *Luidia ciliaris* on maerl bed. Images copyright of Scottish Natural Heritage.

Figure 1.5, 1.6, 1.7 and 1.8: Different growth forms of maerl result from difference in the hydraulic energy present and in turn show a different hydrodynamic behaviour, affecting sediment transport.

Figure 1.9: Forces acting on a maerl grain during initiation of motion.

Figure 1.10: Eco-geographical variables of abiotic surrogates may be utilised as part of habitat suitability models of maerl and related species.

Figure 1.11: : Multibeam Bathymetry and LiDAR data from Galway Bay, one of the twenty six INFOMAR priority bays in Ireland (INFOMAR, 2016).

Figure 1.12: Distribution of the median diameter, *d50* of 110 grab samples of seafloor sediment obtained between March 2009 and August 2010, and maerl areas with the offshore SACs.

Chapter 2

Figure 2.1: Maerl sample locations in Galway Bay, west coast of Ireland, with three different hydrodynamic regimes that include beach sediment, an intertidal bed, and an open marine bed. The images of the maerl represent a

footprint of 0.25 m by 0.10 m on the seafloor. F, Foul Sound; G, Gregory Sound.

Figure 2.2: A) Experimental setup for measuring maerl settling velocity, with B) a settling tube monitored at two points either side of a 1 m section by two video cameras.

Figure 2.3: A) A microscope image of a 2.5 cm diameter stub with maerl grains from the intertidal bed. This is an example of highly irregular maerl with a low convexity value. B) A binarized image with grain perimeter, bounding box, and convex hull perimeter.

Figure 2.4: Settling velocity versus sieve diameter with two Ferguson and Church (2004) model curves using constant C_1 and C_2. The $C_1 = 18$, $C_2 = 0.4$ curve is for smooth spheres; the $C_1 = 24$, $C_2 = 1.8$ is for highly angular quartz grains.

Figure 2.5: Grain-shape parameters (convexity, circularity, and caliper elongation) for the three samples versus sieve diameter. The reciprocal of convexity increases linearly with diameter. The solid line represents the least-squares fit between the reciprocal convexity and diameter, plotted as the convexity versus diameter. The coefficient of determination is $r^2 > 0.9$ for each sample.

Figure 2.6: Settling velocity versus diameter using the modified version of the Ferguson and Church (2004) model, where C_2 is allowed to vary linearly with diameter. The coefficients of determination, r^2 for the model curves and observed data vary between 0.95 and 0.97 for experiments with salinity of 35 ppt; they are lower for the freshwater experiments due to data outliers.

Figure 2.7: The parameter C_2 and the drag coefficient as a function of sieve diameter. The drag coefficient and C_2 inferred from the settling-velocity inversions are compared with theoretical values from the Ferguson and Church (2004) model modified to account for the linear variation of C_2 with diameter.

Figure 2.8: Drag coefficient versus grain Reynolds number for the three maerl samples at salinity 35, superimposed on drag-coefficient curves based on data from (Komar and Reimers, 1978) for settling-velocity experiments across a range of grain shapes. The latter represent parametric trends with different Corey shape factors between 0.22 and 1.0 where a value of 0.7 is typical for natural quartz grains.

Figure 2.9: C_2 ($= aC^{-1}$) estimated from the grain-shape measurements of convexity versus C_2 inferred from the settling-velocity observations using this paper's modification of the Ferguson and Church (2004) model with $C_2 = C_{21}\, d$. The solid lines in the figure have a gradient of 1 to highlight the correlation between the estimated and inferred C_2. The actual gradients of the least-squares lines fitted between the two variables are 0.85 ± 0.15 ($r^2 = 0.7$), 0.91 ± 0.1 ($r^2 = 0.85$), and 0.98 ± 0.02 ($r^2 = 0.97$) for Carraroe, Aran, and Muckinish grains, respectively.

Chapter 3

Figure 3.1: A) The TU Delft rotating annular flume. B) A plan view of the rotating annular flume, with the side-looking Acoustic Doppler Velocimeter (ADV), Electromagnetic Liquid Meter and HD video camera. The ADV is mounted at 7 cm above the bed.

Figure 3.2: A) Cross-section of velocity field in the rotating annular flume with the same ratio between the lid and flume rotation speeds used in this experiment (Booij 1994) B) The coordinate system (Booij 1994) showing tangential (u), radial (v) and vertical (w) components to which all measured velocities were transformed. Lid (ω_l) and flume base (ω_b) rotation speeds are also shown. C) Measured velocity profile at 45 cm s^{-1} for run 3 of the Carraroe samples. D) TKE shear stress profile at 45 cm s^{-1} for the Carraroe sample. E) The two-cell secondary flow model of Sheng (1989) for the generalised rotating annular flume. The figure illustrates the effect of the secondary circulation, particularly at elevations ~ 5cm, on profiles which were located near the bottom right of Figure 3.2A.

Figure 3.3: Velocity profiles for samples from Carraroe (beach), Muckinish (intertidal) and Aran (open marine). The rows correspond, from the top, to runs 1, 2 and 3 and the bottom row corresponds to the run at critical threshold velocity. The Aran curves show some interference effects in the flow field at elevations > 10 cm due to the top boundary of the linear flume.

Figure 3.4: The velocity profile in the logarithmic layer as a function of elevation, z (m) in semi-log space for LOTW estimation at initiation of motion.

Figure 3.5: The profiles of the bed shear stress derived using the TKE method for the 4 velocity runs. For Carraroe, secondary flow interference is apparent at elevations ~ 4 – 6 cm; for Aran, at elevation > 8 cm due to the top boundary of the linear flume; for Muckinish curve (run 3), an eddy effect is apparent at ~ 7 cm. The Muckinish curve at the critical threshold velocity has the steepest increase in shear stress near the bed because of the high grain roughness.

Figure 3.6: The profiles of TI for the 4 velocity runs. The Aran curves show some interference effects at elevations > 10 cm.

Figure 3.7: The profiles of the three-dimensional RS as a function of elevation above bed level at the critical threshold velocity. An outlier associated with the secondary flow cell at elevation 4.5 cm for the Carraroe run is omitted.

Figure 3.8: Shields curve with envelope and the critical Shields parameters for the three maerl samples. The non-dimensional grain diameter D* is a function of the median particle size, fluid viscosity and specific gravities of particle and fluid (Soulsby, 1997).

Chapter 4

Figure 4.1: Galway Bay study site. Distribution of the median diameter, d50 of 110 grab samples of seafloor sediment obtained between March 2009 and August 2010, and maerl beds (A), smoothed distribution of the critical Shields parameter (B), location on the west of Ireland (C), and nested, computational mesh superimposed upon bathymetry (D). MH is the location (53° 19.5 N, 9° 54.25' W) of Mace Head Atmospheric Station. The three islands are known as the Aran Islands; Inishmore, Inishmaan and Inisheer (from east to west).

Figure 4.2: Hydrodynamic and wave outputs from summer 2007. Significant wave height (A), wave period (B), horizontal particle velocity at bed (C), depth-averaged current speed (including wave-induced currents) during the spring tide flood (D) and spring tide ebb (E), and wind velocity rose at Mace Head over the spring neap cycle (F).

Figure 4.3: Hydrodynamic and wave outputs from winter 2013. Significant wave height (A), wave period (B), horizontal particle velocity at bed (C), depth-averaged mean current speed (including wave-induced currents) during the spring tide flood (D) and spring tide ebb (E), and wind velocity rose at Mace Head over the spring neap cycle (E).

Figure 4.4: Validation of hydrodynamic and wave models with data (red) and theoretical response (black) for significant wave height (A), wave period (B), surface elevation (C) for 24th July to 7th August, 2007; significant wave height (D), wave period (E) for 15th to 28th December 2013; depth-averaged current speed (F) for 1st to 15th September, 1994. The surface elevation was calibrated by reference to the Inishmore tide gauge (-9.6669W, 53.1178 N) which was corrected to the same vertical datum (Mean Sea Level- OSGM05) by applying a +14.6 cm shift (INFOMAR, 2007).

Figure 4.5: Modelled peak depth averaged shear velocity in Galway Bay. Summer 2007 due to currents (A) and combined wave-currents (B), and winter 2013 due to currents (C) and combined wave-currents (D).

Figure 4.6: Residual currents in the modelling period of summer 2007 (A) and winter 2013 (B) and box plot to show residual currents in maerl and non-maerl areas during summer 2007(C), with further box plots in Appendix- Section 6.2.

Figure 4.7: Mobilization Frequency Index (MFI) due to currents (A) and combined wave-currents (B) over the spring-neap cycle in summer 2007, and due to currents (C) and combined wave-currents (D) over the spring-neap cycle in winter 2013. Grain size distribution with maerl areas (E) and spatially varying critical Shields parameter (F) have been reproduced to enable comparison.

Figure 4.8: Sediment Mobility Index (SMI) for the summer 2007 (A) and multibeam acoustic backscatter (B) with dark areas representing high backscatter and light areas representing low backscatter, and SMI for winter 2013 storms (C). Note the different colour palettes for summer and winter SMI maps to emphasise different SMI levels and facilitate comparisons with the backscatter map.

Figure 4.9: Sediment transport model. Erosion (bed level change below 0) and deposition (bed level change above 0) at the seafloor (A) and rate of seafloor level change (B) for summer 2007, and equivalent results for winter 2013 (C) and (D).

Figure 4.10: Sediment transport vectors map (total load components) with bed level over one spring-neap tidal cycle in summer 2007 (A) and winter 2013 (B).

Appendix

Figure 6.1: Extrapolation and Analysis of the Principal Reynolds Stress for Muckinish intertidal sample.

Figure 6.2: Carraroe Threshold Quadrant Analysis.

Figure 6.3: Carraroe Threshold Quadrant Analysis.

Figure 6.4: Carraroe Threshold Quadrant Analysis.

Figure 6.5: Carraroe Law of the wall with replicates.

Figure 6.6: Aran Law of the wall with replicates.

Figure 6.7: Muckinish Law of the wall with replicates.

Figure 6.8: Carraroe grain size statistics.

Figure 6.9: Aran grain size statistics.

Figure 6.10: Muckinish grain size statistics.

Figure 6.11: Galway Bay Computational Mesh Extent, with locations of ADCP, tide gauge and wave buoys.

Figure 6.12: Box plot for Mobilisation Frequency Index in maerl and non-maerl areas in Summer 2007.

Figure 6.13: Box plot for Mobilisation Frequency Index in maerl and non-maerl areas in Winter 2013.

Figure 6.14: Box plot for Sediment Mobility Index in maerl and non-maerl areas in Summer 2007.

Figure 6.15: Box plot for Sediment Mobility Index in maerl and non-maerl areas in Winter 2013.

Figure 6.16: Box plot for residual currents in maerl and non-maerl areas in Winter 2013.

Figure 6.17: Sensitivity results of MFI in 2007 showing the upper bound (MFI + 20% current speed, significant wave height and wave period) for pure currents (A), combined wave currents (B) and the corresponding difference in MFI in comparison to the final results (C and D). Note the difference in combined wave-current situation is greatest in D just south of Inisheer, where there is the highest uncertainty in the final MFI, likely due to the largest significant wave heights.

Figure 6.18: Sensitivity results of MFI in 2007 showing the lower bound (MFI - 20% current speed, significant wave height and wave period) for pure currents (A), combined wave currents (B) and the corresponding difference in MFI in comparison to the final results (C and D). Note the difference in combined wave-current situation is greatest in D just west of the Aran Island, where there is the highest uncertainty in the final MFI.

Figure 6.19: Sensitivity results of SMI in 2007 showing the upper and lower bounds (SMI ± 20% current speed, significant wave height and wave period) for combined wave-currents upper bound (A), combined wave-currents lower bound (B) and the corresponding difference in SMI in comparison to the final results (C and D).

Figure 6.20: Sensitivity results for choice of time interval (10 equal interval time steps in a spring neap cycle) in the sediment mobility calculation. Mobilization Frequency Index (MFI) due to currents (A) and combined wave-currents (B) over the spring-neap cycle in summer 2007, and Sediment Mobility Index (C), with corresponding differences with the final results which used 20 timesteps (D, E and F).

Figure 6.21: Sediment transport model results for quartz with critical shields parameter of 0.06 density 2650 kg m^{-3}. Bed level change shows zones of deposition or erosion in summer 2007 (A) and winter 2013 (C) and Rate of Bed level change in summer 2007 (B) and winter 2013 (D). Results show larger zone of deposition in centre of the bay and smaller zone of erosion and a lower sediment transport rates than maerl results due to a higher critical bed shear stress and density of quartz than that of maerl as expected.

List of Tables

Chapter 1

Table 1.1: Key statistics about oceanography in Galway Bay (Data from Admiralty (2015) and Marine Institute Ireland (MI, 2016).

Chapter 3

Table 3.1: Flow Reynolds Number (Re), depth-averaged velocity u (cm s^{-1}), and flume base and lid rotation speeds (s^{-1}) for each run. The Re is calculated from uR/v where R is the hydraulic radius, v is the kinematic viscosity (1.004 x 10^{-6} m^2 s^{-1}) for a water temperature of 21ºC. The hydraulic radius was 28 cm for the rotating annular flume and 25 cm for the linear flume.

Table 3.2: The stages of motion for each of the four velocity runs.

Table 3.3: Parameters derived from the flume experiments, including the precision at one standard deviation.

Chapter 4

Table 4.1: Key statistics about oceanography in Galway Bay (Data from Admiralty (2015) and Marine Institute Ireland (MI, 2016).

Table 4.2: Details of the computational mesh used in the coupled hydrodynamic-wave-sediment transport models, with mesh extent map in Appendix (Section 6.2).

Table 4.3: The RMSEs and R^2 values of validation of the coupled models.

Table 4.4: Summary of the key correlation coefficients (R^2) between sediment mobility indices and backscatter strength.

Appendix

Table 6.1: TKE and RS triplicates, and Shields parameters with errors, for Carraroe.

Table 6.2: TKE and RS triplicates, and Shields parameters with errors, for Aran.

Table 6.3: TKE and RS triplicates, and Shields parameters with errors, for Muckinish.

Table 6.4: Sensitivity analysis due to choice of bed elevation for Carraroe TKE.

Table 6.5: Sensitivity analysis due to choice of bed elevation for Aran TKE.

Table 6.6: Sensitivity analysis due to choice of bed elevation for Muckinish TKE.

Table 6.7: Sensitivity analysis due to choice of bed elevation for Carraroe RS. Aran RS values are negative so the Shields parameter was not obtained using this technique.

Table 6.8: Sensitivity analysis due to choice of bed elevation for Muckinish RS.

Table 6.9: The quadrants for the points at 0.1 of the flow depth at threshold conditions are a useful way of identifying the dominant turbulent process at the point.

Table 6.10: Precision errors using the law of the wall methodology at Carraroe.

Table 6.11: Precision errors using the law of the wall methodology at Aran.

Table 6.12: Precision errors using the law of the wall methodology at Muckinish.

Table 6.13: Date, time and levels of Highest Astronomical Tide in this century in Galway Bay.

Table 6.14: The mean and standard deviation of the differences of sediment mobility indices in summer 2007 and upper bound as a result of the sensitivity analysis introducing 20% errors in hydrodynamic parameters.

Table 6.15: The mean and standard deviation of the differences of sediment mobility indices in Summer 2007 and lower bound as a result of the sensitivity analysis introducing 20% errors in hydrodynamic parameters.

Table 6.16: The mean and standard deviation of the differences as a result of the sensitivity analysis of time interval on sediment mobility indices in summer 2007.

1. Introduction

1.1. Motivation and Literature Review

1.1.1. Why Model Sediment Mobility?

Sediment mobility modelling is of importance to a range of disciplines including sediment dynamics, marine conservation, coastal engineering and renewable energy (Harris and Coleman, 1998; Idier et al., 2010; Li et al., 2015). It is based on the fundamental quantity of bed shear stress and the impact of pure currents, wave-only, wave-induced currents or combined wave-current flow on surficial sediments (Hemer, 2006; Dalyander et al., 2013). Utilising coupled hydrodynamic-wave-sediment transport models, it is possible to extract useful information about the sediment transport in regional and coastal seas, and estuarine environments (Warner et al., 2008; Brown and Wolf, 2009; Bever and MacWilliams, 2013; Hoeke et al., 2013). However, given the high level of uncertainty of the theory and data underpinning sediment transport modelling, the reliability of sediment transport models still lags behind that of hydrodynamic and wave models (Wilcock, 2001; Schmelter et al., 2012). Sediment mobility modelling is one alternative methodology to the sediment transport model, generating useful sediment transport information from knowledge of the hydrography (Idier et al., 2010).

Benthic habitats are affected by abiotic factors and the oceanography of the benthic boundary layer is of significance to habitat forming biogenic reef systems such as maerl or rhodolith beds. Sediment mobility modelling is a useful way of quantifying the interaction between the hydrodynamics, sediment dynamics and ecology of mobile biogenic maerl forming habitats. With the changing climate and increased storminess, modelling tools provide a unique opportunity to model impacts of episodic natural disturbance events such as extreme storms on maerl as biogenic sediment. A key study by Brodie et al. (2014) on the impact of a high CO_2 world on benthic flora suggests increased storminess is one of the factors which leads to a biogeographical shift in the range of maerl beds.

1.1.2. Maerl/Rhodolith Beds

Maerl or rhodolith beds are non-geniculate, free-living coralline algae habitats, with two maerl forming species: *Lithothamnium corallioides and Phymatholithon calcareum* found in the EC Habitats Directive. Maerl beds are one of the four main macrophyte dominated benthic communities in the world (Foster, 2001). Rhodoliths have different morphologies and growth forms including prâlines, boxwork and unattached branched rhodolith morphologies, depending on the hydrodynamic energy present during formation (Basso, 1998). Some authors distinguish between the term maerl and rhodolith, with maerl being the unattached branched structures and rhodoliths being nodules. Further sub-divisions into encrusting, lumpy or fruticose rhodoliths (especially of prâline rhodoliths) have also been made (Woelkerling et al., 1993; Sañé et al., In Press). This study uses "rhodolith" to refer to aggregates of non-geniculate coralline macroalgae and is inclusive of the term "maerl", the English translation of the Breton term "maërl" (Figures 1.1 and 1.2). It is important to note that the term rhodolith includes maerl, but the term maerl does not include rhodolith. "The term rhodolith is more sedimentological and genetic (a nodule made of red calcareous algae)…whereas the term maerl is only referring to the branched growth forms, that can have very variable final shape" (Daniela Basso, *pers. comm*.). The origins of this stem from the fact that branched maerl of Lemoine (1910) was used as reference material for nodular rhodoliths of the Mediterranean (Basso et al. (2015). It is important to stress correct terminology as international legislation is based on and restricted to these terms. For example in the UK and Ireland, all nodular forms (technically rhodoliths) are known as maerl in UK and Irish waters in legislation.

Figures 1.1 and 1.2: Typical branched maerl from the North Atlantic beds.

Maerl forms dense biogenic reefs with high micro-scale complexity, supporting a diverse range of rare epifauna and epiflora, some of which are endemic to maerl (Figures 1.3 and 1.4). Rhodoliths have the requirement for photosynthesis and are generally restricted to the depth of the euphotic zone which can be as deep as 268 m in the Caribbean (Littler et al., 1985). Newly discovered rhodolith beds off the East coast of Brazil on the Abrolhos Shelf have an extent of 21 000 km^2 - an area the size of El Salvador (Amado-Filho et al., 2012). Most recently rhodolith beds have been discovered in the mouth of the Amazon (Moura et al., 2016). Maerl beds are slow growing stores of carbon and are globally important blue carbon sinks when they are buried. De Grave et al. (2000) estimate the national maerl-bearing sediment resource volume in Ireland in the order of 114 x 10^6 m^3, which equates to an estimated total of 11 856 456 tons of blue carbon stored in maerl habitats in Ireland, based on carbon storage figures used in a report by the Scottish government (Burrows et al., 2014) (i.e. 114 × 10^6 m^3 × 0.8667 tons m^{-3} × 0.12 = 11 856 456 tons of C). This is the best available estimate of the storage of blue carbon in Irish maerl beds.


Figures 1.3 and 1.4: *Lithothamnion glaciale* maerl bed in the Caol Scotnish rapids with common brittlestars *Ophiothrix fragilis* and the smaller black brittlestar *Ophiocomina nigra* (1.3) and seven armed starfish *Luidia ciliaris* on maerl bed (1.4). Images copyright of Scottish Natural Heritage.

Historically, maerl was mistaken to be coral on Admiralty charts, with an estimated 50-60 % of "crl" areas as being maerl areas in Irish waters (De Grave and Whitaker, 1999). Commercial extraction of maerl has been carried out historically for use as a soil conditioner, as a lime replacement, for the treatment of acidic drinking water, as an animal food additive and as

a health food supplement (Birkett et al., 1998). Maerl is a non-renewable resource which has been traditionally been extracted on a small scale. However, more recently large scale extraction has occurred particularly in Brittany, where an estimated 600,000 tonnes per annum of maerl were commercially extracted during the 1970s (Cabioch, 1969; Birkett et al., 1998; De Grave et al., 2000). Commercial extraction of maerl is banned in Brittany since 2011. In the UK, the low recoverability of maerl due to slow growth rates was recognised in 2005, when extraction of maerl was banned (Hall-Spencer, 2005). In Ireland, a company, Celtic Sea Minerals Ltd., was licenced to extract 5,000 tonnes per annum off Lonehort Point, Bantry Bay in 1994 (Birkett et al., 1998). Following this, a licence to extract up to 16,000 tonnes per annum from 2001 – 2010 was granted. However, this license has not been used since 2007 and maerl has been sourced from Iceland (Celtic Sea Minerals Ltd, 2016; MI, 2016). Commercial extraction has been identified to be the single biggest anthropogenic threat as it removes the productive surface layer at the top of maerl beds (Hall-Spencer, 1994; *pers. comm.*). This results in excessive sediment load leading to smothering by fine sediment also impacting the surrounding community (Birkett et al., 1998; Wilson et al., 2004). Maerl beds in Galway Bay and its surrounding have never been commercially extracted in the last 100 years and have been protected as an Special Areas of Conservation (SAC) (NPWS, 2013). In Ireland, it is illegal to remove small quantities of material from the beach under the Foreshore Act (1933) (Michael Guiry, *pers. comm*.).

Salmon farming over and adjacent to maerl beds has a detrimental impact even in strongly tidal areas (Hall-Spencer et al., 2006). Contamination occurs from an influx of fish faecal pellets and partially consumed food waste which deposit upon the maerl bed. This material decomposes and increases oxygen demand inducing anaerobic conditions (Birkett et al., 1998; Sanz-Lázaro et al., 2011). Bivalve dredging as well as eutrophication have been identified to be major threats to maerl (Hall-Spencer, 1995; Grall and Glemarec, 1997; Hall-Spencer et al., 2003). Other anthropogenic threats to maerl have been detailed in publications relating to the BIOMAERL Project (BIOMAERL, 1999; Barberá et al., 2003).

1.1.3. Why Study Hydrodynamic Properties?

The hydrodynamic properties of maerl have received very little attention from the research community and are a necessary prerequisite to sediment transport studies on maerl (Weill et al., 2010; Joshi et al., 2014) . The settling velocity and critical bed shear stress are fundamental quantities in sediment dynamics, required for the quantification of sediment transport (Van Rijn, 1993). The critical bed shear stress influences the likelihood for suspension whereas the settling velocity influences the likelihood for deposition. Although initiation of motion due to unidirectional currents is a classic problem in sediment dynamics, this has rarely been studied in the case of maerl (Harris et al., 1996; Mitchell, 2001). Related physical quantities such as the grain size, grain shape and specific gravity or sediment density are also key quantities which need to be known in order to quantify the fundamental sediment properties of maerl as biogenic sediment. Furthermore, both physical and hydrodynamic properties of maerl vary with the amount of hydraulic energy present in a particular environment, in turn affecting maerl hydrodynamic behaviour (Figures 1.5-1.8).

Figure 1.5, 1.6, 1.7 and 1.8: Different growth forms of maerl result from difference in the hydraulic energy present and in turn show a different hydrodynamic behaviour, affecting sediment transport.

For example, the forces acting on a prominent grain during initiation of motion are the lift and frictional drag component of the fluid force and the submerged weight (Figure 1.9). In the case of maerl, these are altered due to the irregular grain shape of maerl altering the packing of the maerl sediment, as well as complex hiding and exposure effects of the maerl grain and the presence of additional intergranular forces affecting maerl mobility.

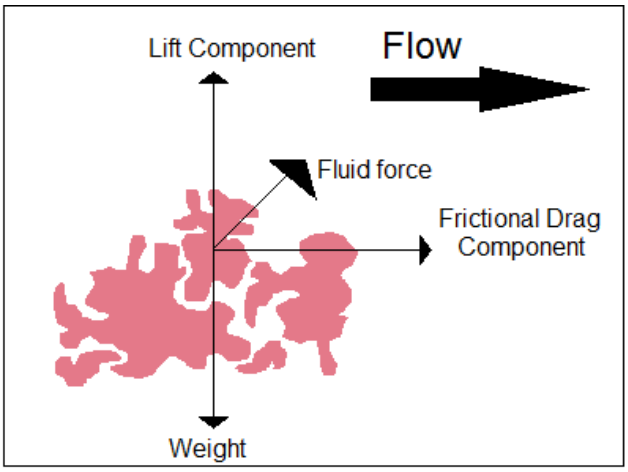

Figure 1.9: Forces acting on a maerl grain during initiation of motion.

In this thesis, Chapters 2 and 3 are focussed on the setting velocity of maerl and critical bed shear stress respectively. Further details are given in Section 1.3.

1.1.4. Abiotic Surrogacy

In terms of marine conservation, the sediment mobility of maerl is an important biophysical variable, which could be used as a predictor for species occurrence. Harris (2012c) defines "surrogacy" in the context of benthic habitat mapping studies as a biophysical variable that can be quantitatively mapped to benthic species occurrence. An abiotic or physical surrogate may be a direct or indirect variable affecting the presence or absence of a particular species in a particular space at a particular time.

Chapter 4 of this thesis sets out to determine the variables that are the best abiotic surrogates for maerl, and the characteristics that can be used as predictors for maerl species occurrence. For example, it is well known that light intensity is a physical surrogate for maerl species occurrence as maerl is an alga which needs to photosynthesize. It can then be incorporated into a suite of eco-geographical variables for maerl to use as part of predictive habitat suitability models and related species living on maerl (Figure 1.10).

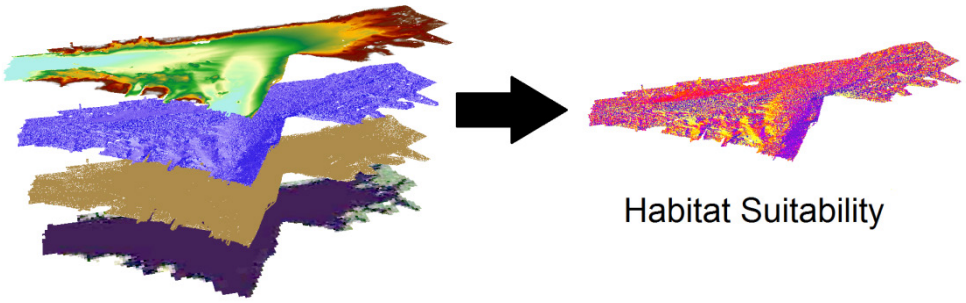

Figure 1.10: Eco-geographical variables of abiotic surrogates may be utilised as part of habitat suitability models of maerl and related species.

1.1.5. Patch Theory and Disturbance Regimes

A habitat patch can be defined as a discrete landscape element; all natural systems have patchiness at certain scales (Pullin, 2002). Therefore, a habitat may contain a range of hierarchal patches, exhibiting either physical or biological patchiness depending on their cause (Harris, 2012a). The thesis is limited to the physical causes of marine benthic patchiness due to fluctuating quantities over a range of spatio-temporal scales. It focuses on

recurring disturbance events such as storms which may cause marine benthic patchiness. Harris (2012a) discuss other causes of physical patchiness such as bathymetry, slope, roughness, wave-current exposure, water properties (temperature, salinity, dissolved oxygen content), geology, sediment properties, and combinations of these factors. All of these affect the habitat heterogeneity of the seafloor. Environmental disturbances may be biological or physical, chemical, periodic or episodic in nature and can dynamically affect the species habitat, resulting in stress on organisms, mobilising sediments, abrasion, limiting light availability, interruption in food supply, changes in availability of habitat or resources (Harris, 2012a). Patch clearing processes such as severe storms can result in an altered environmental disturbance regime, triggering ecological succession until the disturbed patch becomes equivalent to the undisturbed patch. In turn, this affects the recoverability of the benthic habitat. Maerl can be a very old species that is slow (~10-100 years) to recover fully from disturbance due to its slow rate of growth and reproduction. In Chapter 4, the work on sediment mobility as an indicator of benthic disturbance gives insights into the recoverability of the habitat as well as the disturbance regime.

1.1.6. Ecologically or Biologically Significant Areas (CBD, 2016)

The following are the scientific criteria for identifying marine ecologically or biologically significant areas (EBSAs) adopted by the Convention on Biological Diversity (COP 9) and including references for maerl:

- Uniqueness or Rarity (BIOMAERL, 1999)
- Special importance for life history stages of species (Kamenos et al., 2004b; Steller and Cáceres-Martínez, 2009)
- Importance for threatened, endangered or declining species and/or habitats (Hall-Spencer et al., 2008)
- Vulnerability, Fragility, Sensitivity, or Slow recovery (Grall and Hall-Spencer, 2003)
- Biological Productivity (Sciberras et al., 2009)
- Biological Diversity (Nelson et al., 2014)
- Naturalness (Barberá et al., 2003)

Maerl beds meet all seven criteria and have the potential to form part of representative networks of Marine Protected Areas (MPAs).

1.1.7. Rhodoliths as Carbonate Producers

Rhodoliths are major temperate carbonate producers and form an important component of the cool-water carbonate systems of the Heterozoan Association (James, 1997; Nalin et al., 2006; Titschack et al., 2008). Pleistocene coralline algal accumulations known as *"Coralligène de plateau"* cover an extensive area of the warm temperate Mediterranean and are considered to be carbonate factories (Nalin et al., 2006; Titschack et al., 2008; Coletti et al., 2015). Rhodolith facies forming an integral part of mixed carbonate-siliciclastic deposition systems at the Abrohlos Shelf in Brazil also contribute to carbonate production (Amado-Filho et al., 2012; D'agostini et al., 2015).

In the west of Ireland, a facies model of maerl sediments has been proposed by Bosence (1980) with rippled Clean Algal Gravel facies found in the most exposed areas. Furthermore, in intermediate energy areas a Muddy Algal Gravel dominates with progressively increasingly fine sediments accumulating in low energy areas (Bosence, 1980). This suggests that there is significant winnowing of mixed maerl-siliciclastic material leading to the formation of beds with a high percentage maerl. Bosence and Wilson (2003) estimated the carbonate production and accumulation rates for maerl beds in the North Atlantic, including Mannin Bay, Connemara, Co. Galway. They also conclude that rates are such that sustainable extraction is not possible and maerl is a non-renewable resource (Bosence and Wilson, 2003).

1.2. Study Site

Galway Bay is a large bay semi-enclosed at its western end by the three Aran Islands. Galway Bay is defined as 62 km long from west to east, the mouth of the bay is 33 km wide from north to south, and narrows to 10 km at Black Head (INFOMAR, 2016). The three islands are known as Inishmore, Inishmaan and Inisheer (from west to east). The seafloor sediment is underlain by granite in the north of the bay with a major submarine fault (Pracht et al., 2004) juxtaposing Carboniferous karst limestone of the Burren to the south, the most extensive limestone region in north-west Europe (McCabe, 2008). The presence of the Galway Bay fault in North Sound has recently been discovered and documented by the INFOMAR multibeam and LiDAR survey of Galway Bay from 2006-2014 (INFOMAR, 2016; Figure 1.11). Outcrops of limestone rock are present in the Outer Bay and in the Inner Bay, along with glacial features such as drumlins, sheet moraines and elongated, esker-type gravel ridges (Lei, 1995). The regional climate around Galway Bay is primarily governed by the influence of the North Atlantic Drift and prevailing south-westerly winds, whose combined effect in the Bay is mitigated by the Aran Island. The islands also provide shelter from the largest swell fields of the North Atlantic which significantly influence the regional oceanography.

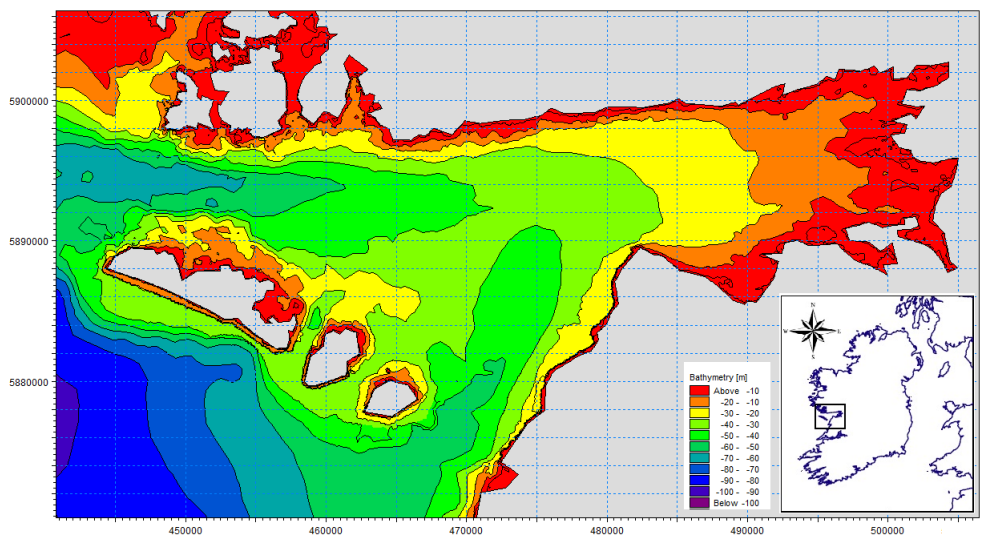

Figure 1.11: Multibeam Bathymetry and LiDAR data from Galway Bay, one of the twenty six INFOMAR priority bays in Ireland (INFOMAR, 2016).

Tides are dominated by the semi-diurnal tidal constituents and are macrotidal (Table 1.1). Outer bay wave data are 6 year seasonal means from a non-directional wave buoy and inner bay wave data are 10 year seasonal means from the Spiddal wave rider buoys (location map and further tidal information can be found in Section 6.2). Temperature and salinity ranges are based on a ROMS model with 6 year seasonal means (MI, 2016).

Table 1.1: Key statistics for oceanography in Galway Bay (Data from Admiralty (2015) and MI (2016).

	Spring	Summer	Autumn	Winter
Tidal Range (m)	4.50m (mean spring tides)		1.90m (mean neap tides)	
Significant Wave Height (m) (mean)	2.78 (outer)	1.95 (outer)	3.08 (outer)	3.89 (outer)
	0.64 (inner)	0.58 (inner)	0.81 (inner)	1.03 (inner)
Wave period (s) (mean)	7.27 (outer)	6.25 (outer)	7.38 (outer)	8.05 (outer)
	3.83 (inner)	3.62 (inner)	3.90 (inner)	4.36 (inner)
Wave Direction (º) (mean (direction))	219 (SW)	229 (SW)	223 (SW)	223 (SW)
Temperature (ºC) (mean ± sd.)	9.79 ± 1.49	15.7 ± 0.93	13.8 ± 1.60	9.01 ± 1.25
Temperature range (ºC) (min. – max.)	6.89 - 12.7	14.0 - 17.7	8.56 - 15.7	5.49 - 11.2
Salinity (mean ± sd.)	33.2 ± 2.43	34.0 ± 1.65	34.0 ± 2.25	33.0 ± 3.28
Salinity Range (min. – max.)	13.3 - 34.9	19.7 - 35.1	12.5 - 35.1	10.0 - 35.1

The net inflow from South Sound is greater than the net outflow from the North Sound, resulting in an anti-clockwise gyre in Galway Bay (Booth, 1975; Lei, 1995) and deposition of sediment in the centre of the Bay (Booth, 1975; O'Connor et al., 1993). The moderate exposure to wave action results in the deposition of fine sand and mud (Keegan, 1972). A higher percentage

of silt-clay is found along the northern shore as a result of freshwater input from the River Corrib at the northeast end of the bay (Figure 1.12).

Lei (1995) carried out the first three-dimensional hydrodynamic modelling in Galway Bay. Their model identified the influence of the River Corrib extending to the inner bay, and the north shore where some regions of stratification occur during the summer. There are also several minor tributaries to the west of the Corrib and Lei (1995) concludes that the freshwater input, together with the prevailing south-westerly wind, governs the oceanographic circulation. Additional freshwater and submarine ground water inputs from the southeast and southern shores (Smith and Cave, 2012) and upwelling of nutrient rich waters at Kilkerrin Bay (Roden and Raine, 1994; Sides et al., 1994) are present but not modelled.

Residual currents are the currents remaining after removal of all oscillatory tidal currents (Pugh and Woodworth, 2014). Lei (1995) reviewed the possible factors affecting residual currents in Galway Bay, including tide-induced, wind-induced and as a result of freshwater input. The study confirms that wind-induced currents are more important than tide-induced currents. Ren et al. (2015) compared the wind-induced circulation with a wave radar system near a wave energy test site at the north shore and suggested wind shear can propagate to the sub-surface.

Bathymetric constraints are significant in any hydrodynamic model for Galway Bay as they must account for the presence of, for example, accelerated currents known to be associated with the headland of Black Rock and channels created by inlets and islands on the north shore. Interaction of the tidal wave with coastal geometry must also be included in any hydrodynamic model as it gives rise to inequalities in the amplitude and duration of ebb and flood tidal flows resulting in tidal residual currents.

Outside of Galway Bay, seasonality and structure of hydrographic patterns off the western Irish Shelf are influenced by Eastern North Atlantic Water modified by freshwater input from River Shannon (Fernandes, 1988; Nolan, 2004).

Maerl Beds in Galway Bay

Galway Bay contains more than 65-70% of the maerl beds in Ireland (De Grave and Whitaker, 1999). The National Parks and Wildlife Service have extensively surveyed the maerl beds especially in and around the Special Areas of Conservation (SACs). National Parks and Wildlife Service (NPWS) have mapped living and dead maerl dunes and beds using diver survey and acoustic techniques (RoxAnn) in Galway Bay and surrounding complexes (NPWS, 2013). Most of the maerl beds in Galway Bay are conserved as SACs. A diver survey of the Aran Islands maerl beds is still underway (Yvonne Leahy, *pers. comm.*).

Present day conservation policies on maerl in Ireland include protection under the EU Habitats Directive, with two species protected under Annex V, with indirect protection under Annex I (EC Council Directive 92/43/EEC).

They form part of Special Areas of Conservation (SACs), being part of the OSPAR (Oslo and Paris) Convention list of threatened and/or declining species. As a result conservation of maerl is also important basis for the formation of a network of Marine Protected Areas in Ireland (Johnson et al., 2008). In the UK it is also a UK Biodiversity Action Plan Priority Species.

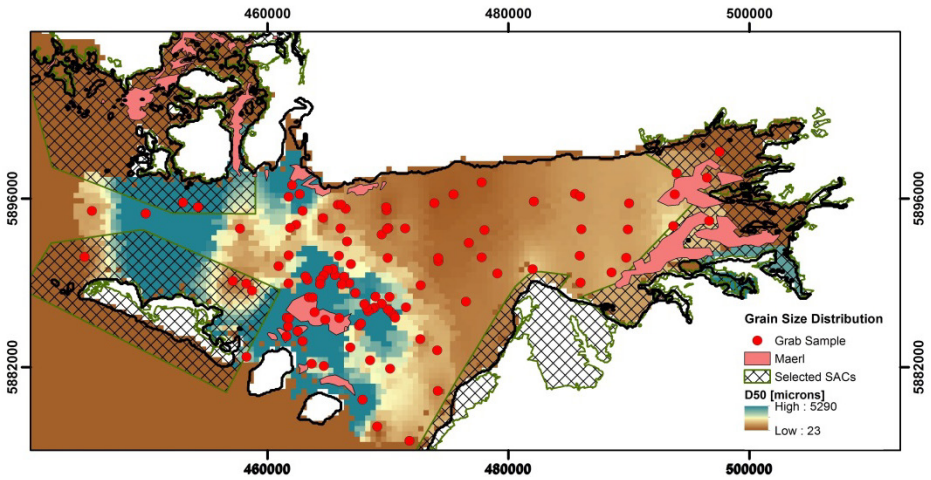

Figure 1.12: Distribution of the median diameter, *d50* of 110 grab samples of seafloor sediment obtained between March 2009 and August 2010, and maerl areas with the offshore Special Areas of Conservation (SACs).

1.3. Research Questions

1.3.1. Hydrodynamic Properties of Maerl

As a step towards integrating maerl beds into complex sediment transport models, it is necessary to carry out experimental work on the physical and hydrodynamic properties of maerl. Properties including the settling velocity, grain shape, grain size, grain density (submerged specific gravity) and critical bed shear stress have been experimentally determined in the laboratory. Therefore there are several research questions examined in Chapter 2 and Chapter 3 of the thesis. What is the settling velocity of maerl from three different environments in Galway Bay? How do the experimental results compare with theoretical models of settling velocity? How do factors such as grain shape of maerl influence its hydrodynamic properties? How can these be quantified and integrated into theoretical modelling? What is the critical bed shear stress for initiation of motion? Which is the optimum method (Law of the Wall, Turbulent Kinetic Energy or Reynolds Stress) to determine the critical bed shear stress of maerl?

1.3.2. Coupled Modelling

Coupled hydrodynamic-wave sediment transport models are potentially a useful tool for generating eco-geographical variables to utilise as part of habitat suitability models. The first step in the coupled modelling work flow is to run an initial barotropic hydrodynamic model to model the pure tidal currents and water levels. The water levels and tidal currents can be coupled into the spectral wave model. In order to model wave induced currents, the wave radiation stresses need to be coupled from the spectral wave model back into the hydrodynamic model, which is rerun to obtain wave induced currents. The outputs of the coupled hydrodynamic-wave sediment transport models can be integrated with hydrodynamic properties, for example, from the results of experimental work.

The research questions examined in Chapter 4 include: What is the relative importance of the different physical processes operating in Galway Bay, such as wave action, tidal currents, wave-induced currents, for the mobility of maerl-siliciclastic sediment? Which hydrodynamic parameters, such as

significant wave height, wave period, residual currents, depth-averaged shear velocity and orbital velocity at the seafloor, are the most influential on sediment mobility? How does their relative importance change from calm to storm conditions? Does sediment mobility modelling provide a more useful approach for understanding seafloor dynamics than sediment transport models? Can sediment mobility act as a physical surrogate for maerl-siliciclastic sediment? How can sediment mobility maps be used in marine spatial planning to minimise the disturbance of sensitive ecosystems?

1.3.3. Wider implications of Research

Habitat suitability models of maerl and related species are especially important for predicting the distribution of live maerl in areas where it is unknown (Guisan and Zimmermann, 2000; Martin et al., 2014). For a maerl-forming species in particular, sediment dynamics are important for quantifying the potential and realised niche of maerl. A key research question in Chapter 4 is: Which are the optimum eco-geographical variables for physical surrogacy studies on maerl?

More generally, a comprehensive understanding and a quantitative classification of benthic disturbance regimes has numerous applications for marine spatial planning. By modelling the transport pathways of maerl, it is possible to understand where to minimise anthropogenic activity such as bottom trawling and dredging for scallops from maerl beds or commercial extraction of maerl (Hall-Spencer, 1995). Although commercial extraction of maerl is not taking place in Galway Bay, understanding the unique behaviour of maerl from a sediment dynamics perspective has implications for neighbouring areas where extraction activity could impact maerl beds.

An understanding of the sediment transport pathways around a region is of great importance for managing conflict associated with anthropogenic activity. For example, the potential location of Europe's largest salmon farm close to the maerl beds at Inisheer could have detrimental effects on the maerl habitats, as has been shown in other areas (Hall-Spencer et al., 2006; Sanz-Lázaro et al., 2011). Monitoring and mitigating the transport of

pollution associated with increased coastal infrastructure such as sewage outfalls requires knowledge of the regional hydrodynamics. Structures on the seafloor at the ¼ scale wave energy test site could require an assessment of the sediment transport for scour protection.

This research can be used to inform geological facies models of carbonate production (Nebelsick and Bassi, 2000; Coletti et al., 2015). The construction of carbonate deposition models of rhodolith could be improved by quantifying regional variations in sediment mobility at the beginning of the process of deposition. This would improve the understanding of the biostratigraphy of fossil deposits of rhodoliths. If the physical properties of maerl can be determined from different hydrodynamic regimes, it may be possible to quantify the effects of water motion on rhodoliths in past environments.

1.4. Structure of Thesis and Summary of Papers

This thesis is divided into 6 main chapters. The rest of the thesis consists of Chapter 2, which is about "Settling velocity and grain shape of maerl." Chapter 3 discusses the experimental work to determine the critical bed shear stress of maerl using three different bed shear stress determination techniques in a rotating annular flume and straight flume. Chapter 4 looks at the sediment mobility modelling in Galway Bay. Chapter 5 is the thesis Conclusions and contains some recommendations for maerl conservation. This thesis has been structured around three publications, with details of the contribution of the author explained in following section.

1.4.1. Paper 1 Summary

Joshi, S., Duffy, G.P. and Brown, C. (2014) Settling velocity and grain shape of maerl biogenic gravel, Journal of Sedimentary Research 84(8) 718.

The settling velocity, grain shape and grain density are the first physical and hydrodynamic properties of rhodoliths which have been examined. The settling velocity of maerl is the fundamental sediment dynamics quantity which is primarily governed by the grain shape properties of maerl. Maerl settling velocity has been measured using settling tube measurements and the grain shape has been studied utilising detailed microscopic imaging. The grain shape of maerl is especially interesting to study as it varies with the amount of hydraulic energy present due to different degrees of abrasion. Three different hydrodynamic environments have been studied; beach, open marine and intertidal environment. A grain shape parameter known as the convexity was found to vary linearly with grain diameter, as the maerl structure becomes increasingly branched. The Ferguson and Church universal equation for settling velocity has been adapted to incorporate the linear increase in grain-size-dependent roughness (Ferguson and Church, 2004). Maerl experiences greater drag than the natural quartz grain and therefore has a lower settling velocity. Maerl tends to form beach deposits with a low percentage of sand and it is hypothesised that the lower settling velocity of maerl results in this preferential transport of biogenic maerl sediments compared to quartz sands and gravels. A combination of different wave climates and transport histories result in this increased spatial

variability of grain textures. The paper discusses to what extent a general equation for maerl settling velocity is possible. It makes recommendations on how the grain shape of grain size end members may be used to predict the settling velocity of maerl from different environments. Siddhi Joshi (SJ) carried out the settling velocity experiment with the laboratory assistance of Zoe Elliott, School of Geography. SJ carried out the grain shape analysis utilising the microscope and analysed the results using a modified version of a script by Mulchrone et al. (2013). Modifications of the script were carried out by SJ. SJ wrote the paper manuscript, Garret Duffy (GD) and Colin Brown (CB) edited the paper and CB suggested important revisions to the modelling of Ferguson and Church (2004) and Dietrich (1982).

1.4.2. Paper 2 Summary

Joshi, S., Duffy, G.P. and Brown, C. *In Prep.* Critical bed shear stress and threshold of motion of maerl biogenic gravels.

The second hydrodynamic property determined here is the critical bed shear stress, the force required to initiate motion of maerl biogenic gravels due to unidirectional currents. Three methods are utilised; Law of the Wall, Turbulent Kinetic Energy and Reynolds Stress. A rotating annular flume and straight flume have been utilised. Results have been analysed and plotted against the Shields curve with maerl falling below the Shields curve for quartz grains. Law of the Wall maerl critical bed shear stress experimental results are most reliable as they are multilevel measurements with a high R^2 value. Maerl subaqueous dunes formed at higher than the critical threshold velocity in the rotating annular flume. SJ carried out the experiment in Delft with laboratory assistance of Prof. Wim Uijttewaal's technical team at TU Delft in the Water Laboratory. Prof Leo van Rijn of Deltares/ Utrecht University has been acknowledged for providing suggestions to the experimental methodology during his visit to TU Delft. SJ carried out the analysis of the results to obtain the critical bed shear stress using the three methodologies and wrote the paper. GD and CB edited the paper with important suggestions. The paper was initially submitted to Journal of Sedimentary Research and reviewed by two anonymous referees, who made suggestions to improve the quality of the manuscript. These

changes were enacted by SJ and CB, and the paper will be resubmitted as a new submission to an international coastal dynamics journal.

1.4.3. Paper 3 Summary

Joshi, S., Duffy, G.P. and Brown, C. *In Prep.* Mobility of maerl-siliciclastic mixtures: impact of waves, currents and storm events.

This paper aims to quantitatively determine which dominant hydrodynamic processes govern the sediment mobility in Galway Bay, in particular in the maerl habitats. Sediment mobility is determined from hydrodynamic, wave and transport models using the DHI MIKE suite of modelling tools. The current induced sediment mobility and the combined wave-current induced sediment mobility are computed during calm summer conditions and extreme winter storm conditions. Maerl critical bed shear stress experimental results are incorporated into the models. A grid of spatially varying critical bed shear stress, with both maerl and quartz sediments has been computed using the Shields curve and experimental results. Two sediment mobility indices have been used; the Mobilization Frequency Index (MFI) and the Sediment Mobility Index (SMI). Results of the sediment transport model are also discussed as a comparison to sediment mobility modelling. The study finds that maerl prefers intermediate mobility environments. Models give insight into the hydrodynamic niche of maerl and the combined wave-current sediment mobility can be considered to be an abiotic surrogate for maerl. Sediment mobility indices can be partially correlated with multibeam backscatter and contribution of physical processes to disturbance has conservation applications. SJ carried out the coupled hydrodynamic sediment transport modelling in DHI MIKE 21 and performed the sediment mobility calculation. GD evaluated and assisted with the modelling methodology within DHI MIKE 21. SJ wrote the paper and produced the figures, CB evaluated the science and suggested important improvements. SJ has made all the changes prior to a submission to an international coastal dynamics journal.

2. Settling Velocity and Grain Shape of Maerl Biogenic Gravel

This chapter has been published as:
Joshi, S., Duffy, G.P. and Brown, C. (2014) Settling velocity and grain shape of maerl biogenic gravel, Journal of Sedimentary Research 84(8) 718.

Note for hardbound copy: Chapter 2 has not been reproduced in the digital version of the thesis due to copyright reasons and can be accessed online at Journal of Sedimentary Research archives at:
http://dx.doi.org/10.2110/jsr.2014.51

2.1. Abstract

The importance of a grain-size-dependent shape metric, convexity, for determining the unusual settling velocity characteristics of maerl, a variety of unattached coralline algae, has been quantified by modelling of settling-tube data. A modification of the general settling-velocity equation of Ferguson and Church (2004), involving a dependence of the drag coefficient-related constant, C_2, on grain size, produces a satisfactory fit to the experimental observations. For a given grain size and at Reynolds numbers greater than ~ 220, maerl grains experience greater drag than is predicted for natural quartz grains by Ferguson and Church (2004) because of this grain-size-dependent roughness. Subsequent detailed measurements of maerl grain shape using microscopic image analysis confirm a strong positive linear relationship between grain roughness, quantified by the reciprocal of convexity, and grain size.

This departure from the ideal settling characteristics of siliciclastic gravel is hypothesized to explain the observed propensity of maerl, under suitable hydrodynamic conditions, to form beach deposits with a low percentage of sand. Maerl samples from three different sedimentary environments (open marine, intertidal, and beach) exhibit different linear relationships between roughness and grain size, probably resulting from different degrees of abrasion due to a combination of different wave climates and transport histories. This spatial variability in grain texture suggests that a general equation for maerl settling velocity is not possible. However, for maerl, and other branched sediment types, it may only be necessary to measure the convexity of the middle and largest size fractions to estimate the linear variation of C_2 with grain size.

Our results indicate that, over a range of bottom current conditions between 200 and 250 mm s^{-1}, where the settling curve of maerl is flat and grain-size invariant relative to siliciclastic sediment, a larger part of the maerl grain-size distribution can remain in suspension compared to the siliciclastic sediment. This contrast in physical properties may be an effective process for the spatial separation of coarse siliciclastic and biogenic sediment.

2.2. Introduction

Particle settling velocity is a fundamental sediment property that influences the rates of vertical flux, entrainment, deposition, and sorting of particles suspended in a fluid (Fredsøe and Deigaard, 1992; Ferguson and Church, 2004). It is a key parameter to include in coupled hydrodynamic-wave-sediment transport models of rivers, estuaries, and deltas, and for the quantitative evaluation of coastal and marine morphodynamics (Van Rijn, 1993; Strom and Keyvani, 2011). Knowledge of hydrodynamic properties, such as the settling velocity and the critical bed shear stress, is a crucial prerequisite to modelling sediment mobility in coastal environments.

Biogenic sediment does not exhibit the scale-invariant crystalline properties of siliciclastic sediment, and is generally highly irregular in grain shape (Smith and Cheung, 2003), which is a key parameter affecting the drag resistance force of a moving particle (Dietrich, 1982). In spite of this situation, relatively little work has been carried out on the hydrodynamic characteristics of calcareous biogenic material, especially calcareous algae or "maerl." This paper addresses that knowledge gap.

The velocity at which the upward force of drag resistance exactly opposes the downward force of gravity is known as the terminal fall, or settling, velocity, w_s (Hallermeier, 1981; Fredsøe and Deigaard, 1992; Van Rijn, 1993). The equilibrium for a spherical particle of diameter, d, is shown (Eq. 2.1), where the terms related to the combined actions of buoyancy and gravity on the left-hand side are equal to the drag resistant term on the right-hand side:

$$(\rho_s - \rho) g \frac{\pi}{6} d^3 = C_D \frac{1}{2} \rho w_s^2 \frac{\pi}{4} d^2 \tag{2.1}$$

where ρ_s and ρ are the densities of the sediment and fluid, and C_d is the drag coefficient.

All particle settling-velocity curves can be divided into three regions: the region dominated by viscous drag known as the Stokes region, the transitional region where there is greatest uncertainty in prediction, and the

Newtonian or inertial region where the turbulent drag of the wake behind each grain is the predominant resisting force (Ferguson and Church, 2004; Bosboom and Stive, 2013). In the Stokes region, corresponding to small particles and Reynolds number, $\mathrm{Re} = w_s d/v$ less than one, the solution of the equations of motion for Stokes flow for perfect spheres yields

$$w_s = \frac{Rgd^2}{18v} \tag{2.2}$$

where $R = \rho_s/\rho - 1$ is the submerged specific gravity and v is the kinematic viscosity coefficient, representing the fluid's internal resistance to flow (Stokes, 1851). Substituting Equation 2.2 into Equation 2.1 allows determination of the drag coefficient C_d for particles in the Stokes region:

$$C_D = \frac{24}{\mathrm{Re}} \tag{2.3}$$

In the Newtonian region where $\mathrm{Re} > 1000$, the combined effect of grain shape and/or roughness plays a greater role, resulting in a settling velocity

$$w_s = 1.6\sqrt{Rgd} \tag{2.4}$$

Other authors, e.g., Van Rijn (1993), have suggested a different coefficient.

Ferguson and Church (2004) proposed a dimensionally correct explicit model, which fulfils the criteria of Stokes' Law of settling for small, irregular, permeable grains and the constant drag coefficient for large grains. Building on previous work (e.g., Dietrich (1982), Cheng (1997)), they introduce two parameters, C_1 and C_2, which allow for variations in grain shape:

$$w_s = \frac{Rgd^2}{C_1 v + (0.75\, C_2 Rgd^3)^{0.5}}. \tag{2.5}$$

Equation 2.5 provides an accurate prediction of the settling velocity in the transitional region ($1 < \mathrm{Re} < 10^3$) or ($0.1\ \mathrm{mm} < d < 4\ \mathrm{mm}$) for quartz sand. The equation largely preserves the physical criteria in all three regions in its simplest form, and accounts for shape effects by varying the parameters C_1

and C_2 for a given sediment type. The values of C_1 and C_2, which correspond to smooth spheres, are $C_1 = 18$, $C_2 = 0.4$, and for natural grains are $C_1 = 18$, $C_2 = 1$. Ferguson and Church (2004) express the drag coefficient in terms of C_1 and C_2 as

$$C_D = \left(\frac{2C_1 v}{\sqrt{3RgD^3}} + \sqrt{C_2} \right)^2 \tag{2.6}$$

This study determines settling-velocity curves for maerl biogenic sediment, and tests the validity of Ferguson and Church's equation for settling velocity for this specific sediment type. It proposes a modification to Equation 2.5 for highly irregular maerl grains that exhibit a dependence of shape on grain diameter. This result requires the C_2 parameter of the Ferguson and Church (2004) model to vary linearly with grain diameter.

2.2.1. Maerl

The ecological and economic importance of free-living, unattached, non-geniculate coralline red algae, known as maerl or rhodolith, has been studied over the last 30 years (Maggs, 1983; Birkett et al., 1998; BIOMAERL, 1999; Foster, 2001; Bassi et al., 2012). However, the hydrodynamic parameters of maerl have received very little attention from the research community. Maerl beds, together with kelp beds, seagrass meadows, and coral reefs, are one of the four largest macrophyte-dominated benthic communities in the world (Foster, 2001). Maerl reproduces by fragmentation of thalli during vegetative propagation, as well as by the production of spores (Birkett et al., 1998; Mitchell, 2001). Maerl beds support high biodiversity and an abundance of rare epifauna and epiflora (Keegan, 1974; Maggs, 1983; Kamenos et al., 2004a). They are important nursery grounds for juvenile stages of molluscs, crustaceans, and commercially important fish (Hall-Spencer (Hall-Spencer, 1998; Kamenos et al., 2004a). As major carbonate producers, maerl beds are globally significant carbon sinks (Amado-Filho et al., 2012).

Maerl beds are restricted to the euphotic zone and are intolerant of high suspended-sediment concentrations. Anthropogenic disturbances such as

fishing activity via trawling, commercial extraction, organic matter input from aquaculture, and scallop dredging, have been found to have an adverse effect (Hall-Spencer and Moore, 2000; Grall and Hall-Spencer, 2003). There are currently maerl beds along the Atlantic coasts of Ireland, Scotland, and Norway; the coasts of the Mediterranean; Gulf of California; north-eastern Canada; eastern Caribbean; Brazil; southern Japan; and Western Australia (Foster, 2001). In Europe, the maerl species under study *Lithothamnium corallioides* and *Phymatholithon calcareum*, are two of 67 plant and animal species listed in Annex V of the EC Habitats Directive, whose exploitation may be subject to management restrictions (EC Council Directive 92/43/EEC). Some occurrences of maerl are also subject to indirect protection under Annex I, i.e., they may constitute a "natural habitat type in danger of disappearance" (EC Council Directive 92/43/EEC). Understanding the sediment mobility of biogenic maerl gravel is relevant to the Seabed Integrity "Good Environmental Status" descriptor, as part of the Marine Strategy Framework Directive (EC Council Directive 2008/56/EC). Maerl beds are also included on the Oslo and Paris Convention's List of Threatened and/or Declining Species and Habitats (OSPAR 2013). In Ireland, gravel beaches and dunes of dead and live maerl receive protection, and form a part of Special Areas of Conservation (SAC), as well as OSPAR Marine Protected Areas.

2.2.2. Previous Studies

Environmental and hydrodynamic controls on maerl grain morphology have been the subject of much research. Bosence (1983) produced a morphological classification of rhodoliths, based on the ranges of similar branch density, and characterized the structure of rhodoliths as either laminar, branching, or columnar, an ecophenotypic response to the hydraulic energy present. Burgess and Anderson (1983) recognized that more immobile rhodoliths have a more columnar structure. Steller and Foster (1995) found that outside the wave-breaking zone, branch density correlated inversely with depth. Marrack (1999) found that shallow wave-dominated maerl beds (< 4.5 m depth) were more exposed to wind-generated waves and more mobile than deeper beds farther offshore, which

are disturbed only by bioturbation or severe storms. Foster (2001) analysed the fragmentation of rhodoliths with increasing water motion, and found that low water motion leads to irregular shapes, moderate water motion leads to spherical shapes, and high water motion leads to fragmentation.

In the more general case of biogenic sediment, Paphitis et al. (2002) determined the settling velocity and entrainment thresholds of shell fragments of the common cockle, *Cerastoderma edule*, and the common mussel, *Mytilus edulis*. Smith and Cheung (2003) determined the settling velocity of heterogeneous calcareous sand from beaches in Hawaii. Smith and Cheung (2003) found that irregular-shaped particles induced turbulence, leading to the breakup of the laminar boundary layer at lower grain Reynolds numbers. Weill et al. (2010) determined the settling velocity and threshold of motion of coarse bioclastic sand from shelly cheniers in France, and estimated their Nikuradse roughness lengths. Pugh and McCave (2011) studied the settling velocity of diatom frustules as a method of determining particle size, as well as determining their porosity and density. Alcerreca et al. (2013) produced a simple equation for calcareous sand in Mexico (coral fragments, ooids, and skeletal mollusc deposits) that relates the non-dimensionalised grain size to the grain Reynolds number. Differential sediment transport by hydraulic sorting has been observed in many depositional environments, including wave action forming ridge like structures known as coral stick ramparts (Folk and Robles, 1964).

2.2.3. Study Site

This study examined the settling-velocity characteristics of maerl collected from three different hydrodynamic regimes in Galway Bay, west of Ireland. The Carraroe biogenic gravel beach is located in Greatman's Bay, the Aran beds are found in an exposed open marine setting northeast of Inishmaan, and the Muckinish intertidal beds are near Finavarra, County Clare (Figure 2.1). The Muckinish bed was sampled during a low spring tide, and the Aran sample was acquired using a Day grab deployed from the *RV Celtic Voyager*. The Carraroe sample was obtained from the swash zone adjacent to the berm as surficial sediment. The Aran Islands bed is found at a depth

of 26 m and is subject to storm wave action, with wave-generated sorting of disaggregated bivalves and shell hash found in nearby rippled scour depressions. The Carraroe maerl beach is subject to mean summer significant wave heights (SWH) < 0.6 m during the summer according to a validated, finite-volume, spectral wave model developed for a separate part of the study using commercial software (See Section 4.3). Muckinish is sheltered, experiencing SWHs of up to only 0.3 m during the strongest summer storm.

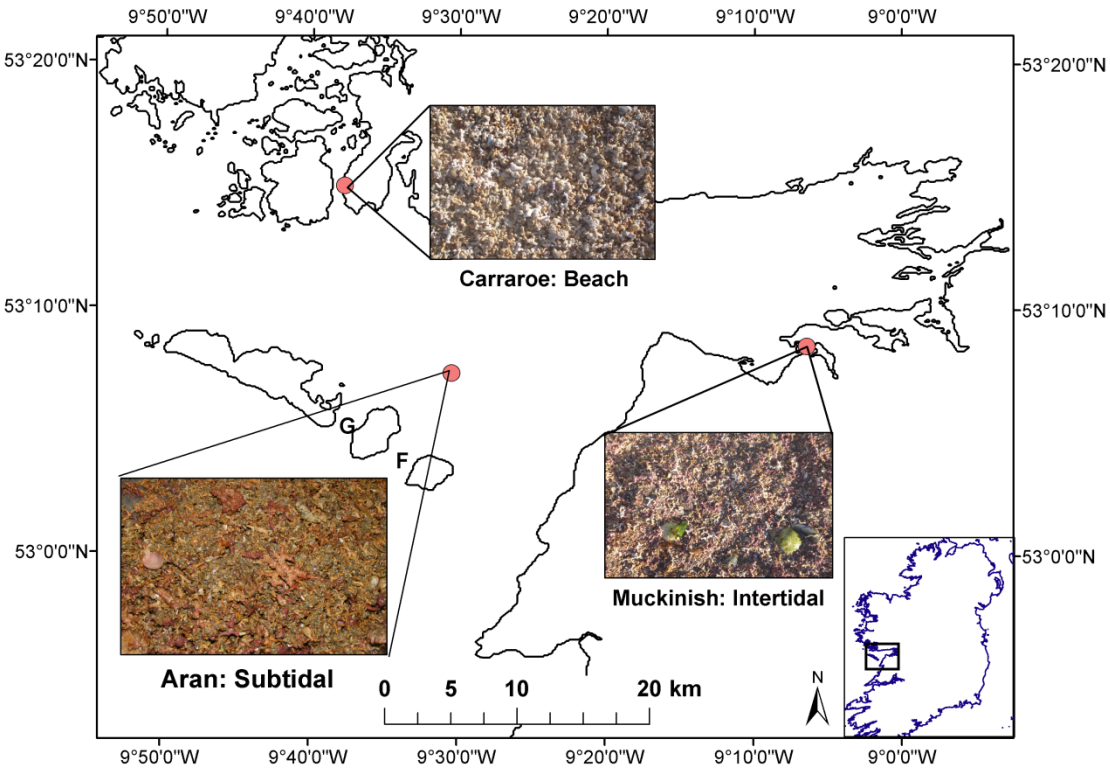

Figure. 2.1: Maerl sample locations in Galway Bay, west coast of Ireland, with three different hydrodynamic regimes that include beach sediment, an intertidal bed, and an open marine bed. The images of the maerl represent a footprint of 0.25 m by 0.10 m on the seafloor. F, Foul Sound; G, Gregory Sound.

2.3. Materials and Methods

2.3.1. Settling-Velocity Methodology

Preparation — Natural sediment was dried in an oven at 60°C for 48 hours and separated into half-phi fractions, using a Retsch sieve shaker, from 500 µm to 32 mm. The settling velocity of each size fraction was measured with three replicates to estimate accuracy. As recommended in Gibbs (1972), a settling tube 2 m tall × 0.18 m wide was used with a settling length of 1.4 m (Figure 2.2). A 0.4 m section of the tube was marked at the top of the tube, to allow the terminal fall velocity to be reached, with a 1 m section utilized for the particle travel-time measurement. The experiment was repeated at two salinities: 0 and 35 ppt. A water bath with a salinity probe was used to obtain a salinity of 35 ppt, with the addition of table salt (NaCl). The salt was slowly added and dissolved by stirring the water bath until the salinity probe reached a salinity of 35 ppt. The salinity and temperature were maintained in the water bath and in the full length of the settling column prior to the experiment to minimize thermal convection (Syvitski, 1991). The room temperature was thermostatically controlled by air conditioning to be 20°C. Prior to the experiment, water in the settling column was allowed to settle with minimal internal circulation (Syvitski, 1991).

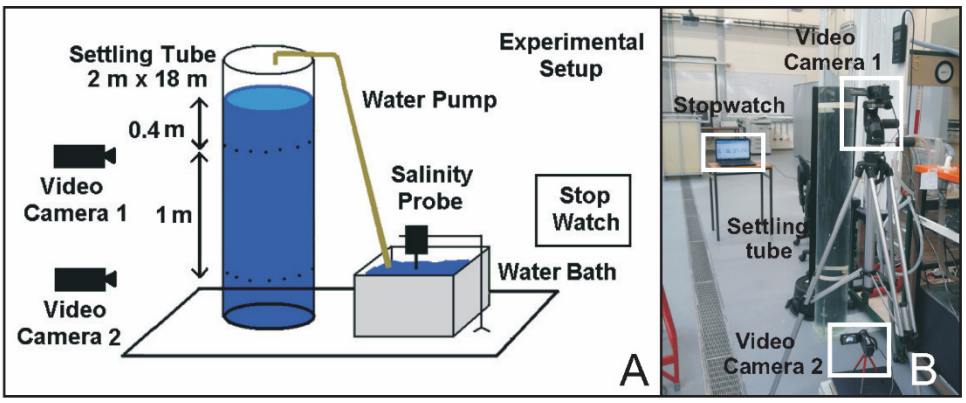

Figure 2.2: **A)** Experimental setup for measuring maerl settling velocity, with **B)** a settling tube monitored at two points either side of a 1 m section by two video cameras.

Experiment — Approximately 10–100 grains of dried maerl sediment were released into the centre of the column to minimize the influence of the settling-tube wall. The sample introduction method was kept consistent in that grains were saturated, allowed to be immersed into the water column first and then allowed to naturally fall down through the settling tube. In some cases, smaller grains formed a film at the top of the tube. This film was agitated and removed prior to each run to prevent these grains from falling and interrupting the subsequent runs. Any voids which were present could give rise to some buoyancy so were left to immerse in water prior to being released. The travel time of the fastest-falling particle was measured using a high-precision stopwatch prominently displayed on a computer monitor and recorded on video. Two high-definition video cameras (Sony SD Handycam® 67× Extended Zoom) were mounted on tripods horizontally adjacent to the top and bottom of the 1 m section mark. The computer display was visible in the far field of both video images. As most of the maerl particles were light coloured, a black background was used to maximize the contrast and ensure a uniform background in the video imagery. The column was illuminated to ensure that the smallest particles were visible in the settling tube. The focus was manually set to infinity to be able to view both the near field (particle) and far field (computer display) simultaneously. Some qualitative visual observation of the grain trajectories and primary and secondary motions (Allen, 1985) was possible in both real time and after processing. A small number (< 5%) of falling grains exhibited both rotation and nonlinear fall trajectories, and those observations of slow fall velocity were rejected. The inclusion of slow settling-velocity measurements arising from nonlinear fall trajectories or rotation would be reasonably expected to cause an even greater departure from the Ferguson and Church (2004) model as it stands, with the slow fall measurements excluded, the rate of change of fall velocity with grain size is already very low or grain-size invariant. It is difficult to assess what effect, if any, the inclusion of a slightly greater number of slower-velocity determinations would have on the observed trend of the settling velocity data. Hindered settling, when the high concentration of particles results in alteration of the free flow of other particles due to the presence of surrounding particles (van Rijn, 2007b), was not a major issue due to the low concentration of the

material. When this did occur, grains were found to lock together during the fall and flocculate. In such cases, the measurement was rejected.

Error Estimation — The settling-velocity estimate and its accuracy were obtained using

$$w_s = f(\Delta d, \Delta t) = \frac{\Delta d}{\Delta t} = \frac{(d_b - d_t)}{(t_b - t_t)} \tag{2.7a}$$

$$\sigma_{w_s}^2 = \left(\sigma_{tt}\frac{\partial f}{\partial t_t}\right)^2 + \left(\sigma_{tb}\frac{\partial f}{\partial t_b}\right)^2 + \left(\sigma_{dt}\frac{\partial f}{\partial d_t}\right)^2 + \left(\sigma_{db}\frac{\partial f}{\partial d_b}\right)^2 \tag{2.7b}$$

where $\sigma_{W_S}$is the settling-velocity error, σ_{tt} and σ_{tb} are the errors in the travel-time measurements at the top (t_t) and bottom (t_b) cameras, and σ_{dt} and σ_{db} are the errors in the distance measurements at the top (d_t) and bottom (d_b) distance markers. During data processing, each frame captured just before and after the particle crossed the mark was analysed in SM Player software (Smplayer, 2014). This technique gave an error of the time measurement in both cameras of 0.1 second, at the constant 15 frames per second (fps) recording speed. The point at which a particle crossed a distance marker was photographed at 15 fps, giving a distance error of 2 mm at each camera. For a typical measurement of 220 mm s^{-1}, the estimated error is 7 mm s^{-1}.

2.3.2. Grain-Shape Methodology

Grain shape properties were analysed to quantify how the mechanical properties of maerl affect the settling velocity. A two-dimensional image was measured accurately using digital image techniques and the grain-shape distribution of 10 particles per size fraction was quantified, i.e., 90–100 grains were analysed quantitatively per sample location, resulting in a total of ~ 270 images.

Microscope Imaging.— A Leica WILD M3Z microscope (6.5–40× magnification) with mounted Nikon Coolpix 995 camera was used for an analysis of grain-size fractions with midpoints 1.7 mm to 9.6 mm in half-phi increments. The advantages of an accurate two dimensional measurement were considered to outweigh the disadvantages of using this 2D technique for the estimation of the 3D particle roughness. Individual grains were

mounted on stubs according to their size fraction. Care was taken to ensure that the grain was orientated so that the longest and intermediate axes could be imaged on a two-dimensional plane. This approach helped to minimize out-of-plane roughness. An estimate of the variability of the irregular grain shape within a fraction was obtained by measuring 10 grains per size fraction.

Image Analysis.— Images were analysed using the Component Measurement tools in the Wolfram Mathematica software package, using a modified version of the script described in Mulchrone et al. (2013). The image was pre-processed using basic image-processing filters (contrast enhancement, edge detection) and subsequently binaries (Figure 2.3). Three grain-shape metrics (caliper elongation, circularity, and convexity) were selected to quantify different aspects of the grain morphology recorded in a two-dimensional image (Malvern, 2013). The fractal dimension was calculated to explore the significance of fractal geometry on the variability of the grain shape (Strom and Keyvani, 2011). The caliper elongation, E, is a measure of the particle form and is not sensitive to edge roughness:

$$E = 1 - \frac{a}{b} \tag{2.8}$$

where a and b are minor and major axes obtained using the Feret diameter, defined as the distance between two parallel planes, such as a caliper, restricting the object perpendicular to that direction (Wolfman, 2013). The more rod-like the particle is, the higher the caliper elongation. The circularity, Y, is quantified as the deviation from the circular equivalent area to the irregular grain:

$$Y = \frac{p_{eq}}{p} \tag{2.9}$$

where p_{eq} is the equivalent disk perimeter, i.e., the perimeter of a circle with the area equating to the irregular grain, and p is the perimeter length. The convexity, C, is a perimetric property and a measure of the roughness of the grain:

$$C = \frac{p_h}{p} \tag{2.10}$$

where p_h is the convex hull perimeter; i.e., the "elastic band"–like length measurement encapsulating the roughness within the plane (Figure 2.3). Hence, a circle would have a convexity of 1 and an irregular shape would have a convexity < 1. The convexity can be used as an indicator of grain roughness and complexity of the micro topography of a sediment particle (Malvern, 2013). In the case of maerl, convexity is considered to be inversely proportional to the branch density of maerl, a parameter that has previously been found to decrease with depth (Steller and Foster, 1995).

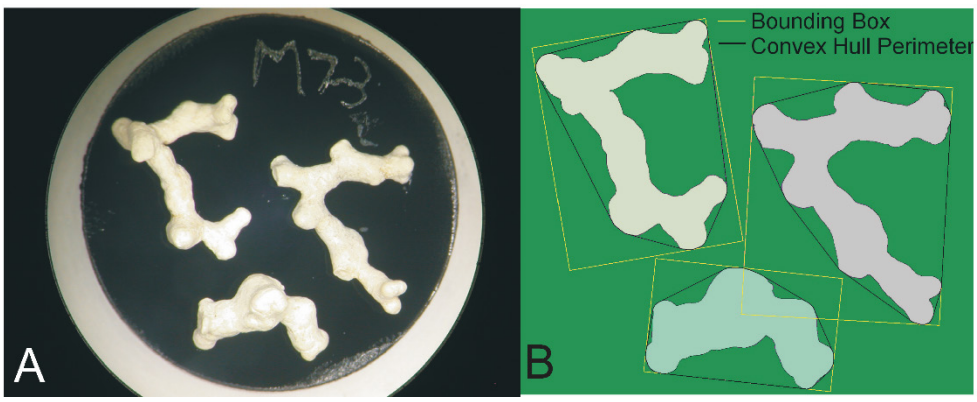

Figure 2.3: **A)** A microscope image of a 2.5 cm diameter stub with maerl grains from the intertidal bed. This is an example of highly irregular maerl with a low convexity value. **B)** A binarized image with grain perimeter, bounding box, and convex hull perimeter.

The fractal dimension, d_p, was calculated using the image area and perimeter (Maggi, 2005):

$$d_p = 2\frac{\log[p]}{\log[A]} \tag{2.11}$$

where A is the area of the projected image.

2.3.3. Sediment Density

The submerged specific gravity is required for accurate estimates of the parameters C_1 and C_2 (Equation 2.5). Given the unique nature of maerl, the sediment density was estimated by way of laboratory experiment. The

British standard of BS 1377-2:1990 was followed, with a modification for the quantity of sediment and with the use of deionized water. The density of the sediment at room temperature was calculated as the product of water density and specific gravity of the sediment using

$$\rho_s = \mathrm{J}(\rho, M_1, M_2, M_3, M_4) = \rho \frac{(M_2 - M_1)}{(M_4 - M_1) - (M_3 - M_2)} \tag{2.12}$$

where M_1 is mass of glass jar, M_2 is mass of glass jar partially filled with maerl only, M_3 is mass of jar partially filled with maerl then completely filled with water, and M_4 is mass of jar completely full of water only. Quality control of the density measurements was ensured by making two replicate subsamples per sample site, with the result deemed of an acceptable quality if both glass jars gave a measurement within 30 kg m^{-3} of each other at all three stages of measurement of M_3. The accuracy of individual measurements was estimated by propagation of error:

$$\sigma_{\rho s}^2 = \left(\sigma_\rho \frac{\partial J}{\partial \rho}\right)^2 + \left(\sigma_{M1} \frac{\partial J}{\partial M_1}\right)^2 + \left(\sigma_{M2} \frac{\partial J}{\partial M_2}\right)^2 + \left(\sigma_{M3} \frac{\partial J}{\partial M_3}\right)^2 + \left(\sigma_{M4} \frac{\partial J}{\partial M_4}\right)^2 \tag{2.13}$$

where $\sigma_{\rho s}$ is the sediment density error, σ_ρ is the water density error (dependent on σ_t, the water temperature error), and σ_{M1} to σ_{M4} the mass errors for M_1 to M_4, respectively. A water-temperature error of 0.5°C gave an error in $\sigma_{\rho s}$ of $\pm$ 0.75 kg m^{-3} (Van Rijn, 1993). The scales were accurate to $\pm$ 0.0001 kg and this corresponded to the σ_{M1} to σ_{M4}.

2.4. Results and Analysis

We assessed the bulk density of oven-dried whole samples, which had varying fractions of shelly or sandy material. The Carraroe sample has a value of 2629 ± 16 kg m^{-3}; Aran, a value of 2588 ± 16 kg m^{-3}; and Muckinish, a value of 2437 ± 14 kg m^{-3}. The low density of the Muckinish maerl sample, compared to the density of pure calcium carbonate (~ 2710 kg m^{-3}) from which the maerl internal lattice is chiefly composed, is probably due to the high internal porosity of the live maerl in Muckinish (Jazmin Hernandez-Kantun, *pers. comm*.). The presence of a high number of internal voids and laminations due to growth "episodes" results in a decreased density of the live maerl, with figures as low as ~1982 kg m^{-3} (specific gravity 1.93 ± 0.13) reported by Harris et al. (1996). The high density of the Carraroe (beach) maerl sample is because wave action has broken the maerl branches and abraded the maerl surfaces thereby reducing grain porosity and effectively increasing grain density, cf. Bucher et al. (1998). Age related consolidation is also occurring at Carraroe (Christine Maggs, *pers.comm.*) The Muckinish measurement was judged to be a representative value of the density of live maerl and was used for ρ_s in Equations 2.1, 2.2, 2.4, 2.5, and 2.6.

The settling-velocity results were compared to values predicted from equations for settling velocity as a function of diameter in Dietrich (1982) and Ferguson and Church (2004). The empirical Equation 19 in Dietrich (1982) is based on a statistical analysis of settling-velocity experiments with natural sediment, and it contains a term (equation 18 of Dietrich (1982)) that accounts for the grain angularity characterized by the (Powers) roundness index (R_3),

$$R_3 = \left[\alpha - \left(\left(C_{sf}/\beta\right) tanh(log_{10}\ d_* - \gamma)\right)\right]^{1+(\delta - P)/\varepsilon} \tag{2.14}$$

where $d_*$is the dimensionless particle size (related to the grain diameter), C_{sf}, the Corey shape factor ($0 < C_{sf} < 1$) characterizing the grain shape, and $\alpha, \beta, \gamma, \delta, \varepsilon$ are empirical constants derived to fit the data. The maerl data from the experiments were inverted to obtain values of $C_{sf}$and P using the values of the empirical constants provided in Dietrich's equation 18. The

best fitting curves required $C_{sf} > 1$ and $P > 6$, and curve fits were poor. For both scales to be constrained to their conventional limits, Equation 2.14 must be rescaled by adjusting some of the empirical constants. If, for example, $\alpha \sim \beta \sim 1$ and the other constants are retained as in Dietrich (1982), the curves for the three locations can be forced to fit observed settling-velocity data reasonably well (coefficient of determination, r^2 between 0.95 and 0.97) with $0.75 < C_{sf} < 1$ and $3.1 < P < 3.5$, the roundness values being similar to those of an irregular coarse sand. If C_{sf} and P are allowed to vary with grain size, the goodness of fit is improved marginally (r^2 between 0.97 and 0.99). Therefore, the formulation in Dietrich (1982), based upon siliciclastic sediment experiments, can be generalized to provide a predictive model for the settling velocity of biogenic maerl particles, which exhibit physical properties different from those of siliciclastic sediment. We note that the Dietrich (1982) model requires the determination of four free parameters, of which α and β have no obvious physical interpretation.

The second approach, based on Ferguson and Church (2004), has been used to generate end members of settling-velocity curves as a function of grain diameter (Figure 2.4), for smooth spheres (constant $C_1 = 18$ and $C_2 = 0.4$) and highly angular quartz grains (constant $C_1 = 24$ and $C_2 = 1.8$), These results show a systematic, grain-size-dependent discrepancy with the data for grain sizes greater than ~ 1 mm. The data for these grain sizes cannot be reproduced by intermediate model curves in the same range, but the data at diameters less than ~ 1 mm (in the viscous region) do indicate a convergence on the curve for smooth spheres. Overall, the data suggest that the decrease in the rate of change of observed settling velocity with diameter (> 1 mm) is due to the change in shape and/or angularity of maerl with diameter. This hypothesis is supported by the results from the grain-shape measurements below (Figure 2.5).

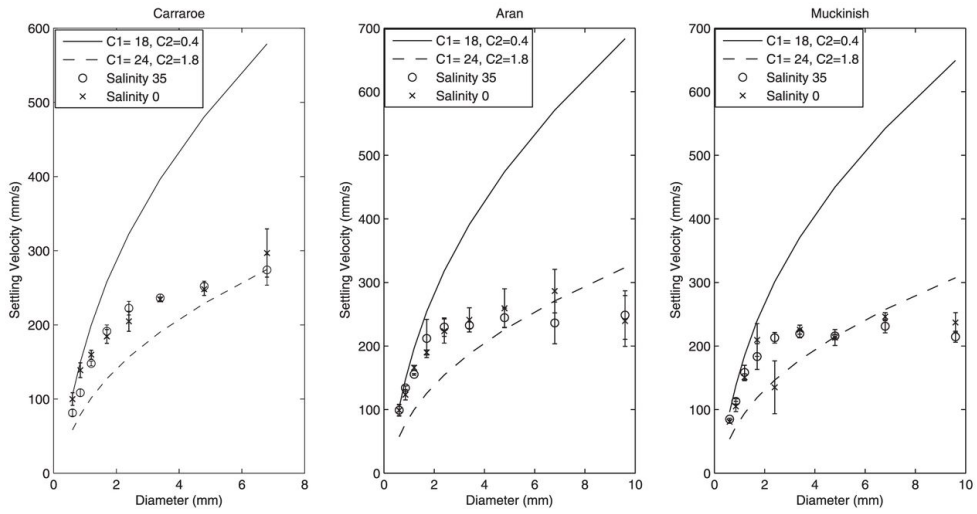

Figure 2.4: Settling velocity versus sieve diameter with two Ferguson and Church (2004) model curves using constant C_1 and C_2. The $C_1 = 18$, $C_2 = 0.4$ curve is for smooth spheres; the $C_1 = 24$, $C_2 = 1.8$ is for highly angular quartz grains.

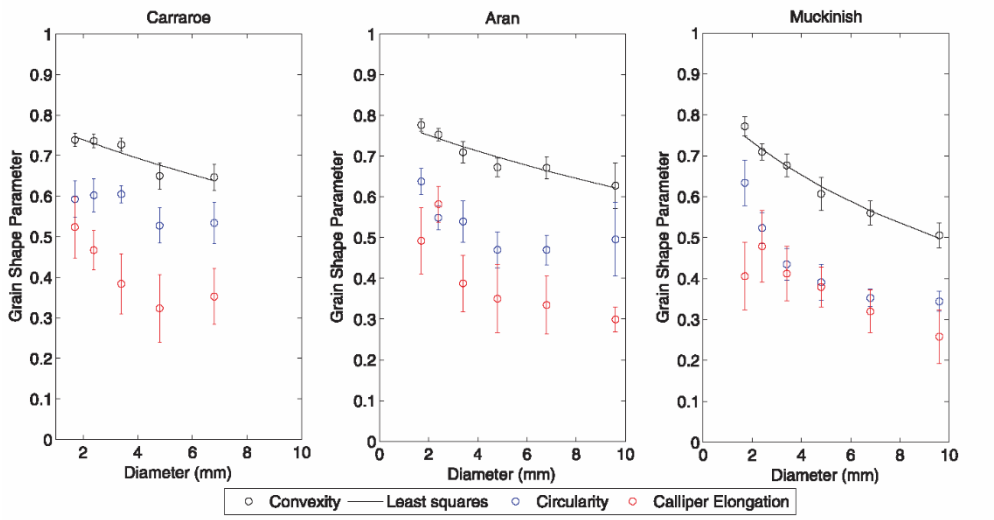

Figure 2.5: Grain-shape parameters (convexity, circularity, and caliper elongation) for the three samples versus sieve diameter. The reciprocal of convexity increases linearly with diameter. The solid line represents the least-squares fit between the reciprocal convexity and diameter, plotted as the convexity versus diameter. The coefficient of determination is $r^2 > 0.9$ for each sample.

Convexity and circularity are found to co-vary and decrease with increasing diameter, and caliper elongation is also found to decrease with increasing diameter. Numerical tests with least-squares curve fitting suggest that the *reciprocal* of convexity increases linearly with diameter, particularly in the

most accurate measurements on the Muckinish samples, suggesting that convexity decreases with increasing branch density. Muckinish convexity also has the largest gradient, suggesting that gravel-size grains from these intertidal maerl beds exhibit the highest branch density. The Carraroe beach samples show the smallest degree of within-bin variability, denoted by the error bars, indicating that they are the most regular in shape, a conclusion consistent with their relatively high circularity. In general, convexity variability is less than the circularity and caliper elongation variabilities, reflecting the strength of the ability of this grain shape-parameter to quantify the highly irregular nature of maerl. Grains also become less circular with increasing diameter as the branching increases. The fractal dimensions of the maerl samples are typically 1.36 ± 0.02 for Carraroe and Aran and 1.41 ± 0.05 for Muckinish.

The variation in these grain-shape parameters with diameter is consistent with the inability to model maerl settling-velocity data with grain-shape parameters that are invariant with grain diameter. Initially, we hypothesized that both C_1 and C_2 vary according to $C_j = C_{j0} + C_{j1}\ d$, ($j = 1, 2$). The observed settling-velocity data were fitted using a variety of constrained and unconstrained inversions to estimate the four unknown parameters. The results demonstrated that: (1) C_2 is strongly dependent on grain diameter; (2) the goodness of fit decreases insignificantly (r^2 decreases by $< 0.2\%$) if $C_{11} = 0$, an unsurprising result given that the grain Reynolds numbers for these samples ($40 < \mathrm{Re} < 2000$) are much higher than those appropriate for the Stokes regime; and (3) inversions constrained so that C_1 was allowed to vary no lower than 16 (to allow for particle shapes that are more hydrodynamically efficient than perfect spheres where $C_1 = 18$) gave stable and consistent results for C_1 ($33 < C_1 < 42$) and $C_{20} = 0$.

The preferred fits to the observed settling velocities were calculated with this modified Ferguson and Church (2004) model where $C_2 = C_{21}\ d$ and $C_1 > 16$ (Figure 2.6). The values for C_1 and C_{21} are: 42 ± 2 and 265 ± 8; 33 ± 3 and 284 ± 6; 38 ± 3 and 352 ± 6 for Carraroe, Aran, and Muckinish grains, respectively.

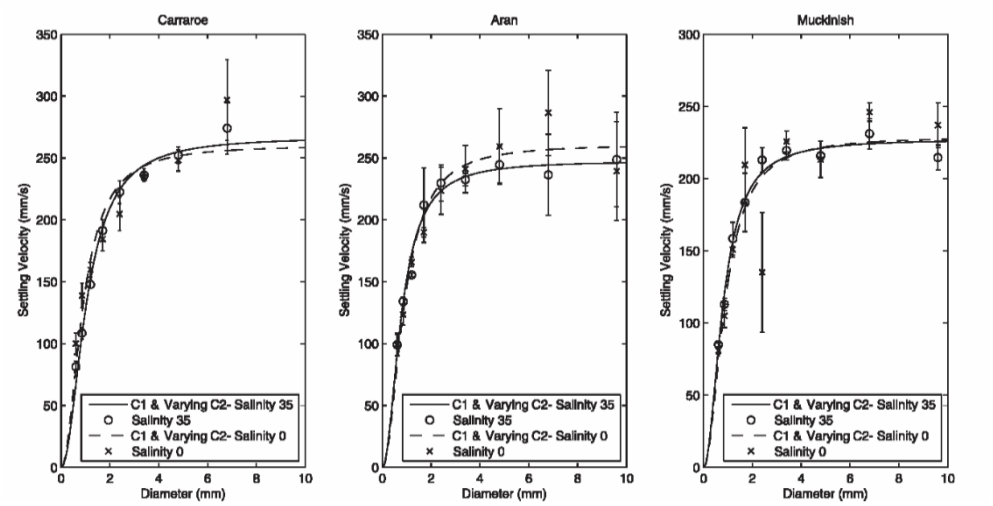

Figure 2.6: Settling velocity versus diameter using the modified version of the Ferguson and Church (2004) model, where C_2 is allowed to vary linearly with diameter. The coefficients of determination, r^2 for the model curves and observed data vary between 0.95 and 0.97 for experiments with salinity of 35 ppt; they are lower for the freshwater experiments due to data outliers.

C_2 and the drag coefficient C_d vary with diameter (Figure 2.7). The drag coefficient correctly converges to the asymptotic value of C_2 as diameter increases (Ferguson and Church, 2004). SEM images of the internal structure of the maerl frame indicate that the particles are impermeable (Strom and Keyvani, 2011), so the diameter dependency of C_2 is ascribed solely to the effect of the increasing complexity in the shape of impermeable (solid) maerl particles, which increases the drag coefficient in the intermediate regime.

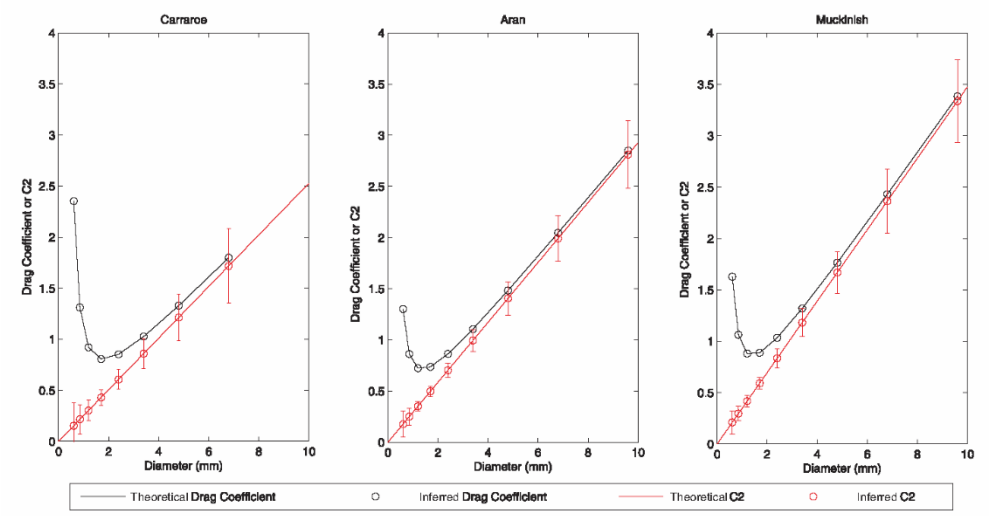

Figure 2.7.: The parameter C_2 and the drag coefficient as a function of sieve diameter. The drag coefficient and C_2 inferred from the settling-velocity inversions are compared with their theoretical values from the Ferguson and Church (2004) model modified to account for the linear variation of C_2 with diameter.

The drag-coefficient estimates for the three maerl samples are plotted (Figure 2.8) against grain Reynolds number and compared with previous data for a range of grain shapes (Komar and Reimers, 1978), quantified by their three-dimensional Corey shape factors (Blott and Pye, 2008). The latter curves span the transition regime at intermediate grain Reynolds numbers ($1 < \mathrm{Re} < 10^3$). Local minima are observed in the maerl curves at $\mathrm{Re} \sim 220$, after which the grain-shape effects of the maerl start to dominate the hydrodynamic behaviour. Maerl drag coefficients increase at the largest measured Reynolds numbers and diameters, and cross the curves that correspond to increasingly irregular grain shapes. It is envisaged that the maerl drag coefficients will reach an asymptotic value at grain sizes larger than the maximum size used in these experiments.

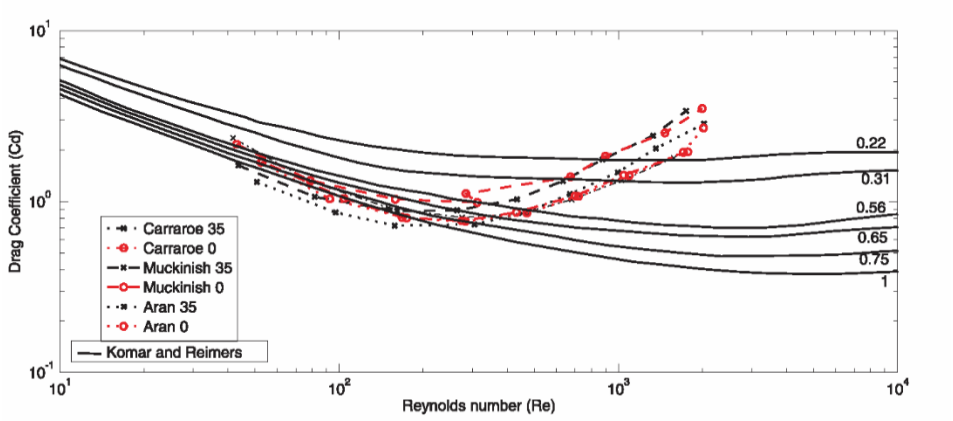

Figure 2.8: Drag coefficient versus grain Reynolds number for the three maerl samples at salinity 35, superimposed on drag-coefficient curves based on data from (Komar and Reimers, 1978) for settling-velocity experiments across a range of grain shapes. The latter represent parametric trends with different Corey shape factors between 0.22 and 1.0 where a value of 0.7 is typical for natural quartz grains.

If the reciprocal convexity increases linearly with sieve diameter (Figure 2.5), and C_2 increases linearly with sieve diameter (Figure 2.7), it suggests that C_2 is inversely proportional to convexity. There is a strong correlation between C_2, estimated assuming $C_2 = a/C$, and C_2 inferred from the settling-velocity inversions (Figure 2.9). The relationship is independent of salinity and the results indicate a gradient of $a \sim 1$.

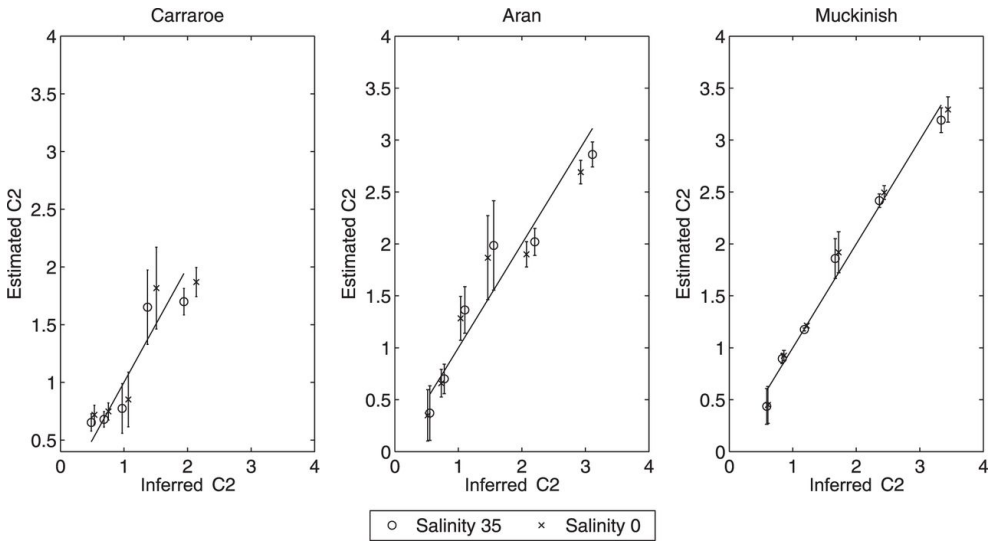

Figure 2.9: C_2 ($= aC^{-1}$) estimated from the grain-shape measurements of convexity versus C_2 inferred from the settling-velocity observations using this paper's modification of the Ferguson and Church (2004) model with $C_2 = C_{21}\, d$. The solid lines in the figure have a gradient of 1 to highlight the correlation between the estimated and inferred C_2. The actual gradients of the least-squares lines fitted between the two variables are 0.85 ± 0.15 ($r^2 = 0.7$), 0.91 ± 0.1 ($r^2 = 0.85$), and 0.98 ± 0.02 ($r^2 = 0.97$) for Carraroe, Aran, and Muckinish grains, respectively.

2.5. Discussion

For siliciclastic sediment, particle diameter, not shape, is treated as the controlling variable in settling-velocity experiments because particle-shape indices tend to be constant for a given siliciclastic sediment. In contrast, this study shows that grain-size-dependent shape, and particularly angularity, plays a central role in governing the settling velocity of maerl. The drag coefficient increases more rapidly with increasing diameter compared to the Ferguson and Church (2004) model as the grains become increasingly irregular. Van Der Meulen (1988) measured the settling velocity of coral sand and also found that it was more angular with a lower settling velocity than natural sub rounded quartz sands. This result is thought to be due primarily to the increase in projected area increasing the friction component of the drag force (Janke, 1966) and the lower density of the maerl grain. These laminated or coated grains contained voids that decreased the grain density due to the method of episodic growth (Peter Harris, *pers comm.*).

Ferguson and Church (2004) provide a simple and flexible model for settling-velocity data with two free parameters to account for size-invariant shape effects. The modification in this paper to their formulation also requires only two free parameters that can account for grain-shape metrics of maerl that vary with sieve diameter. This result highlights the need to measure grain shape across a range of diameters, especially for biogenic sediment. Furthermore, it has been demonstrated that (reciprocal) convexity is a robust parameterization of the particle shape, and it directly controls C_2, and therefore the drag coefficient, especially at Reynolds numbers greater than 220. For maerl, the boundary between the transitional region and the inertial region falls at lower Reynolds number of 220 compared to ~ 1000 for siliciclastic sediment of varying, but grain-size-invariant, shape factors.

In the intermediate regime, the shape factor α (Strom and Keyvani, 2011) representing particle shape in the Stokes regime, is contributing only to C_1, a parameter that varies weakly across the three different hydrodynamic regimes, suggesting that an ecological or physical parameter is influencing the shape factor. The most sheltered shore face zone (Muckinish) has $C_1 \sim 42 \pm 2$, whereas the unsheltered open marine (Aran) and beach swash

zone (Carraroe) have $C_1 \sim 36 \pm 4$. This may be due to an increasing degree of wave action at the latter two sites, which reduces the complexity of branching of the maerl; this trend is consistent with observations (Figure 2.7) that suggest that all grain-shape parameters, particularly convexity, decrease rapidly with diameter at Muckinish. This conclusion is tentative, and future work should focus on the relationships between settling velocities and maerl grain morphological parameters with sieve diameters from ~ 0.1 mm to 30 mm (corresponding to $0.1 < \mathrm{Re} < 10^5$), and their implications within the broader-scale physical environment.

In this study, the relationship between reciprocal convexity of a maerl grain's major cross section and C_2 is striking in its simplicity and effectiveness. Furthermore, the convexity metric is a less complicated descriptor of the shape of a biogenic, non-crystalline, branched grain, as opposed to the triaxial-ellipsoid-based metric, the Corey shape factor, and the qualitative Powers roughness metric (Dietrich, 1982). We therefore recommend that similar future studies measure the convexity of the end members and midpoint of the grain-diameter distribution.

The tendency of maerl to form in, or maintain, spatially well-defined open marine "beds" and beaches of poorly sorted maerl with small quantities of fine sand (De Grave and Whitaker, 1999) could be explained by our results. Suspension, and potentially advection, of sediment occurs when the local upward turbulent component of velocity exceeds the settling velocity. Because of the grain-size dependency of drag, for a large range (2 mm–10 mm) of maerl grain-size distributions, settling velocity (and suspension threshold) is effectively grain-size invariant (Figure 2.4). For an initial seafloor composed of unsorted sand and unsorted maerl, there may be processes whereby motion is initiated and water velocity exceeds ~ 210 mm s^{-1} so a large fraction of the maerl grain size distribution is brought into suspension with a disproportionately smaller amount of hydraulically equivalent siliciclastic sand-size grains. Such a process is more likely to occur for non-beach maerl sediment (e.g., Muckinish) that exhibits the greatest shape change with diameter (Figure 2.5) because it has been subjected to a low degree of abrasion. The beach maerl from Carraroe

exhibits a less pronounced change in grain shape with grain size, so the settling curve exhibits less grain-size invariance than those from the other two locations. This transport mechanism could partly explain the observed heterogeneity in sand and maerl coastal and littoral environments that are sheltered from storms that could mobilize coarse siliciclastic gravel. This winnowing mechanism could also explain homogeneity within the maerl deposits. We suggest that this hypothesis could be tested using computational fluid dynamics modelling.

3. Critical Bed Shear Stress of Maerl

This chapter is to be submitted as:

Joshi, S., Duffy, G.P., and Brown, C., Critical bed shear stress and threshold of motion of maerl biogenic gravel.

3.1. Abstract

A determination of the critical bed shear stress of maerl is a prerequisite for quantifying its mobility, rate of erosion and deposition in conservation management. The critical bed shear stress for incipient motion has been determined for the first time for samples from biogenic free-living maerl beds in three contrasting environments (open marine, intertidal and beach) in Galway Bay, west of Ireland. The bed shear stress was determined using three methods, Law of the Wall, Turbulent Kinetic Energy and Reynolds Stress, in both a rotating annular flume and a linear flume. The velocity profile of flowing water at different elevations above a bed of the natural maerl grains was measured in four runs of progressively increasing flow velocity until the flow exceeded the critical threshold shear stress of grains on the bed. The critical Shields parameter was then estimated as a non-dimensional mobility number and the results are compared with the Shields curve for natural quartz sand. The critical Shields parameters for the maerl particles from all three environments fall below this curve. Along with a previously reported correlation between maerl grain shape and settling velocity, these results suggest that the highly irregular shapes also allow maerl grains to be mobilised more easily than quartz grains with the same sieve diameter. The intertidal beds with the roughest particles exhibit the greatest critical shear stress because the particle thalli interlock and resist entrainment. In samples with a high percentage of maerl and low percentage of siliciclastic sand, the lower density, lower settling velocity and lower critical bed shear stress of maerl results in its preferential transport over the siliciclastic sediment. At velocities ~ 10 cm s^{-1} higher than the critical threshold velocity, rarely-documented subaqueous maerl dunes formed in the annular flume.

3.2. Introduction

3.2.1. Maerl

Maerl is free-living, non-geniculate, coralline red algae (rhodolith) that produce mobile biogenic sediment deposits in shallow marine environments. It is one of four main macrophyte-dominated benthic communities in the world (Foster, 2001). Maerl beds play a primary role in carbonate production in tropical southwest Atlantic and are a globally significant blue carbon sink (Amado-Filho et al., 2012). Maerl is of ecological significance and two species, *Lithothamnium corallioides* and *Phymatholithon calcareum*, are protected under Annex V of the EC Habitats Directive, with indirect protection under Annex I (EC Council Directive 92/43/EEC). Maerl beds are also included on the Oslo and Paris (OSPAR) Convention's List of Threatened and/or Declining Species and Habitats (Hall-Spencer et al., 2010). Their spatial distribution contributes to the evidence base for the Seabed Integrity Good Environmental Status descriptor in the Marine Strategy Framework Directive (EC Council Directive 2008/56/EC). In Ireland, gravel beaches and dunes of dead and live maerl receive protection and form a part of Special Areas of Conservation (SAC), as well as OSPAR Marine Protected Areas, and approximately two-thirds of them occur within SACs located in and around Galway Bay (De Grave and Whitaker, 1999). The ratio of live to dead maerl is a proxy for the quality of the shallow water benthic habitat (NPWS, 2013). Given its requirement for photosynthesis, maerl is restricted to the seafloor in the euphotic zone; its heterogeneous spatial distribution is a consequence of sensitivity to light intensity, spatial heterogeneity in current intensity, moderate wave action, low sedimentation rates and high salinity (Birkett et al., 1998). Maerl forms beds, banks, and subaqueous dunes ~ 0.3 m to 2 m high (e.g., Keegan (1974), Hall-Spencer (1995)) probably due to oscillatory wave-induced currents (Bosence, 1976). For siliciclastic sand and maerl gravel mixtures, the critical threshold velocity for incipient motion is a function of the maerl grain diameter (Harris et al., 1996) and maerl mobility variations can arise from differences in hydrodynamic processes in shallow wave-dominated maerl beds, deeper water wave-dominated beds and deeper water current-dominated beds (Marrack, 1999).

Fossil rhodoliths are also important indicators of the depositional environment and the hydraulic energy in shallow and deep deposits (Johnson et al., 2012; Quaranta et al., 2012). For example, the rapid burial of rhodolith sediment following a high-energy storm event often leads to dissolution, where carbonate has dissolved below the carbonate saturation horizon (Johnson et al., 2012). The preferential transport of rhodolith in sand-rhodolith mixtures is likely to have implications for the Late Pleistocene transgressive carbonate sedimentation of rhodolith beds on the Abrolhos Shelf during periods of sea-level rise (D'agostini et al., 2015). There is clear evidence of a strong relationship between the available hydraulic energy, maerl grain morphology and sediment mobility (Riosmena-Rodríguez et al., 2011; Nelson et al., 2012) so an understanding of maerl hydrodynamic properties is also important for re-constructing palaeo-environmental processes and quantifying the range of present ecological niches of maerl (Bassi et al., 2012).

Two hydrodynamic properties of importance for the understanding of maerl deposition are the settling velocity and the critical bed shear stress. The particle settling velocity influences the rates of vertical flux, entrainment, deposition, and sorting of particles suspended in, and deposited by, a fluid (Fredsøe and Deigaard, 1992). The branched forms of maerl particles, with grain size-dependent roughness, experience significantly greater drag than are predicted for natural quartz grains with the same intermediate diameter (Joshi et al., 2014). The critical bed shear stress is a prerequisite for quantifying the incipient motion, mobility, rate of erosion and spatial deposition of maerl in the presence of benthic currents. Just as the distinctive maerl grain morphology significantly influences the particle settling velocity (Joshi et al., 2014), it is also likely to influence the critical bed shear stress. Therefore this paper reports the first results of a laboratory determination of the critical bed shear stress for incipient motion in steady unidirectional currents of maerl particles sampled from three coastal locations with different hydrodynamic environments.

3.2.2. General Theory

Critical bed shear stress at the threshold of particle motion is defined as the tangential frictional resisting force per unit area that the flow encounters on the seafloor, primarily as a result of the composition and roughness of the bed material (Masselink et al., 2011). As part of the first mode of bedload transport, the threshold of sediment movement is a critical stage of entrainment of sediment (Buffington, 1999; Paphitis, 2001; Dean and Dalrymple, 2002). Wiberg and Smith (1987) derive the critical bed shear stress for uniform and heterogeneous beds in terms of the gravitational force based on the immersive weight, drag and lift coefficients, downstream velocity, the force resisting downstream motion and angle of repose (the difficulty of removing a grain from its grain pocket). Particle motion occurs when the instantaneous fluid force on a particle exceeds the instantaneous resisting force due to the submerged weight and bed friction (van Rijn, 2007a). A grain moves from equilibrium into the first stage of entrainment when the lift, drag and viscous forces across its surface area overcome the stabilising force of its weight and factors that relate to the position of the grain relative to adjacent grains. The stochastic process gives rise to a threshold of motion envelope (Buffington and Montgomery, 1997).

Grain shape has a significant effect on the critical bed shear stress for initiation of motion in the case of non-uniform graded beds such as maerl. Previous studies have shown that the relative exposure of the grain introduces two length scales; the grain diameter and the grain roughness length (Miller and Byrne, 1966; Wiberg and Smith, 1987; van Rijn, 2007c). The ratio between these two length scales alters the angle of repose of sediment, in turn altering the critical bed shear stress (Miller and Byrne, 1966; Wiberg and Smith, 1987). The effect of the relative exposure of the grain shape on the initiation of motion is known as the relative grain protrusion (Fenton and Abbott, 1977). The more exposed the grain is, the higher the relative grain protrusion, the lower the critical bed shear stress for initiation of motion. The relative grain protrusion also plays an important role in governing hiding and exposure processes, where large grains armour around smaller grains (Egiazaroff, 1965; Day, 1980; van Rijn, 2007c).

3.3. Materials and Methods

3.3.1. Introduction to Experiment

In this study, the critical bed shear stress has been estimated from laboratory experiments on maerl samples from three different sedimentary environments (beach, intertidal and open marine) in Galway Bay, west of Ireland. The locations of the Carraroe biogenic gravel beach, the Aran open marine beds, and the Muckinish intertidal beds are given in Joshi et al. (2014). The Carraroe samples were obtained from surficial sediment from the swash zone adjacent to a berm. The maerl beach is subjected to summer mean significant wave heights < 0.6 m (as obtained in summer 2007 wave model in Chapter 4.). The Aran Islands bed was sampled at a water depth of 26 m and is subject to storm wave action, with wave-driven sorting of disaggregated bivalves and shell hash occurring in nearby rippled scour depressions. The Muckinish inter-tidal beds are sheltered, with significant wave heights < 0.3 m during the strongest summer storm. The principal species in Carraroe and Aran is *Phymatolithon calcareum,* and in Muckinish it is *Lithothamnium corallioides* and rarer species (Maggs, 1983).

The Aran bed is poorly sorted, whereas the Carraroe and Muckinish beds are moderately well sorted. Each sediment sample is a heterogeneous mixture and, as the grain size distribution, grain angularity, roundness and sorting influence the angle of repose (Miller and Byrne, 1966) and therefore critical bed shear stress. Grain size has been measured using the methodology stated in Mason (2011). The natural sediment was dried in an oven at 60ºC for 48 hours and separated into 0.5 phi fractions using a Retsch sieve shaker from 1 mm to 32 mm. Details of the grain shapes of the samples from the three locations are given in (Joshi et al., 2014) and a summary of grain size statistics is presented in Appendix 1 (Section 6.1).

The critical bed shear stress for the maerl samples is estimated in the laboratory using three techniques: Law of the Wall (LotW), Turbulent Kinetic Energy (TKE) and Reynolds Stress (RS).

3.3.2. Law of the Wall

The LotW technique requires measurement of the velocity profile using multi-level measurements. The theoretical profile has a logarithmic structure due to the increasing effect of bottom friction with proximity to the sediment–water interface, described by the von Kármán–Prandtl equation (Soulsby, 1997):

$$u(z) = \frac{u_*}{\kappa} \ln\left(\frac{z}{z_o}\right) \tag{3.1}$$

where κ is the von Kármán constant, $u(z)$ is the current speed profile, z is the elevation above the bed, u_* is the shear velocity and z_o is the roughness length. The equation can be rearranged in the form of $y = mx + c$ where the gradient of the logarithmic layer, m is proportional to the bed shear velocity (Masselink et al., 2011). In practice, the shear velocity is:

$$u_* = m\kappa \tag{3.2}$$

where $\kappa = 0.409$.

The relationship between bed shear stress τ_0, fluid density ρ, and shear velocity is:

$$\tau_0 = \rho {u_*}^2 \tag{3.3}$$

The LotW technique requires steady, unidirectional flow and can be sensitive to accelerating flow, and it requires accurate measurement of the elevation above the bed (Wilcock, 1996; Biron et al., 1998). Critical bed shear stress and critical shear velocity error estimates are calculated using Equation 3.4 below (Wilkinson, 1983) for formal error propagation with respect to the bed shear stress, including a minor simplification for elevation errors:

$$\delta m = \frac{t}{\sqrt{(N-2)}} \frac{\sigma_y}{\sigma_x} \sqrt{(1-r^2)} \tag{3.4a}$$

$$\delta u_* = \kappa \delta m \tag{3.4b}$$

$$\delta \tau = 2 u_* \rho \kappa \delta m \tag{3.4c}$$

where δm is the error in the gradient, σ_x is the standard deviation of the natural logarithm of the elevation in m, σ_y the standard deviation of the velocities in m s^{-1}, r is the coefficient of determination, and N is the number of data points.

Keulegan (1938) determined the characteristics of turbulence for open channel flow following the method used by Nikuradse (1932) for turbulence and surface flow characteristics in pipes of varying roughness. The length δ, defined as the thickness of the viscous sublayer, is the minimum distance from the wall for which the LotW equation holds. Unlike the turbulent log-layer, it is a region of laminar flow where viscous stresses predominate or are of the same order as the apparent stresses due to momentum exchange. The viscous sublayer thickness is proportional to the kinematic viscosity ν, divided by the shear velocity:

$$\delta = 11.5 \frac{\nu}{u_*} \tag{3.5}$$

Keulegan (1938) obtained approximations for the velocity distribution in the presence of smooth, wavy and rough walls, and defines a relative waviness ratio to differentiate between a wavy wall and a rough wall (and an intermediate region). The viscous sub-layer is significantly thinner or absent over a rough wall (i.e., equivalent to a rough bed) than that over a smooth wall due to the roughness of the grains protruding into the flow. As the ratio between the thickness of the viscous sublayer and the median grain diameter δ/d_{50} approaches zero with increasing grain Reynolds number (Paphitis, 2001), we assume that the viscous sublayer in our experiments is negligibly thin due to highly convex grain protrusions of coarse maerl into the fluid.

3.3.3. Turbulent Kinetic Energy

Turbulence is a major contributor to bed-load erosion and the TKE is directly related to the threshold of motion (Bowden and Fairbairn, 1956; Redjah et al., 2010). The TKE technique is based on the assumption that bed shear stress is proportional to turbulent velocity fluctuations so the root mean square (rms) error in velocity can be considered to be the magnitude

of the turbulence. The TKE (Bowden and Fairbairn, 1956; Pope et al., 2006; Redjah et al., 2010) is:

$$TKE = \frac{1}{2}\left(\overline{u'^2} + \overline{v'^2} + \overline{w'^2}\right) \quad (3.6a)$$

$$\tau_{TKE} = c\rho\, TKE \quad (3.6b)$$

where u', v' and w' are the instantaneous velocity fluctuations around the mean flow in the x, y and z (positive upwards) directions respectively, the bar denotes time averaging, τ_{TKE} is bed shear stress, c ~ 0.19 (Soulsby, 1983; Thompson et al., 2003; Lefebvre, 2009) and $\rho = 1000$ kg m^{-3} is the water density. The theoretical profile of the TKE increases significantly towards the bed as the turbulence is a maximum near the bed (Soulsby, 1983; Nicholas, 2001).

Turbulence Intensity (TI) is a percentage of the absolute value of the turbulence fluctuation $rms\,(U')$ with respect to the absolute value of the mean resultant velocity, $\overline{U}$ (Dyer, 1986; Lefebvre, 2009). Dyer (1986) found the near-boundary TI to be ~ 10% locally. TI quantifies the profile of the turbulence characteristics above the maerl bed by comparing the local level measurements with the turbulence characteristics across the entire profile. We include it in the analysis as it is useful for identifying local-level turbulence cells within the TKE shear stress profile and signal contamination:

$$TI = 100\frac{rms\,(U')}{\overline{U}} \quad (3.7)$$

3.3.4. Reynolds Stress

The RS quantifies the rate of turbulent transfer of momentum across the (x, y, z) planes (Soulsby, 1983; Jamieson et al., 2010). The one-dimensional principal RS component, τ_{RSxz} is defined from local velocity fluctuations, u', w' in the streamwise x- and vertical z-directions respectively:

$$\tau_{RSxz} = -\rho\overline{(u'w')} \quad (3.8a)$$

where the bar denotes time-averaging. The other components are:

$$\tau_{RSxy} = -\rho\overline{(u'v')} \quad (3.8b)$$

$$\tau_{RSyz} = -\rho\overline{(v'w')} \quad (3.8c)$$

The one-dimensional principal RS (*x-z)* component is sensitive to elevation (Kim et al., 2000; Thompson et al., 2003; Biron et al., 2004; Pope et al., 2006). In this study, three components of the RS have been measured to account for the momentum transfer across all three planes.

3.3.5. Critical Shields Parameter

The critical Shields parameter (θ_c) quantifies the mobility of maerl beds when subjected to pure current fluid flow. The original equation (Shields, 1936) is:

$$\theta_c = \frac{\tau_c}{g(\rho_s - \rho)d_{50}} \quad (3.9)$$

where g is the acceleration due to gravity, d_{50} is the median grain size in the experimental sample distribution, τ_c is the critical bed shear stress and ρ_s is the density of the sediment particle. The dimensionless Shields parameter, typically 0.03 to 0.1, is the ratio of the shear forces acting on the particle compared to the submerged weight of the particle. The Shields curve compares the ratio of the bed shear stress and gravity force to the ratio between the inertia and viscous forces at threshold conditions (Varoni, 1964; Thompson et al., 2004). The curve represents the point when 1 - 10% of the sediment is in motion (rolling, sliding or colliding) (Sutherland and Soulsby, 2011). In the experiment (described below), the time series of the three-dimensional current variation measured at 0.1 of the flow depth is used to calculate the critical bed shear stress and, in turn, the Shields parameter in the TKE and RS techniques.

Buffington and Montgomery (1997) identified systematic biases accounting for the scatter in the original Shields curve. Paphitis (2001) modified the Shields curve, based on data for quartz densities, with a stochastic envelope

defined as containing 91.5% of selected data. Rather than picking one particular value for the critical bed shear stress for a sediment sample, our experiment provides a threshold envelope using the standard deviation of the three replicates of the Shields parameter. The grain shape and inter-granular geometry can affect the degree of grain protrusion into the viscous sublayer and this can alter the critical Shields parameter (Buffington and Montgomery, 1997; Paphitis, 2001). A variable ratio between the grain diameter and the thickness of the viscous sub-layer in the presence of protrusions can lead to increased vertical bursting events responsible for bedload transport (Heathershaw and Thorne, 1985).

3.3.6. Experiment

The Cees-Kranenburg rotating annular flume in Delft University of Technology (Figure 3.1) was used for the experiments with the Carraroe and Muckinish samples, and a linear flume was used for the Aran sample because the quantity of material was insufficient for use in the annular flume. Care was taken to minimise the impact of vertical sorting and gradation in the flume environment. Sediments were added to the dry flume and the bed was levelled using a levelling tool specifically constructed for this purpose. Bed aging, where the bed is allowed to settle following resuspension of the material, was not carried out to avoid the effect of differential settling and the consequent non-natural vertical gradation. In each flume, for four runs with samples from each location, the flow velocity was progressively increased beyond the threshold velocity that initiated motion of grains from the bed, so allowing the estimation of critical bed shear stress using the three techniques.

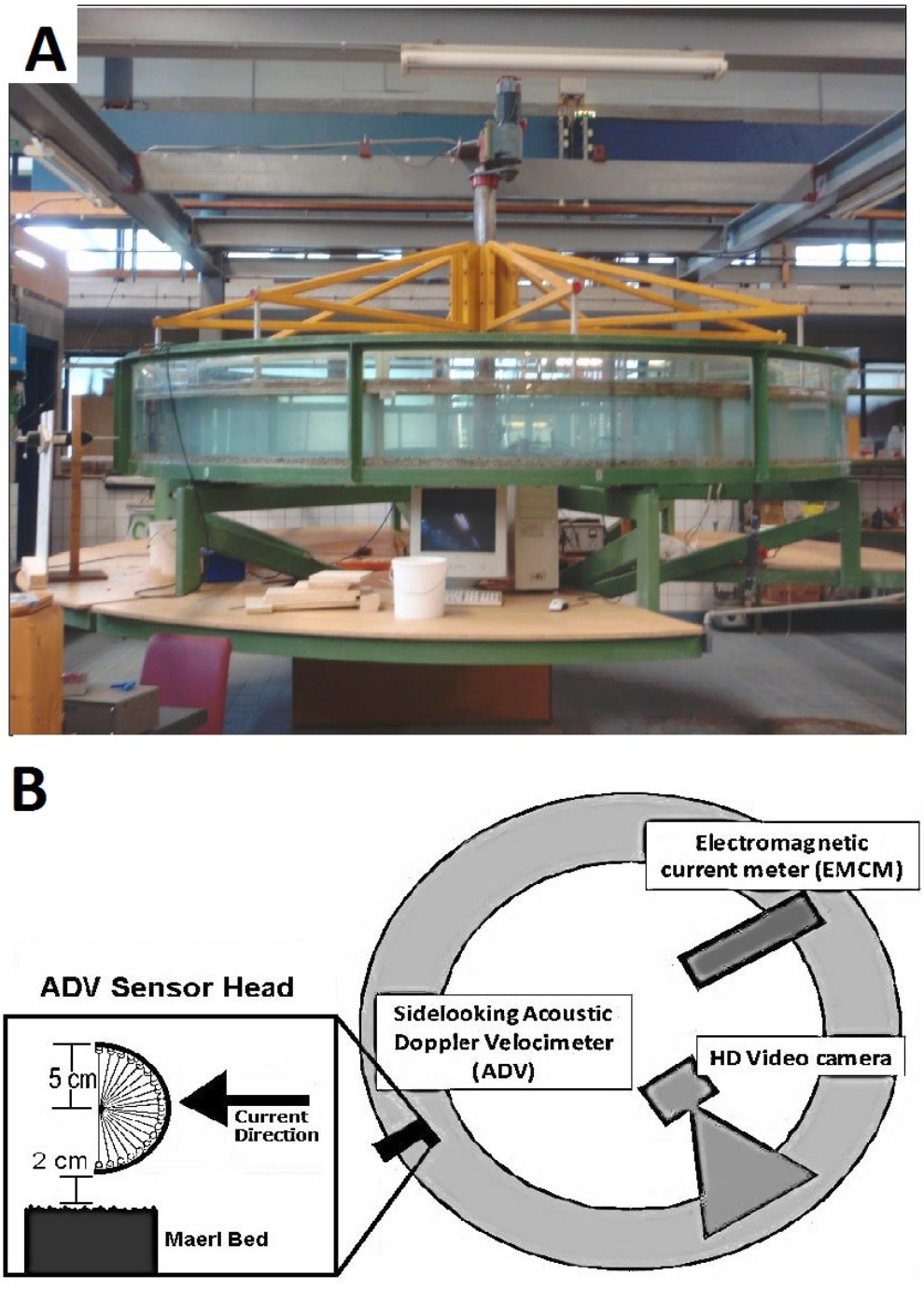

Figure 3.1: A) The TU Delft rotating annular flume. B) A plan view of the rotating annular flume, with the side-looking Acoustic Doppler Velocimeter (ADV), Electromagnetic Liquid Meter and HD video camera. The ADV is mounted at 7 cm above the bed.

Rotating Annular Flume

The advantage of annular flumes for maerl experiments is that there are none of the entrance and exit boundary effects associated with linear flumes (Booij, 1994). The TU Delft flume has an external diameter of 3.7 m, with a rectangular annular cross section of 0.3 m (width) by 0.47 m (maximum adjustable height) (Winterwerp and Kranenburg, 2002). The lid and the flume base rotate in opposite directions simultaneously in order to generate uniform unidirectional velocity flow and minimise secondary flows associated with curvature. Figure 3.2A illustrates the effect of the secondary circulation, particularly at elevations ~ 5cm, on profiles which were located near the bottom right. Lid (ω_l) and flume base (ω_b) rotation speeds are also shown in Figure 3.2B. A two-cell secondary flow model (Sheng, 1989) of the generalised rotating annular flume is shown in Figure 3.2E. By using an integrated boundary layer model, Sheng (1989) identified that radial velocities within the boundary layer were about 20% of the mean tangential velocities, but this strongly depends on annular flume configurations (Yang et al., 2000). Booij (1994) presents the simplified Reynolds equations and the continuity equation solved for a cylindrical coordinate system (Figure 3.2B). Booij (1994) identified the optimum ratio between the flume rotation speed and the lid rotation speed (in the opposite direction) to 1) minimise the intensity of the secondary flows (especially in the near-bed part of the flume) and to produce a uniform distribution of tangential velocity and of near bottom shear stress over the flume width. A flow depth of 0.256 m was used, resulting in a ratio of -2 which was maintained in all four velocity runs. The depth-averaged velocity (Soulsby, 1997) allowed the calculation of the flow Reynolds number (Table 3.1).

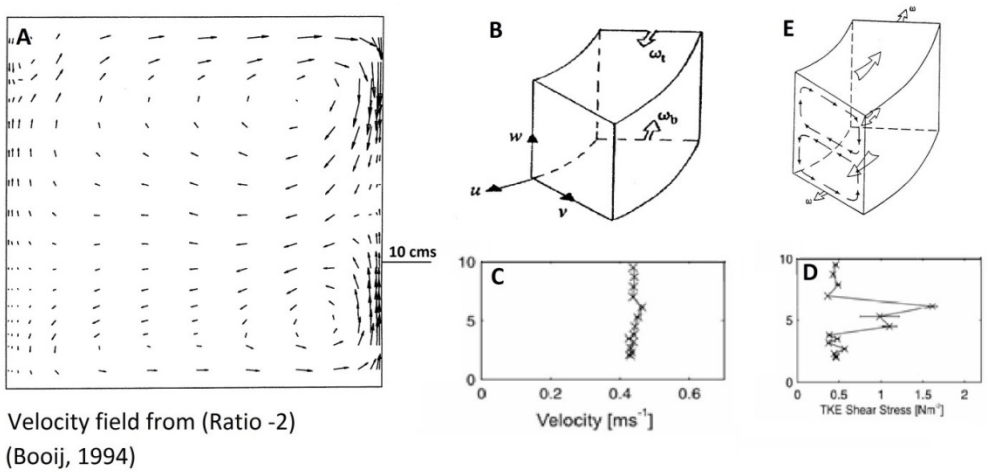

Figure 3.2: A) Cross-section of velocity field in the rotating annular flume with the same ratio between the lid and flume rotation speeds used in this experiment (Booij, 1994) B) The coordinate system (Booij, 1994) showing tangential (u), radial (v) and vertical (w) components to which all measured velocities were transformed. C) Measured velocity profile at 45 cm s^{-1} for run 3 of the Carraroe samples. D) TKE shear stress profile at 45 cm s^{-1} for the Carraroe sample. E) The two-cell secondary flow model (Sheng, 1989) for the generalised rotating annular flume.

Table 3.1: Flow Reynolds Number (Re), depth-averaged speed, u (cm s^{-1}), and flume base and lid rotation speeds (s^{-1}) for each run. The Re is calculated from uR/v where R is the hydraulic radius, v is the kinematic viscosity (1.004 x 10^{-6} m^2 s^{-1}) for a water temperature of 21ºC. The hydraulic radius was 28 cm for the rotating annular flume and 25 cm for the linear flume.

Run		**Carraroe**		**Aran**		**Muckinish**	
	Flow speed	**Rotation Speed**	**Re**	**Flow speed**	**Re**	**Rotation Speed**	**Re**
1	25.23 ± 0.2	Flume -0.320 Lid 0.667	70583	27.55 ± 0.3	68599	Flume -0.320 Lid 0.667	66945
2	36.37 ± 0.2	Flume -0.466 Lid 0.969	101743	35.65 ± 0.2	88759	Flume -0.466 Lid 0.969	97785
3	43.39 ± 0.5	Flume -0.550 Lid 0.140	121380	46.91 ± 0.8	116815	Flume -0.550 Lid 0.140	112304
4	51.86 ± 0.5 threshold velocity	Flume -0.650 Lid 1.352	145078	56.06 ± 0.5	139598	Flume -0.810 Lid 1.680	159885

The bottom of the flume was covered with a 3.5-cm thick layer of maerl. Fresh water at a constant temperature of 21°C was used and the room temperature was regulated. A Panasonic HDC HS300 video camera was mounted on a tripod to quantify the stages of sediment movement. A stop watch was visible in the field of view and a black cloth enhanced the visibility of the maerl in the footage. Small quantities of china clay particles were added to increase the density of scattering points and signal-to-noise ratio of the acoustic return signal.

A Nortek Vectrino side-looking ADV utilises the Doppler shift of sound from four beams to measure the three components of instantaneous velocity of the particle at a point. It was mounted 7 cm above bed level near the middle of the flume, and had a distance to sampling volume of 5 cm, sampling rate of 25 Hz, and a cylindrical sampling volume of length 0.91 cm. The velocity was measured three times at each elevation for each

velocity run for each sample and these provide estimates of precision. Each of these triplicate measurements was logged for one minute bursts with ten seconds at the beginning and end of the three minute period to allow the ADV to reach equilibrium, when the ADV correlation statistics become stable after adjusting to the properties of the water. This is sufficient to capture the turbulence properties (Biron et al., 2004).

A Delft Hydraulics Four Quadrant analogue electromagnetic liquid meter (EMS) utilises Faraday's Law of Induction to measure the velocity of a conductive liquid moving through a magnetic field. Its ellipsoidal sensor obtains a cylindrical sampling volume of 0.33 cm diameter by 0.5 cm height (De Wit, 1992), and it was mounted 180° to the ADV to corroborate the ADV results. Once the flume flow was constant, the side-looking ADV was rotated while facing the direction of the flow, allowing the flow to be measured in 10° increments, with additional measurements at 45° and 135°, to give a total of 21 points that comprised the velocity profile. The ADV digital data, EMS analogue data, and flume and lid rotation speed data were streamed into DASY Lab data acquisition software. An average difference of 1.2% was found between the EMS and the ADV data at the same elevation, therefore the EMS data are not presented. The logarithmic layer was identified from the velocity profiles using points at 2, 2.1, 2.3, 2.67, 3.2 and 3.5 cm elevation (corresponding to the 10° rotational increments) in the bottom 15% of the water column.

Linear Flume

A 4.3 m (length) x 25 cm (width) x 30 cm (height) linear flume was utilised for the Aran open marine sample. An ADV and video was used as in the rotating annular flume. A Nortek Vectrino Lab downward-facing ADV, situated in the centre of the linear flume, profiled the water column from bed level +0.5 cm to +9.5 cm with a total of 19 points. The bottom of the flume was covered with a 6.5-cm thick layer of maerl. The logarithmic layer was identified from the velocity profiles at 0.5 cm intervals from 2.5 to 5.5cm elevation in the bottom 22% of the water column.

Choice of Elevation

The determination of zero level was made by assuming the actual bed thickness was within ±0.1, ± 0.25, ± 0.5, ± 1 and ± 2 cm of measured bed thickness and then obtaining the best fitting regression with a theoretical LotW profile. For the annular flume, the r^2 values (~0.99) did not change significantly, suggesting the zero level datum surfaces were appropriately determined. For the linear flume, the zero level datum was determined to be - 2 cm below the initial bed elevation, corresponding to an improvement of r^2 from 0.86 to 0.92. This is a plausible value because the large grain protrusions in the Aran sample considerably distorted the zero level. All elevations for the Aran samples are referred to the level after this zero level determination. We note that this is also important for the TKE and RS techniques where the measurements must be located in the logarithmic layer (Kim et al., 2000; Pope et al., 2006).

Following Biron et al. (2004), we used an elevation of 0.1 of the flow depth, corresponding to 2.67 cm above the zero level for the rotating annular flume and 2.5 cm for the linear flume, to obtain the critical bed shear stress estimates for TKE and three-dimensional RS. The choice plays an important role in assessing errors in the critical Shields parameter (Section 6.1). The lowest measurements in the velocity profile were at 2 cm and 2.5 cm in the annular and linear flumes, respectively. Even though these are below the 0.1 flow depth criterion, the data points provide useful information about the boundary layer.

Threshold of motion

The critical threshold velocity was determined by increasing the flow velocity until the point of incipient motion, defined as the medium stage (Buffington, 1999) where 'grains of medium diameter are in motion… not strong enough to affect bed configuration', was identified (Table 3.2). This is following on from Kramer (1935) definition of the four stages of incipient motion and is an attempt to standardise the identification of the threshold of motion based on visual observations. To consider the stochastic process, video observations were reviewed prior to making the ADV measurements to ensure that the same stage of motion was identified for all three samples.

Table 3.2: The stages of motion for each of the four velocity runs.

Velocity Run	Carraroe beach sediment	Aran open marine beds	Muckinish intertidal beds
1	No motion		
2			
3	Occasional saltating grain	No motion of maerl grains	Gentle vibration of some grains
Critical threshold velocity	Surficial grains of all grain sizes present in motion Maximum saltation path length of ~5 cm Little suspension of particles	Armouring of fine material within matrix of maerl gravels Small maerl gravels mobile Maximum saltation path length ~4 cm Some suspension of particles	Saltation and tumbling of free maerl grains Some interlocking of grains resisting motion Maximum saltation path length ~3 cm Vibration of grains not in motion
Post-critical threshold velocity	Extensive formation of subaqueous dunes Continuous saltation, with onset of some suspension Rolling and tumbling of all grain sizes Erosion of bed level, ADV velocity profile not possible	Saltation of largest grains Extensive suspension of fine sediment Erosion and washing away of sediment, ADV profile not possible Greatest erosion in channel centre Subaqueous dunes not formed due to flume configuration Rippling of finer shell material	Extensive formation of subaqueous dunes Subaqueous dunes form towards the outer wall of the flume Some influence of secondary flows due to centrifugal forces Suspension of finest particles lead to clouding in video Erosion of bed level so ADV velocity profile not possible

3.3.7. Data Processing

The ADV data from both flumes were processed using WinADV software (Wahl, 2000). A signal to noise ratio filter and a phase-space threshold de-spiking filter were applied (Goring and Nikora, 2002) to average across spikes in the ADV time series data set; datasets with less than 95% of good data were rejected, e.g., if it was apparent there was interference near the moving lid. For the annular flume data, a rotational correction was applied to ensure the accuracy of the vertical separation of measurements. The average velocity and an estimate of precision were obtained from the three readings at each point.

3.4. Results and Analysis

3.4.1. Velocity Profiles

The sequence of velocity profiles (Figure 3.3) shows the progression to increasingly turbulent flow. Based on visual inspection of the gradient of the profile, the logarithmic layer extends from ~ 2 cm to 3.5 cm in the annular flume, and ~ 2.5 cm to 5.5 cm in the linear flume. The lines defining the logarithmic layer (Figure 3.4) have goodness-of-fit values > 0.92. Some superimposition with the secondary flow field is visible in the outer layer of the velocity profiles for the threshold velocity (Figures. 3.2A, C, D). As turbulence increases, so does the momentum transfer from layer to layer, resulting in increased eddy formation and entrainment into suspension (Chadwick et al., 2013). This progressive entrainment of the maerl grains in the velocity runs is crucial to determining the medium stage of the threshold of motion (Buffington, 1999). These stages (Table 3.2) include the formation of sub-aqueous maerl dunes at velocities >10 cm s^{-1} greater than the threshold velocity.

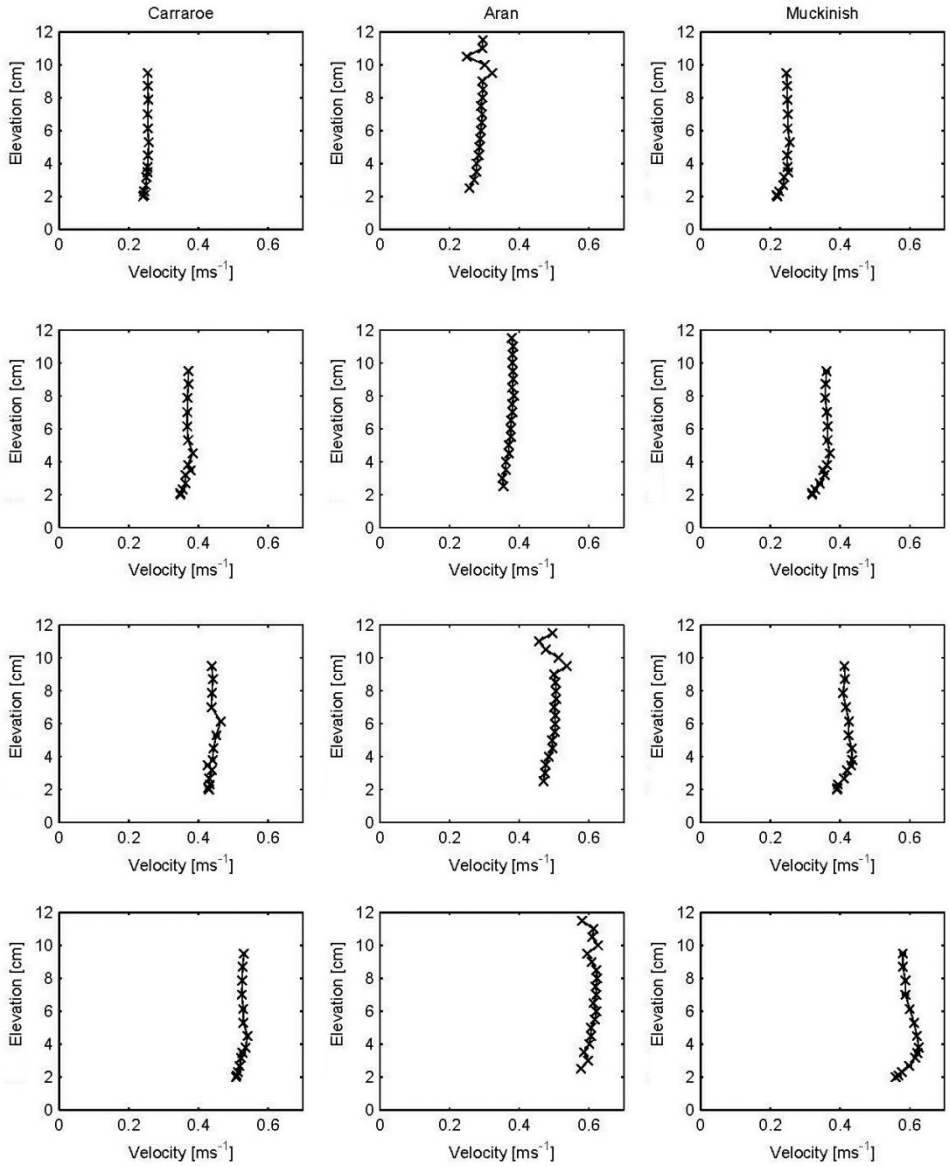

Figure 3.3: Velocity profiles for samples from Carraroe (beach), Muckinish (intertidal) and Aran (open marine). The rows correspond, from the top, to runs 1, 2 and 3 and the bottom row corresponds to the run at critical threshold velocity. The Aran curves show some interference effects in the flow field at elevations > 10 cm due to the top boundary of the linear flume.

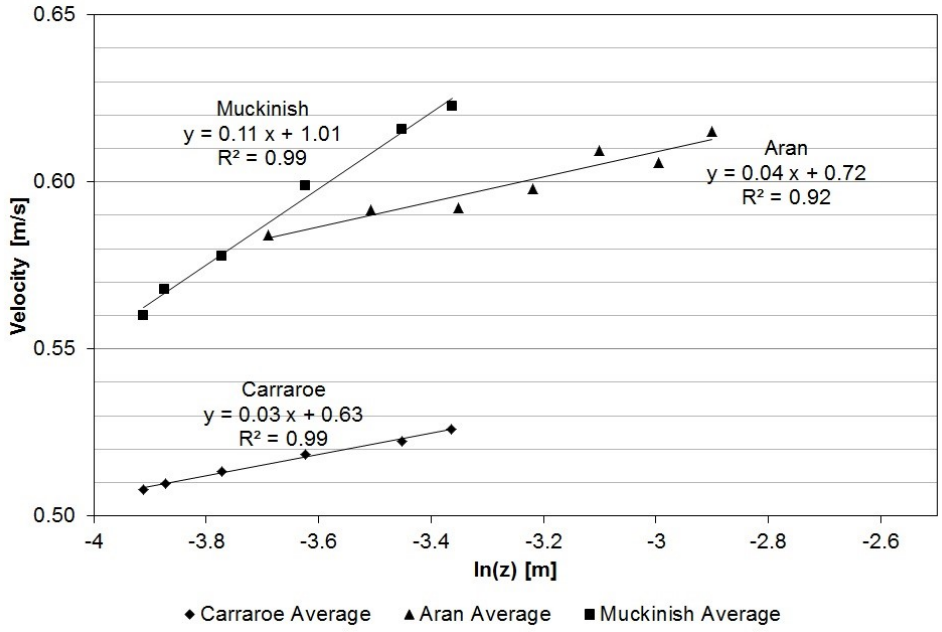

Figure 3.4: The velocity profile in the logarithmic layer as a function of elevation, z (m) in semi-log space for LOTW estimation at initiation of motion.

3.4.2. Turbulence Characteristics

Figure 3.5 shows the TKE shear stress is greatest nearest to the bed (apart from an outlier due to the top boundary in the linear flume) suggesting retardation in velocity relative to a parallel stationary boundary, in accordance with the "no slip" condition of boundary layer dynamics (Komar, 1974). This retardation is probably due to heterogeneities in the roughness (Soulsby, 1983; Wiberg and Smith, 1987), and is most pronounced in the Muckinish samples with the roughest grains. Some outliers can be identified outside the logarithmic layer at 4.5 cm and 6 cm for the annular flume velocity runs (Figure 3.5). The TI increases smoothly to a maximum near the bed (Figure 3.6) with values of ~ 15%, 10% and 8% for Muckinish, Carraroe and Aran samples, respectively. These values compare favourably with results from Dyer (1986), which include maximum TI values of ~ 10% for sand, with a lower roughness length than the Muckinish biogenic maerl sediment. The results confirm that TI is sensitive to the roughness of the grains.

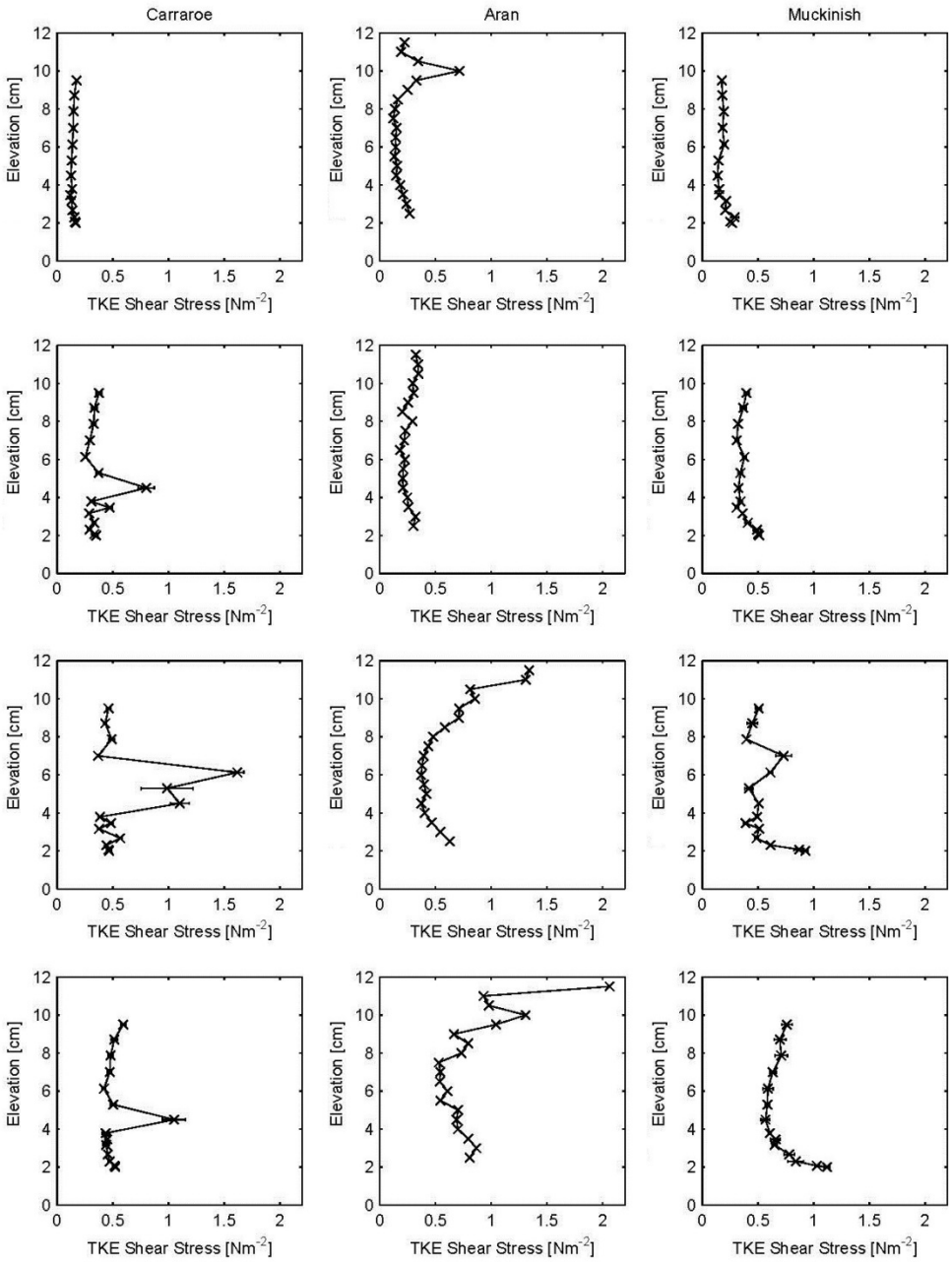

Figure 3.5: The profiles of the bed shear stress derived using the TKE method for the 4 velocity runs. For Carraroe, secondary flow interference is apparent at elevations ~ 4 – 6 cm; for Aran, at elevation > 8 cm due to the top boundary of the linear flume; for Muckinish curve (run 3), an eddy effect is apparent at ~ 7 cm. The Muckinish curve at the critical threshold velocity has the steepest increase in shear stress near the bed because of the high grain roughness.

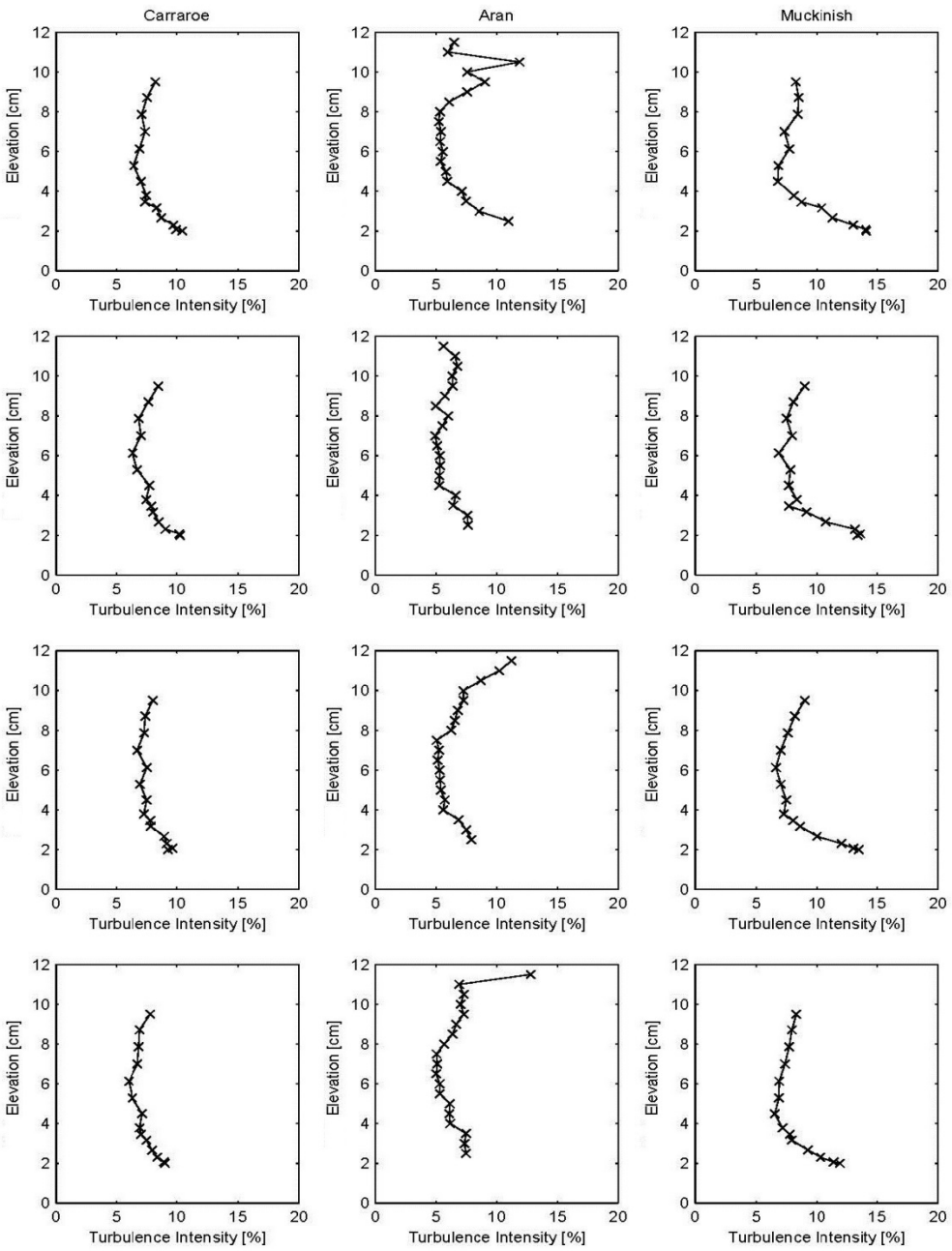

Figure 3.6: The profiles of TI for the 4 velocity runs. The Aran curves show some interference effects at elevations > 10 cm.

The principal RS (Figure 3.7) is positive for the Carraroe and Muckinish samples in the annular flume, and negative for Aran in the linear flume. In addition, the $-\rho(u'v')$ component, representing the momentum transfer in the stream-wise and lateral direction shows a significant negative stress near the bed, especially for the angular Muckinish samples, suggesting that it is related to the maerl grain roughness. The correlation between $-\rho(u'w')$ and $-\rho(u'v')$ components in Muckinish and Carraroe is possibly due to the curvature of the annular flume.

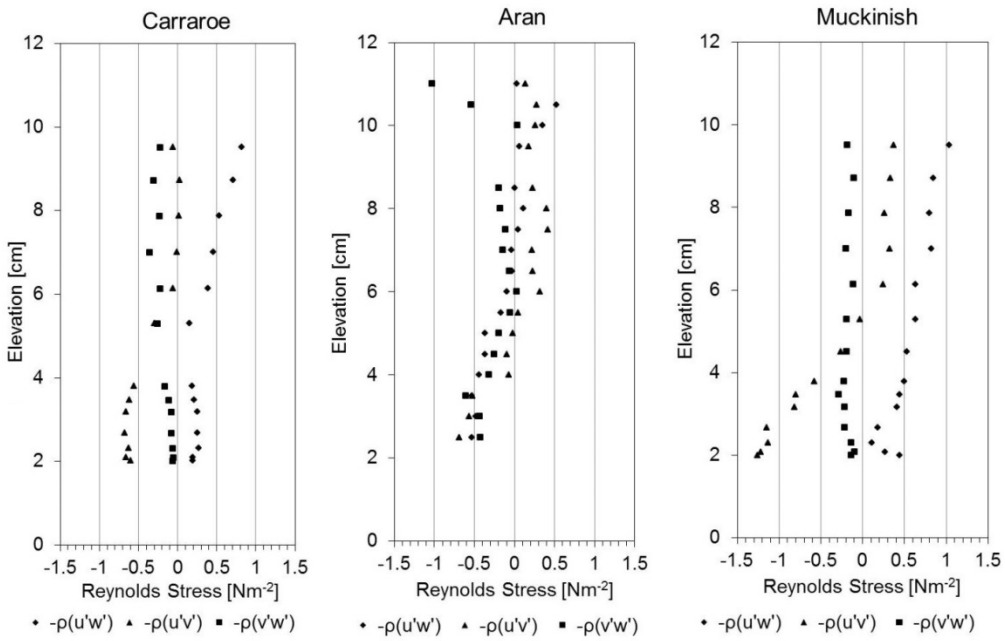

Figure 3.7: The profiles of the three-dimensional RS as a function of elevation above bed level at the critical threshold velocity. An outlier associated with the secondary flow cell at elevation 4.5 cm for the Carraroe run is omitted. Note that the principal RS component, $-\rho(u'w')$ is wholly negative for the Aran sample associated with exit flow conditions in the linear flume so these data have been omitted from the assessments.

Quadrant analysis (Heathershaw and Thorne, 1985; Keylock et al., 2012) is useful for determining the dominant turbulent processes based on measurements at threshold conditions at the 0.1 flow depth elevation (Section 6.1). 'Turbulent sweeps' with downward and forward fluctuations (negative w', positive u') result in bed-load transport, while 'outward interactions' suggest either large longitudinal fluctuations oriented upwards, or small u' fluctuations oriented towards the bed. The Carraroe and Muckinish data indicate turbulent sweeps as a (weakly) dominant process (27%); the Aran data indicate outward interactions (32%). The Muckinish and Carraroe threshold conditions therefore conform to theory. Biron et al. (2004) suggest that RS negative values are difficult to interpret if the flow field is too complex. Our one-dimensional principal RS profiles are negative in the complex flow field generated by the exit conditions in the linear flume, so we do not attempt to obtain the Shields parameter via the RS for Aran samples.

3.4.3. Critical Bed Shear Stress and Shields Parameters

We derived critical bed shear stress, derived quantities and error estimates for the samples (Table 3.3). TKE critical shear velocity is similar for Aran and Muckinish samples but the larger Aran grain size results in calculation of a lower critical Shields parameter (Eq. 3.9). Carraroe beach sediment is subjected to wave action so these samples are rounded and mobile, resulting in the lowest critical bed shear stress; the Muckinish sediment has the highest critical bed shear stress. The accuracies of the RS and LotW measurements are consistent with previously reported results by other workers (e.g., Wilcock (1996)). The precision errors for TKE critical bed shear stress are smaller than those reported by Biron et al. (2004). The Carraroe and Muckinish LotW measurements from the annular flume are more reliable than the Aran measurements from the linear flume. A fuller description of the error analysis is presented in Section 6.1.

Table 3.3: Parameters derived from the flume experiments, including the precision at one standard deviation.

	Method	Carraroe beach	Aran open marine	Muckinish intertidal
Median grain size (cm)		0.25 ± 0.05 Moderately well sorted	0.68 ± 0.10 Poorly sorted	0.45 ± 0.05 Moderately well sorted
Grain density (kg m^{-3})		2629 ± 16	2588 ± 16	2437 ± 14
Depth-averaged critical threshold velocity (cm s^{-1})		51.9 ± 0.5	56.1 ± 0.6	57.2 ± 0.4
Critical bed shear stress (N m^{-2}), τ_c	*LotW*	0.16 ± 0.06	0.22±0.07	2.07 ± 0.19
	Accuracy	± 0.03 (20%)	±0.15 (68%)	±0.52 (25%)
	TKE	0.46 ± 0.01	0.75 ± 0.04	0.78 ± 0.05
	RS	0.25 ± 0.05	-0.52 ± 0.12	0.19 ± 0.03
Critical shear velocity (cm s^{-1}), u_{*c}	*LotW*	1.27 ± 0.29	1.50 ±0.31	4.55 ±0.25
	Accuracy	± 0.13 (10%)	±0.51 (34%)	±0.57 (13%)
	TKE	2.14 ± 0.02	2.74 ± 0.08	2.79 ± 0.08
	RS	1.56 ± 0.14	Negative RS	1.38 ± 0.10
Critical grain Reynolds number Re_g	*LotW*	32 ± 6	101 ± 17	204 ± 9
	TKE	53 ± 1	185 ± 5	125 ± 4
	RS	39 ± 3	Negative RS	64 ± 5
Critical Shields parameter Θ_c	*LotW*	0.004 ± 0.002	0.002 ± 0.001	0.033 ± 0.003
	TKE	0.0110 ± 0.0002	0.0070± 0.0004	0.012 ± 0.001
	RS	0.006 ± 0.001	Negative RS	0.003 ± 0.001
Viscous sublayer thickness (cm)		5.395×10^{-2}	4.214×10^{-2}	4.138×10^{-2}
Rouse Number range		0.004 to 0.014	0.007 to 0.016	0.006 to 0.015

The critical Shields parameters estimated for maerl from the three methods are plotted with the original Shield's curve and Paphitis (2001) threshold envelope for densities close to those of quartz (Figure 3.8). The critical Shields parameters range from 0.004, for the dead beach sediment, to 0.033 for the intertidal live beds. Samples from all three locations fall below the Shields curve, and the Muckinish LotW estimate just falls within the threshold envelope for densities close to those of quartz. The Muckinish maerl beds have the highest critical bed shear stress (using the LotW and TKE) and are least mobile.

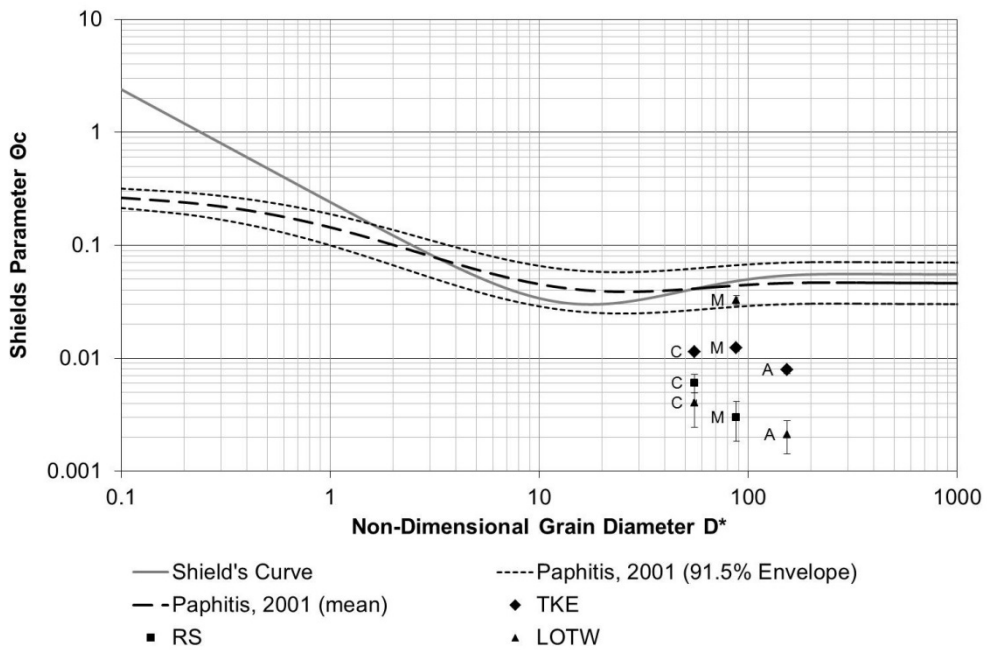

Figure 3.8: Shields curve with envelope and the critical Shields parameters for the three maerl samples. The non-dimensional grain diameter D* is a function of the median particle size, fluid viscosity and specific gravities of particle and fluid (Soulsby 1997).

3.5. Discussion

3.5.1. Experimental results

This study uses three methods to obtain estimates for the critical bed shear stress, critical shear velocity, grain Reynolds number and critical Shields parameter for maerl. The LotW method uses multi-level measurements within the logarithmic layer to detect the presence and thickness of the viscous sub-layer, which might be missed by other methods, e.g. the one-dimensional RS method (Figure 3.7). The Muckinish LotW velocity profile (Figure 3.4) has the most well-defined, highest gradient logarithmic layer associated with higher shear stresses than those for the other maerl samples under similar current conditions. TKE shear stress profiles (Figure 3.5) also suggest that Muckinish maerl has the highest level of near-bed turbulence related to bed roughness. The TI profile (Figure 3.6) also shows that the near-bed turbulence is greatest with the Muckinish sediment, probably because of increased levels of saltation-related roughness (Kim et al., 2000). Video observations confirmed that the saltation paths for Muckinish were the smallest due to secondary interlocking of grains following the initial saltation (Table 3.2).

There is a significant protrusion of the roughest (most branched) maerl grains into the viscous sub-layer, suggesting it is very thin if not absent (Table 3.3), and this alters the critical Shields parameter (Buffington and Montgomery, 1997; Paphitis, 2001). The exposure level of the grains is highest with high relative grain protrusion, resulting in a much lower critical bed shear stress for initiation of motion of maerl, overall when compared to quartz. Smith and Cheung (2003) studied the settling and entrainment characteristics of calcareous sand and found that irregularly-shaped particles result in the break-up of the laminar boundary layer at low grain Reynolds numbers. Miller and Byrne (1966) found that the angle of repose increases with angularity and is a function of the sorting and irregular packing. Mehta and Rao (1985) found that biogenic material such as irregular shaped shells exhibit substantial interlocking frictional forces as a result of shell size, shape, surface roughness, sorting, and packing arrangement (compaction). This leads to grains being mobilised less readily out of its respective grain

pocket due to the inter-granular geometry (Wiberg and Smith, 1987) and explains why Muckinish has a higher critical bed shear stress of the three samples.

The TKE Aran critical bed shear stress is comparable to the Muckinish TKE estimate but the critical Shields parameter is lower, suggesting it is sensitive to grain diameter, even though this is partly compensated by the use of a non-dimensional grain diameter as the ordinate of the Shields curve (Soulsby, 1997). The RS method can result in physically unrealistic negative critical bed shear stresses (e.g., in the $-\rho(u'w')$ component, Figure 3.7) if the flow field is too complex (Biron et al., 2004). Previous studies with siliciclastic grains have suggested that the TKE method gives more precise and reliable estimates than the RS method for the critical bed shear stress (Kim et al., 2000; Thompson et al., 2003; Pope et al., 2006).

Sub-aqueous maerl dunes in the Carraroe and Muckinish samples formed in the annular flume at post-threshold velocities when saltation was the primary mode of sediment transport and significant bed-load transport was occurring. This effect is apparent at the sides of the flumes at shear stresses where currents reach velocities of at least 10 cm s^{-1} greater than the critical threshold velocity for Carraroe and Muckinish sediment (~ 68 cm s^{-1} and 70 cm s^{-1} respectively). It was not possible to obtain the velocity profile and shear stresses at the point of dune formation due to rapid sediment transport altering the bed elevation. This is the first measurement of the critical velocity for sub-aqueous maerl dune formation and its value falls below that for sub-aqueous quartz dune formation of ~80 cm s^{-1} for 0.5 cm grain diameters (Ashley, 1990).

3.5.2. Implications for mobility

Intertidal maerl from Muckinish is the least mobile sediment from the three sampled environments. This is hypothesised to be a consequence of the interlocking thalli of live maerl which are more branched than those found in open marine beds (Steller and Foster, 1995; Joshi et al., 2014) and therefore more likely to resist entrainment. This may be due to the depth-related growth form of the rhodolith (Bosence, 1976, 1983). Aran open

marine maerl exhibits a spheroidal branch growth form (spheroidal II), and sheltered Muckinish intertidal maerl beds exhibit a high degree of rougher ellipsoidal branch growth (ellipsoidal III). Maerl grains with a high branch density are the most convex (Joshi et al., 2014), which increases the drag forces and reduces the settling velocity. The implication is that highly-branched maerl is unstable and, where its low critical shear stresses are exceeded, maerl mobilises easily into suspension *en masse*. Utilising settling velocities from Joshi et al. (2014), the Rouse numbers range from 0.004 to 0.016 (Table 3.3) and are strongly indicative of a very short bedload transport phase, after which all of the sediment is transported as washload transport. This explains the phenomenon observed on the Carraroe maerl beach, where *en masse* transport of maerl as washload is observed in preference to siliciclastic sediments. We suggest that maerl beaches (e.g., the Carraroe locality) with a high percentage of maerl and low percentage of sand form because the lower density and settling velocity of maerl result in its preferential transport over siliciclastic sediment.

The critical bed shear stress is related to other physical attributes of the maerl grains (e.g., grain shape, density, porosity and permeability), which are consequences of environmental factors such as wave action, depth, age of the sediment, and timing of compaction. Grain shape is the critical factor for the relatively low maerl settling velocity which allows maerl to remain in suspension longer than quartz grains (Joshi et al., 2014). We propose that it also strongly determines maerl critical bed shear stress because its greater angularity, degree of exposure to water flow with a thin or absent viscous sublayer, inter-granular porosity, and loose packing, all of which allow grains to be mobilised more readily than quartz grains of a similar size.

The low values of the Shields parameter for maerl (Figure 3.8) may be explained by the fact that grain shape is not included as a parameter when shear stress is normalised to be dimensionless. Similar findings have been found due to the relative grain protrusion experiments of Fenton and Abbott (1977). In this study, values of the critical Shields parameter as low as 0.01 have been reported in "*grains resting on the top of an otherwise flat bed in a turbulent stream*" (Fenton and Abbott, 1977). The irregular grain shape of

maerl is effectively having a similar effect due to the relative grain protusion of the maerl grains.

Live maerl is less dense than dead maerl and maerl grains become denser with age due to increased compaction and exposure of surface pores. The grain densities of sediment samples from Carraroe and Aran are similar and do not produce significant differences in their critical Shields parameters (Figure 3.8); at Muckinish, the effect of the rougher grain shape is more significant than the effect of lower density. The Carraroe and Muckinish beds are moderately well sorted due to the reworking of sediment by continuous wave action in the Carraroe beach locality and tidal currents in the Muckinish intertidal zone; the open marine Aran beds are poorly sorted, due to occasional wave-driven storm activity, which may explain their lower critical bed shear stress. In Carraroe, the dense, irregular material is deposited at the berm and the less dense finer material is transported by wave action, resulting in a grain size gradient from the swash zone to the berm. The mobility of maerl beach sediment may be significantly increased by breaking waves in the swash zone, and the superposition of waves and currents. Symmetrical, sub-aqueous maerl dunes from oscillatory flows, and asymmetrical dunes from wave and current interactions, result in bed-load transport, particularly during storm events (Hall-Spencer and Atkinson, 1999). While our experimental results quantify the influence of steady current velocities on maerl during periods of calm, they also indirectly help the prediction of critical bed shear stress due to wave action (Le Roux, 2003), the primary force governing the seasonality (cyclic variability) of maerl as a habitat forming species (Peña and Bárbara, 2010).

Maerl beds are a highly heterogeneous sediment type and this provides numerous micro- and macro-habitats (Birkett et al., 1998). In Galway Bay, high sediment heterogeneity around the dead and live maerl results in significant ecosystem services value (De Grave and Whitaker, 1999; Sheehan et al., 2015), and, on Carraroe beach for example, the grain size gradient from the swash zone to the berm strongly influences habitat heterogeneity (Christine Maggs, *pers. comm.*). Steller et al. (2009) identified a maerl sub aqueous dune system forming in current-dominated beds under variable current speed where rhodoliths are underlain by carbonate

sediment. This is true for Aran where the currents inhibit the sedimentation of fine and medium sand, and the formation of maerl dunes by winter storm waves results in increased seasonality of maerl mobilisation and its associated epifauna and epiflora (Peña and Bárbara, 2010). Interstices allow burrowing infauna to receive oxygen at depths of ~ 1 m (Hall-Spencer and Atkinson, 1999), providing an ecological niche for rare species such as the sea cucumber, *Neopentadactyla mixta*, present in high densities of 300 m^{-2} in Galway Bay (Gerd Koennecker, *pers. comm*.). By measuring the critical bed shear stress in different environments, the disturbance regimes that determine the structure and function of a benthic habitat can be quantified. Harris and Hughes (2012) stress the importance of identifying the processes affecting the sedimentary environment and the subsequent modelling of the frequency and magnitude of disturbance. This makes it possible to assign a disturbance index to the seafloor, leading to a better definition of the patchiness of a benthic habitat and the development of sediment mobility maps for conservation management and assessment of coastal vulnerability (Kostylev, 2012; Li et al., 2015).

4. Mobility of maerl-siliciclastic mixtures: impact of waves, currents and storm events

This chapter is to be submitted as:

Joshi, S., Duffy, G.P., and Brown, C.,. Mobility of maerl-siliciclastic mixtures: impact of waves, currents and storm events.

4.1. Abstract

Maerl beds are free-living, non-geniculate coralline algae habitats which form biogenic reefs with high micro-scale complexity supporting a diversity and abundance of rare epifauna and epiflora. These habitats are highly mobile in shallow marine environments where substantial maerl beds co-exist with siliciclastic sediment, exemplified by our study site of Galway Bay. Coupled hydrodynamic-wave-sediment transport models have been used to explore the transport patterns of maerl-siliciclastic sediment during calm summer conditions and severe winter storms. The sediment distribution is strongly influenced by storm waves even in water depths greater than 100 m. Maerl is present at the periphery of wave-induced residual current gyres during storm conditions. The combined wave-current sediment mobility index during storm conditions shows correlation with multibeam backscatter and surficial sediment distribution. The combined wave-current Mobilization Frequency Index during storm conditions is an important hydrodynamic variable and acts as a physical surrogate for maerl-siliciclastic mixtures. Sediment mobility modelling can provide useful integrated oceanographic and sediment dynamics information complementing sediment transport and erosion-deposition models.

4.2. Introduction

An understanding of the dynamic equilibrium between erosion and deposition of a sedimentary system is crucial for the identification of sediment transport. This is of relevance to a range of coastal and estuarine activities including the study of morphodynamics, marine conservation, offshore engineering and marine renewable energy (Van Rijn, 1993). This has led to the development of coupled hydrodynamic-wave-sediment transport models for computing the rate of sediment transport due to a combination of waves and currents (Warner et al., 2008; Brown and Wolf, 2009; Bever and MacWilliams, 2013; Hoeke et al., 2013). The dominant physical processes embedded into these models are wind-induced surface gravity waves, tidal currents, and wave-induced currents which take into account radiation stress gradients associated with the horizontal momentum of the waves (Longuet-Higgins and Stewart, 1964; Basco et al., 1982). These are the key forcing functions governing sediment transport in the benthic boundary layer (Jones et al., 2007).

Even in the presence of high-resolution data on the spatial and temporal variations in the wind and wave climate and *in situ* physical properties of seafloor sediment, there is a lack of confidence in the theory and application of sediment transport modelling (Wilcock, 2001; Idier et al., 2010). This is particularly the case when considering uncertainty in cumulative sediment transport due to variations in estimates of sediment input and output as well as estimates of the storage at the sediment source (Schmelter et al., 2012). The quantitative outputs of sediment transport rates may therefore not be reliable. In this study, we recognise the value and limitations of sediment transport models and use sediment mobility modelling as a complementary tool for investigating sediment transport from coupled hydrodynamic-wave-sediment modelling outputs.

Sediment mobility, defined in its simplest form as the percentage of time that grains of a particular size are mobile within a tidal cycle, is an intuitive and practical concept to present sediment transport information based on

hydrodynamic modelling (Idier et al., 2010). Sediment mobility models typically utilise the critical bed shear stress above which incipient motion, mobility, erosion and deposition of sediment occur near the seafloor. Harris and Coleman (1998) utilised a global wave model to estimate global shelf sediment mobility based on empirical threshold speed equations. Porter-Smith et al. (2004) used a similar approach of shear stress threshold exceedance to define regions of the continental shelf with sediment mobility estimations based on wave and tidal energy inputs. Hemer (2006), recognising the need to integrate the magnitude and frequency of seafloor disturbance and sediment mobility due to combined-flow shear stresses, proposed three approaches which have been incorporated, reviewed and standardised by Li *et al*. (2015). Griffin et al. (2008) considered the mobility of sediment based on its grain size distribution rather than the mean grain size. Dalyander et al. (2013) took into account non-linear effects of wave-current interactions by utilising a coupled hydrodynamic-wave model. Li et al. (2015) defined three sediment mobility indices: Mobilization Frequency Index (MFI), Sediment Mobility Index (SMI) and Seabed Disturbance Index (SDI). In this paper, we combine the MFI and SMI with coupled hydrodynamic modelling to assess sediment transport characteristics.

Sediment mobility is affected by geomorphic processes, ocean currents and storm events so it influences sediment rugosity, grain size and turbidity (Harris, 2012c). It is therefore a biophysical variable which can govern the potential and realised hydrodynamic niche of marine organisms and may be considered to be a physical surrogate for benthic species occurrence. It can be utilised as an eco-geographical variable within habitat suitability models for the prediction of spatial patterns of benthic ecosystems (Guisan and Zimmermann, 2000; Kostylev and Hannah, 2007). Harris and Hughes (2012) have examined the mobilisation of sediment on Australia's continental shelf and have defined an ecological disturbance index which considers the recurrence interval of disturbance with respect to ecological succession timescales.

Maerl

This paper is concerned with modelling the mobility of mixtures of maerl and siliciclastic sediment. Maerl (rhodolith) gravel beds are free-living coralline red algae that occur in mobile biogenic sediment deposits in the euphotic zone of shallow marine environments. Its heterogeneous spatial distribution is a consequence of its sensitivity to light intensity, high currents, moderate wave action, low sedimentation and high salinity (Birkett et al., 1998). This often results in autochthonous beds, banks and the formation of subaqueous dunes ~ 0.3m - 2 m high, probably due to oscillatory wave-induced currents (Bosence, 1976). They are often found between islands and adjacent to channels where there are enhanced tidal currents and suppressed waves (Scoffin, 1988; Birkett et al., 1998).

Maerl beds are one of four main macrophyte-dominated benthic communities in the world (Foster, 2001; Basso et al., 2015). They play a primary role as carbonate producers and rhodolith beds are globally significant carbon sinks (Amado-Filho et al., 2012; Adey et al., 2015; Moura et al., 2016). They are of ecological significance with two species, *Lithothamnium corallioides* and *Phymatholithon calcareum*, protected under Annex V of the EC Habitats Directive, with indirect protection under Annex I (EC Council Directive 92/43/EEC). Maerl beds are on the Oslo and Paris (OSPAR) Convention's List of Threatened and/or Declining Species and Habitats (Hall-Spencer et al., 2010). Their spatial distribution contributes to the evidence base for "Seafloor Integrity" and "Hydrographical conditions" Good Environmental Status descriptors in the Marine Strategy Framework Directive (EC Council Directive 2008/56/EC) as biogenic maerl is considered to alter the structure of the seafloor ecosystem (Rice et al., 2012). In Ireland, De Grave (1999) found eel grass-covered live maerl banks in the shallow, low energy parts of Galway Bay and maerl debris facies with varying proportions of sand, mud and shell gravel in high energy areas.

Rhodoliths are known to grow intermittently with a seasonal growth pattern and highest rates in the summer (Adey and Mc Kibbin, 1970; Bosence, 1983). Growth rates have been measured to be 0.55 mm yr^{-1} for

Phymatholithon calcareum and 0.10 mm yr^{-1} for *Lithothamnion corallioides* (Adey and Mc Kibbin, 1970; Birkett et al., 1998). Growth rate has also been found to be inversely related to crust thickness (Steneck, 1986) and maerl species are climax colonisers in conditions of high wave energy in the absence of grazers (Adey and Vassar, 1975). Taberner and Bosence (1985) investigate the co-occurrence of corals and coralline algae, where coralline algae were found to overgrow the corals in the Eocene. A taxonomic gradation has been observed from the rhodolith nucleus to the outer layer due to ecological succession or extrinsic successional control including changes in hydrodynamics (Bosence, 1983; Gherardi and Bosence, 1999; Aguirre et al., 2017). Given the slow and intermittent growth rates, it is likely that the time scales for ecological succession of maerl communities are in the order of decades.

An understanding of maerl hydrodynamic properties is important for re-constructing palaeo-environmental processes and quantifying the range of present, realised ecological niches of maerl (Bassi et al., 2012). Hinojosa-Arango et al. (2009) studied the impact of disturbance on the rich species assemblages associated with maerl in Northern Ireland by comparing a wave-disturbed and a sheltered maerl bed. Campos and Dominguez (2010) obtained sediment mobility on the continental shelf off Brazil using a threshold exceedance approach to locate where the observed orbital velocity exceeds the critical orbital velocity to mobilise sediment. De Falco et al. (2011) utilised a three dimensional hydrodynamic model to study the impact of the hydrodynamic regime on modern maerl carbonate biogenic sedimentation patterns in the western Mediterranean. Elsäßer et al. (2013) modelled the habitat suitability of *Modiolus modiolus* biogenic reefs in Northern Ireland using outputs from a series of coupled hydrodynamic-particle dispersal models. Ayata et al. (2009) used coupled hydrodynamic-advection-dispersion models to model larval connectivity of larval dispersal and settlement of *Sabellaria alveolata* biogenic reefs.

The hydrodynamic parameters of maerl have received little attention from the research community. For sand and maerl gravel mixtures, the critical threshold velocity for incipient motion is a function of the maerl grain diameter (Harris et al., 1996) and its mobility depends upon the different hydrodynamic processes in shallow wave-dominated maerl beds, deep wave-dominated beds and current-dominated beds (Marrack, 1999). There is clear evidence of strong interactions amongst hydraulic energy, maerl grain morphology and sediment mobility (Nelson, 2009; Riosmena-Rodríguez et al., 2011). Maerl have lower settling velocity (Joshi et al., 2014) and lower critical bed shear stress than quartz grains of the same diameter (Chapter 3).

This study focuses on coupled hydrodynamic-sediment transport modelling of a spatially-heterogeneous mixture of maerl gravel and siliciclastic sediment in Galway Bay, containing about two-thirds of all gravel beaches/dunes of dead and live maerl in Ireland (De Grave and Whitaker, 1999), and partially protected in Special Areas of Conservation (SAC). It addresses the following questions: What is the relative importance of the different physical processes operating in Galway Bay, such as wave action, tidal currents, wave-induced currents, for the mobility of maerl-siliciclastic sediment? Which hydrodynamic parameters, such as significant wave height, wave period, residual currents, depth-averaged shear velocity and orbital velocity at the seafloor, are the most influential on sediment mobility and how does their relative importance change from calm to storm conditions? Does sediment mobility modelling provide a more useful approach for understanding seafloor dynamics than sediment transport models? Can sediment mobility act as a physical surrogate for maerl-siliciclastic sediment? How can sediment mobility maps be used in marine spatial planning to minimise disturbance of sensitive ecosystems?

The paper is structured as follows: Section 4.2.2 introduces Galway Bay as the study site, Section 4.3 describes the methodology of the coupled hydrodynamic-sediment transport modelling and the computation of sediment mobility. Section 4.4 presents the results of the sediment mobility modelling for relatively calm conditions during the summer of 2007 and

during extreme storm events in the winter of 2013/2014. Section 4.5 discusses the implications of the results and the utility of sediment mobility indices for conservation and marine spatial planning.

4.2.1. Study Site

Galway Bay is a large bay semi-enclosed at its western end by the three Aran Islands. Galway Bay is defined as 62 km long from west to east, the mouth of the bay is 33 km wide from north to south, and narrows to 10 km at Black Head (INFOMAR, 2016). The three islands are known as Inishmore, Inishmaan and Inisheer (from west to east). The seafloor sediment is underlain by granite in the north of the bay with a major submarine fault (Pracht et al., 2004) juxtaposing Carboniferous karst limestone of the Burren to the south, the most extensive limestone region in north-west Europe (McCabe, 2008). The presence of the Galway Bay fault in North Sound has recently been discovered and documented by the INFOMAR multibeam and LiDAR survey of Galway Bay from 2006-2014 (INFOMAR, 2016). Outcrops of limestone rock are present in the Outer Bay and in the Inner Bay, along with glacial features such as drumlins, sheet moraines and elongated, esker-type gravel ridges (Lei, 1995). The regional climate around Galway Bay is primarily governed by the influence of the North Atlantic Drift and prevailing south-westerly winds, whose combined effect in the Bay is mitigated by the Aran Island. The islands also provide shelter from the largest swell fields of the North Atlantic which significantly influence the regional oceanography. Tides are dominated by the semi-diurnal tidal constituents and are macrotidal (Table 4.1). Outer bay wave data are 6 year seasonal means from a non-directional wave buoy and inner bay wave data are 10 year seasonal means from the Spiddal wave rider buoys (location map and further tidal information can be found in Section 6.2). Temperature and salinity ranges are based on a ROMS model with 6 year seasonal means (MI, 2016).

Table 4.1: Key statistics for oceanography in Galway Bay (Data from Admiralty (2015) and MI (2016).

	Spring	Summer	Autumn	Winter
Tidal Range (m)	4.50m (mean spring tides)		1.90m (mean neap tides)	
Significant Wave Height (m) (mean)	2.78 (outer)	1.95 (outer)	3.08 (outer)	3.89 (outer)
	0.64 (inner)	0.58 (inner)	0.81 (inner)	1.03 (inner)
Wave period (s) (mean)	7.27 (outer)	6.25 (outer)	7.38 (outer)	8.05 (outer)
	3.83 (inner)	3.62 (inner)	3.90 (inner)	4.36 (inner)
Wave Direction (º) (mean (direction))	219 (SW)	229 (SW)	223 (SW)	223 (SW)
Temperature (ºC) (mean ± sd.)	9.79 ± 1.49	15.7 ± 0.93	13.8 ± 1.60	9.01 ± 1.25
Temperature range (ºC) (min. – max.)	6.89 - 12.7	14.0 - 17.7	8.56 - 15.7	5.49 - 11.2
Salinity (mean ± sd.)	33.2 ± 2.43	34.0 ± 1.65	34.0 ± 2.25	33.0 ± 3.28
Salinity Range (min. – max.)	13.3 - 34.9	19.7 - 35.1	12.5 - 35.1	10.0 - 35.1

The net inflow from South Sound is greater than the net outflow from the North Sound, resulting in an anti-clockwise gyre in Galway Bay (Booth, 1975; Lei, 1995) and deposition of sediment in the centre of the Bay (Booth, 1975; O'Connor et al., 1993). The moderate exposure to wave action results in the deposition of fine sand and mud (Keegan, 1972). A higher percentage of silt-clay is found along the northern shore as a result of freshwater input from the River Corrib at the northeast end of the bay (Figure 4.1).

Lei (1995) carried out the first three-dimensional hydrodynamic modelling in Galway Bay. Their model identified the influence of the River Corrib extending to the inner bay, and the north shore where some regions of stratification occur during the summer. There are also several minor tributaries to the west of the Corrib and Lei (1995) concludes that the

freshwater input, together with the prevailing south-westerly wind, governs the oceanographic circulation. Additional freshwater and submarine ground water inputs from the southeast and southern shores (Smith and Cave, 2012) and upwelling of nutrient rich waters at Kilkerrin Bay (Roden and Raine, 1994; Sides et al., 1994) are present but not modelled.

Residual currents are the currents remaining after removal of all oscillatory tidal currents (Pugh and Woodworth, 2014). Lei (1995) reviewed the possible factors affecting residual currents in Galway Bay, including tide-induced, wind-induced and as a result of freshwater input. The study confirmed that wind-induced currents are more important than tide-induced currents. Ren et al. (2015) compared the wind-induced circulation with a wave radar system near a wave energy test site at the north shore and suggested wind shear can propagate to the sub-surface.

Bathymetric constraints are significant in any hydrodynamic model for Galway Bay as they must account for the presence of, for example, accelerated currents known to be associated with the headland of Black Rock and channels created by inlets and islands on the north shore. Interaction of the tidal wave with coastal geometry must also be included in any hydrodynamic model as it gives rise to inequalities in the amplitude and duration of ebb and flood tidal flows resulting in tidal residual currents.

Outside of Galway Bay, the seasonality and structure of hydrographic patterns off the western Irish Shelf are influenced by Eastern North Atlantic Water modified by freshwater input from the River Shannon (Fernandes, 1988; Nolan, 2004). The North Atlantic Oscillation (NAO) influences climatic variability (winter-time temperatures, intensity and frequency of storms) governed by a north-south dipole pressure gradient (Hurrell and Deser, 2009). The increased frequency of storms in Galway Bay is most apparent in the winter storms of 2013/2014 which were associated with a strongly positive NAO anomaly for December 2013 of +3.54 and an average from December 2013 to March 2014 of +2.05; the monthly average

for December 2007 was +1.42 (Osborn, 2016). A total of 12 days of storm (mean wind speed over a 10-minute period > 76 km hr^{-1} or 21 m s^{-1}) occurred in the west of Ireland during December 2013 to February 2014, resulting in high rainfall, strong tidal surges severe flooding, high peak wave periods and extensive coastal erosion (Masselink et al., 2016; Met Éireann, 2016). It has been suggested that the seasonality of maerl and its associated epiflora are due to increased wave action during the winter months (Maggs, 1983; Peña and Bárbara, 2010).

Living and dead maerl dunes and beds using diver survey and acoustic techniques (RoxAnn) have been mapped in Galway Bay especially in and around the SACs (NPWS, 2013). All data have been combined to show areas maerl (Figure 4.1A), with the caveat that the distribution of Aran maerl is based mainly on RoxAnn data and should be treated with caution as maerl has a similar acoustic signature to coarse siliciclastic gravels and biogenic shell hash. Grain size analysis based upon the National Marine Biological Analytical Quality Control Scheme (Mason, 2011). The spatial variation in d_{50}, the median diameter of the log-normal distribution of grain size, from each of the 110 grab samples within Galway Bay, was interpolated by Inverse Distance Weighting (IDW) and subsequently used for the sediment transport model and sediment mobility model calculations (Section 3.4 and Section 3.5 respectively). A d_{50} of 45μm is used for the whole of the Outer Bay, based on the grain size analysis of 70 samples in an area of 978 km^2 in the outer bay (Lordan et al., 2007). The spatial distribution of d_{50} is used to estimate the spatially varying critical Shields parameter necessary for sediment mobility calculations (Section 3.5) and includes a critical Shields parameter of 0.033 for maerl based on laboratory experiments and a density of 2437 kg m^{-3} (Chapter 3).

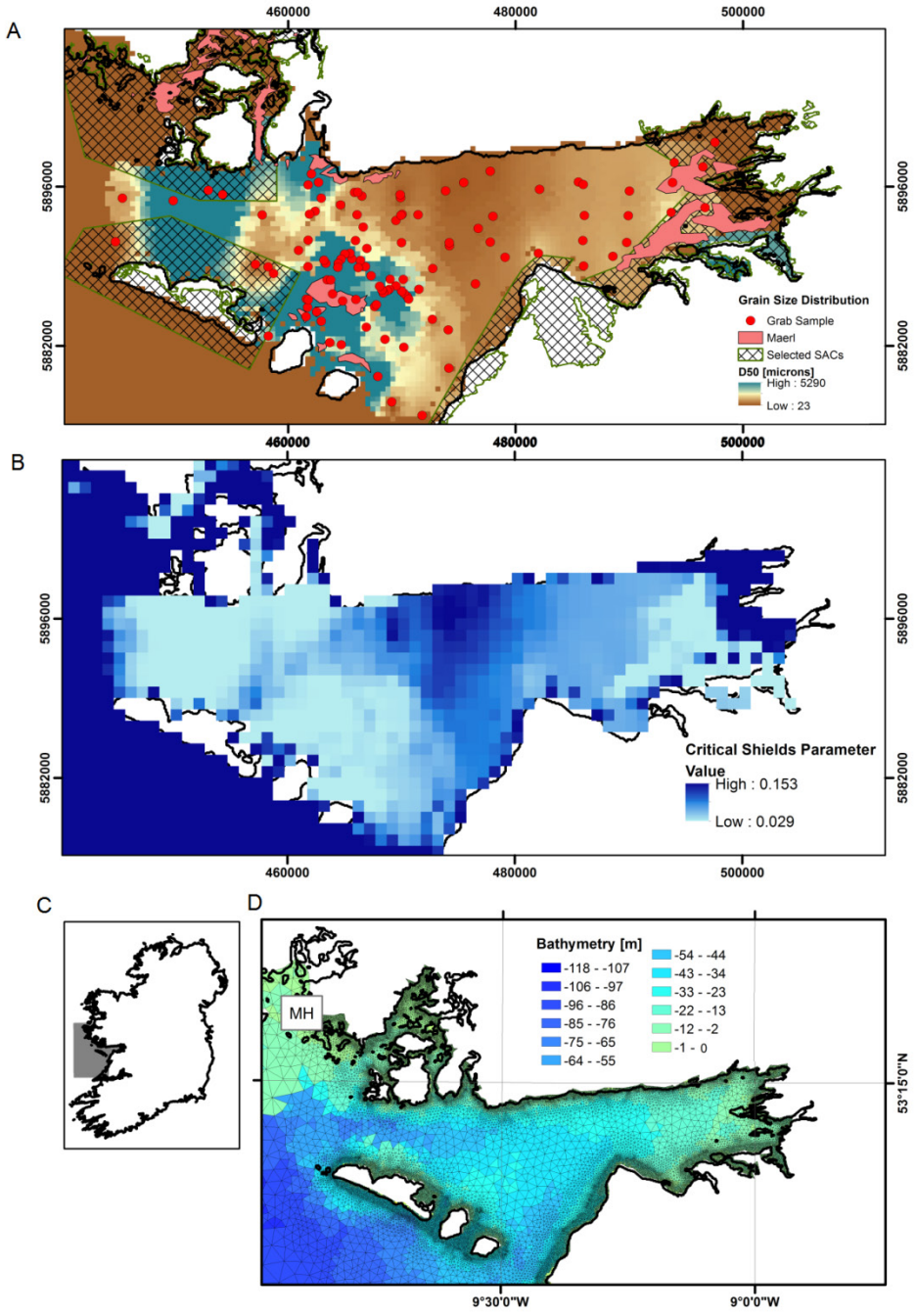

Figure 4.1: Galway Bay study site. Distribution of the median diameter, d_{50} of 110 grab samples of seafloor sediment obtained between March 2009 and August 2010, and maerl beds (A), smoothed distribution of the critical Shields parameter (B), location on the west of Ireland (C), and nested, computational mesh superimposed upon bathymetry (D). MH is the location (53° 19.5 N, 9° 54.25' W) of Mace Head Atmospheric Station. The three islands are known as Inishmore, Inishmaan and Inisheer (from west to east). ADCP and buoy location map can be found in Section 6.2.

4.3. Materials and Methods

Coupled hydrodynamic-wave-sediment transport models were developed in the DHI MIKE 21™ suite of tools (DHI, 2016). The overall modelling strategy is summarised below and the details of the different models are provided in subsequent sub-sections. An initial barotropic hydrodynamic model, MIKE 21™ Coupled Models Flexible Mesh (FM) Hydrodynamic (HD), is used to obtain tidal water levels (surface elevation in m). The 'decoupled mode' was used to enable evaluation and validation at every stage of the modelling before coupling their outputs. These were input into a phase-averaged spectral wave model, MIKE 21™ FM Spectral Wave (SW), which was driven using local wind data from Mace Head. Wave radiation stresses are defined as the time-averaged and depth-integrated total horizontal momentum of the waves less the hydrostatic pressure force (Basco et al., 1982). The SW model generates these wave radiation stresses (S_{xx}, S_{yy}, S_{xy}) which are input into the hydrodynamic model to obtain the wave-induced currents. The wave model and wave-induced current model then drive the MIKE 21™ Sand Transport (ST) model. This provides the sediment transport rate for the spatial distribution of the median grain diameter, d_{50} and the subsequent erosion and deposition for each time step. The outputs of the hydrodynamic model and wave model provide the spatial distribution of current speed, significant wave height and wave period necessary for computing a variety of sediment mobility indices.

4.3.1. Mesh and domain optimisation

The DHI MIKE 21™ FM utilises an unstructured flexible mesh with progressively higher resolution towards the coastlines and islands (Figure 4.1D). The finest resolution nest was deployed adjacent to the coast in < 10 m depths, within the Galway Bay for regions with > 10 m depth, and the coarsest resolution nest outside Galway Bay (Table 4.2). Multibeam echo-sounder and LiDAR bathymetric data (INFOMAR, 2016) were combined with GEBCO 2014 bathymetric data and interpolated onto the computational mesh using MIKE 21™ Mesh Generator and the Analyse Mesh and Refine Mesh tools in the DHI Matlab toolbox.

Table 4.2: Computational mesh used in the coupled hydrodynamic-wave-sediment transport models, with mesh extent map in Section 6.2.

Number of high resolution nests	4
Nest 1 resolution (adjacent to coast)	20 - 100 m
Nest 2 resolution (< 10 m depth)	200 - 320 m
Nest 3 resolution (> 10 m depth)	1.0 - 1.5 km
Nest 4 resolution (outside of bay)	5-6 km
Number of mesh nodes	34 020
Number of mesh elements	64 818
Model time step	600 s
Bed roughness	45 $m^{1/3}/s$
Northern extent	53.68
Southern extent	52.61
Western extent	-10.60
Eastern extent	-8.92

4.3.2. Hydrodynamic Model

The MIKE 21™ HD model solves the shallow water Reynolds-Averaged Navier–Stokes (RANS) equations for each element within the computational mesh (DHI, 2016). The flow rate for the River Corrib at Galway city was averaged to be 103 ± 60 $m^3 s^{-1}$ based on measurements from 1973 - 2005 (OPW, 2016). Tidal boundary conditions were extracted using the Global Tidal Model within MIKE Zero. Calibration of the HD model was carried out by adjusting the uniform value of bed roughness of the 2007 model. The optimal value of 45 $m^{1/3}/s$ of the reciprocal value of the Manning´s roughness coefficient n was utilised (DHI, 2016). The model surface elevations were validated by comparing with the Inishmore tide gauge (MI, 2016). The validation of current speeds was tested by re-running the model with the same parameters (eddy viscosity and bed resistance, riverine inputs) and appropriate tidal boundary conditions for a period in 1994. This was where the last Acoustic Doppler Current Profiler (ADCP)

speeds were measured in Galway Bay, at a site ~14.5 km southwest of the Inisheer lighthouse (52°57'N, 9°39'W) at a thermocline depth of ~ 45m (White, 1995). The original current data were re-processed to ensure data were depth averaged for comparison with the 2DH hydrodynamic model outputs. Residual currents were calculated by averaging the u (x-direction) and v (y-direction) components of the current velocity over a spring-neap tidal cycle to remove the signature of the principal tidal harmonic components (e.g. Bolaños et al., 2014; Pugh and Woodworth, 2014). Wave-driven currents were used in the computation to include factors influencing residual currents (Lei, 1995).

4.3.3. Spectral Wave Model

The spectral wave model, MIKE 21™ SW, solves the wave action conservation equation using the cell-centred finite volume technique (Sørensen et al., 2004; DHI, 2016) with time integration based on a fractional step approach. A fully spectral, instationary formulation is used, where the source terms are based on the WAM Cycle 4 (Komen et al., 1994; Young, 1999). This takes the wave growth due to the wind, non-linear wave-wave interaction, dissipation due to white-capping, bottom friction, depth-induced wave breaking, refraction and shoaling into account (DHI, 2016). Diffraction is partially modelled using a phase-decoupled refraction diffraction approach (Holthuijsen et al., 2003). The Joint North Sea Wave Project (JONSWAP) spectrum is used for initial conditions in the shallow water environment. The wave model requires the boundary conditions for significant wave height, wave period, mean wave directions, directional spreading (index or deviation).

The boundary conditions for the Galway Bay Wave Model in summer 2007 are extracted from the UK Meteorological Office Extended UK Waters Wave Model that has a resolution of 12 km (1/9º latitude by 1/6º longitude) and a model domain from 12°W between 48°N and 63°N (NCOF, 2016). It uses boundary conditions from the Meteorological Office Global Wave Model and is forced by Global Numerical Weather Prediction (GNWP) 10m

winds. One archived data point of 3-hourly output is used at each of the three boundaries, with wind-sea and swell partitioning (NCOF, 2016).

The boundary conditions for the winter storms model of 2013-2014 used an operational implementation of the SWAN model with a resolution of 0.025º (~1.5 km), National Centers for Environmental Prediction (NCEP) Global Forecast System (GFS) wind forcing and the Fleet Numerical Meteorology and Oceanographic Centre (FNMOC) Wave Watch III data for wave boundaries (MI, 2016) (using 10-12 points per boundary). The wave models in summer 2007 and winter 2013/2014 are both forced by the wind measurements at a height of 10m at the Mace Head Atmospheric Station. This facility (Figure 4.1) has wide directional exposure with 60% of air masses from within 180^{o} to 300^{o}. For the summer 2007 wave model, the Spiddal non-directional Waverider buoy at 53^{o}13.6 N, 09^{o}16.02 W is used for validation of significant wave height and wave period. For the winter model, similar data collected by its replacement, the Waverider Mark III buoy at 53^{o}13.7 N, 09^{o}16.13W (MI, 2016) were used for validation.

4.3.4. Sediment Transport Model

The MIKE 21™ ST model is used to obtain the total load (bedload and suspended load, but not washload) sediment transport due to combined wave currents quantified by the sediment transport rate, erosion and deposition. This quasi 3-dimensional model (STPQ3) generates sediment transport tables for all possible combinations of combined wave-current conditions and models the wave-current boundary layer using an integrated momentum approach (Fredsøe, 1984). The grid of spatially varying median grain size (Figure 4.1A) was input to the MIKE Mesh Generator for interpolation onto the computational mesh. MIKE 21™ ST accepts a uniform value for the critical Shields parameter, specified in these models as 0.045 (i.e. > 0.033 for pure maerl) to represent a mixture of maerl and quartz sand. The results of sensitivity tests for a constant critical Shields parameter of 0.06 and density of 2650 kg m^{-3}, appropriate for quartz grains, are presented in Section 6.1 confirm that quartz sand is less mobile than maerl due to its higher critical bed shear stress.

4.3.5. Sediment Mobility Computation

Tidally-induced bed shear stress and shear velocity were calculated for models driven by currents and combined waves - currents (wave only results have not been presented). For the sediment mobility computation, a spatially varying drag coefficient was calculated assuming a logarithmic velocity profile (Soulsby, 1997, Equation 4.1):

$$C_D = \left[\frac{0.40}{\ln(z/h) + 1}\right]^2 \tag{4.1}$$

where h is bathymetric depth and z is the bed roughness length equal to $d_{50}/12$ for hydrodynamically rough flows (Soulsby, 1997). Tidally-induced bed shear stress (τ_c) was calculated using the quadratic stress law:

$$\tau_c = \rho C_D \bar{u}^2 \tag{4.2}$$

where the water density ρ = 1027 kg m^{-3} and $\bar{u}$ is the depth-averaged current velocity. The wave-induced bed shear stress (τ_w) was calculated using the method of Nielsen (1992), with adjusted coefficients from Swart's formula, summarised in Equations 4.3 – 4.8 below. The mean wave period, T and the acceleration due to gravity, g are used to obtain the deep water wave length, L_o and shallow water wave length, L using the explicit approximation of the dispersion relation of linear wave theory (with an accuracy of at least 1.7%) (Fenton and McKee, 1990; Dean and Dalrymple, 2002):

$$L = L_o \left\{ tanh \left[\left(2\pi \sqrt{\left(h/g \right)} / T \right)^{3/2} \right] \right\}^{2/3} \tag{4.3}$$

$$L_o = \frac{g}{2\pi} T^2 \tag{4.4}$$

The wave orbital diameter at the seafloor, d_o also known as the water particle semi-excursion, is then calculated using the significant wave height, H:

$$d_o = \frac{HT}{2\pi} \sqrt{\frac{g}{h}} \tag{4.5}$$

The maximum wave orbital velocity at the seafloor is given by Equation 4.6 (note that this is not the maximum horizontal particle velocity at the seafloor presented in Section 4):

$$u_o = \frac{H}{2}\sqrt{\frac{g}{h}} \tag{4.6}$$

The wave friction factor, f_w is calculated using the Nikuradse roughness length (k_s) (Nikuradse, 1932) , which is equal to skin friction roughness length (i.e. skin friction contribution only without the bedform roughness contribution):

$$f_w = exp\left[5.5\left(\frac{k_s}{d_o}\right)^{0.2} - 6.3\right] \tag{4.7}$$

Finally, the maximum bed shear stress under waves is:

$$\tau_w = \frac{1}{2}\rho f_w u_o^2 \tag{4.8}$$

The Shields parameter is calculated from:

$$\theta = \frac{\tau}{(\rho_s - \rho)gd_{50}} \tag{4.9}$$

where τ is the respective bed shear stress quantity (i.e., τ_c, τ_w) and ρ_s is the sediment density. As sediment mobility is calculated using the magnitude of the shear stress, the total bed shear stress due to the combined wave-current forcing is assumed to be $\tau_{cwc} = \tau_c + \tau_w = \tau$.

The Mobilization Frequency Index (MFI) and the Sediment Mobility Index (SMI), defined by Li et al. (2015) and similar to definitions in Hemer (2006) and Idier et al. (2010), have been calculated over a period of 14 days corresponding to the spring-neap cycle. The MFI corresponds to the percentage of time a grain of a particular size is mobile, i.e. when the critical Shields parameter is exceeded by the observed Shields parameter due to currents, waves or their combination during the spring neap tidal cycle. The SMI, defined by Equation 4.10 below as the combined wave-current bed shear stress divided by the critical bed shear stress (taking the magnitude of

threshold exceedance into account), multiplied by the fraction of time the sediment is mobilised (*MFI* /100). It is a '*non-dimensional index which indicates the sediment mobility integrating both the magnitude and the frequency*' (Li *et al*., 2015)

$$SMI = \left(\frac{\tau_{CWC}}{\tau_C}\right)\left(\frac{MFI}{100}\right) \tag{4.10}$$

The sensitivities of the MFI and SMI resulting from ±20% upper and lower bounds in the errors in significant wave height, wave period and current speed are presented in Section 6.2. If the three parameters are all 20% higher, the MFI increases on average by ~9% for the combined wave-current model. If the three parameters are 20% lower, the MFI decreases on average by ~13%. The equivalent values for the SMI are ~1.5 and ~1.2 with some local variations due to wave breaking adjacent to the coast, especially during the winter storms.

A sensitivity analysis of the sediment mobility indices with respect to the choice of time period over one spring-neap cycle was also conducted. The preferred time period for the summer 2007 and winter 2013 models was based on the spring neap cycle which gave the best fit between the observed and modelled significant wave heights. An additional criterion for winter 2013 was the time period which represented peak storm conditions. The sensitivity analysis demonstrated that sediment mobility was found to be highly-dependent on the choice of time period. By choosing summer calm and winter storm conditions as two end members, the range of the regional sediment mobility, quantified by SMI and MFI, is captured. Both indices are computed across a spring-neap cycle (~ 14 days) using 20 time-step of 17.6 hours. The differences in MFI and SMI for the summer period using 10 time-steps of 35.3 hours instead of 20 time steps are ~ 2.3% ± 7% and ~ 0.04 ± 0.34 respectively, where a standard deviation of 0.34 for the SMI is ~ 7% of the SMI summer range (Section 6.2). A similar calculation for the winter period suggests that a time step of 17.6 hours generates MFI and SMI indices that are accurate to within ± 10%.

4.4. Results and Analysis

The modelling outputs are averaged over two week spring-neap cycles from the 24th July to 7th August, 2007 (Figure 4.2A, B, C), and 15th to 28th December 2013 (Figure 4.3A, B, C). Typically, the significant wave height during summer within the bay does not exceed 1.5 m (Figure 4.2A), mid-period swells in the outer bay are ~ 5-7 seconds (Figure 4.2B) and the horizontal particle velocity at the seafloor, important for the initiation of sediment motion, is less than 0.1 m s^{-1} (Figure 4.2C). Tidal currents are strongest between the Aran Islands, in small bays in the north of Galway Bay and off the southern coast headlands (Figure 4.2D and E). The model confirms the anticlockwise circulation pattern described by Booth (1975) and Lei (1995). The wind velocity rose shows the wind climate is dominated by south westerlies and westerlies (Figure 4.2E).

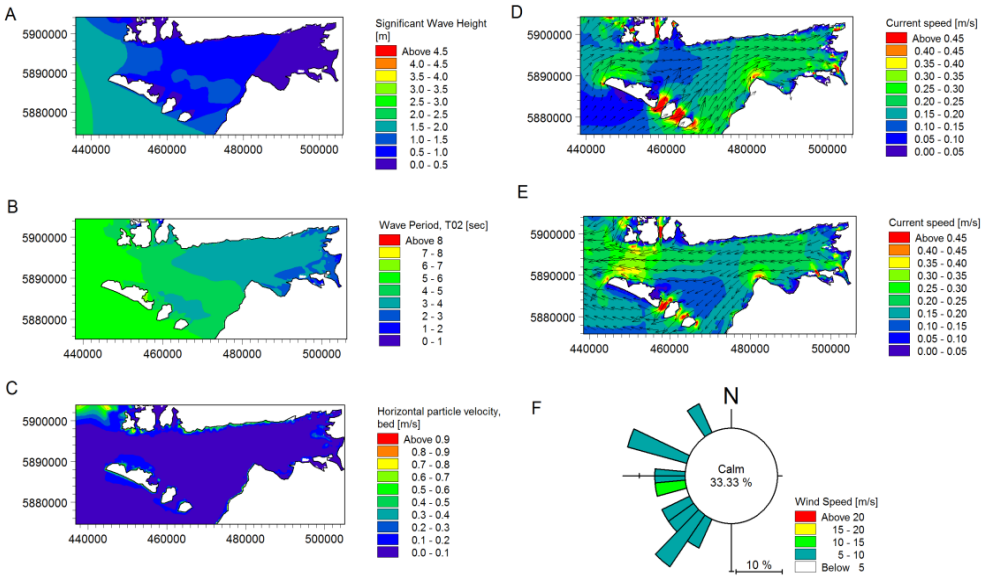

Figure 4.2: Hydrodynamic outputs from summer 2007. Significant wave height (A), wave period (B), horizontal particle velocity at bed (C), depth-averaged current speed (including wave-induced currents) during spring tide flood (D) and spring tide ebb (E), and wind velocity rose at Mace Head over the spring neap cycle (F).

In December 2013, the significant wave height exceeds 2.5 m within the bay and is > 3.5 m in the outer bay (Figure 4.3A); the three Aran Islands reduce the significant wave height and wave periods within the bay (Figure 4.3B).

The horizontal particle velocity at the seafloor (~ 0.5 m s^{-1}) in the inner bay (Figure 4.3C) is five times as large as it is in the summer; it is a measure of the variance of wave-induced orbital motion at bed (Wiberg and Sherwood, 2008). Tidal current speeds are moderate during the storm conditions, though there is a storm surge associated with the NAO anomaly (Figure 4.3D and E). Westerly and south-westerly gusts are dominant (Figure 4.3F).

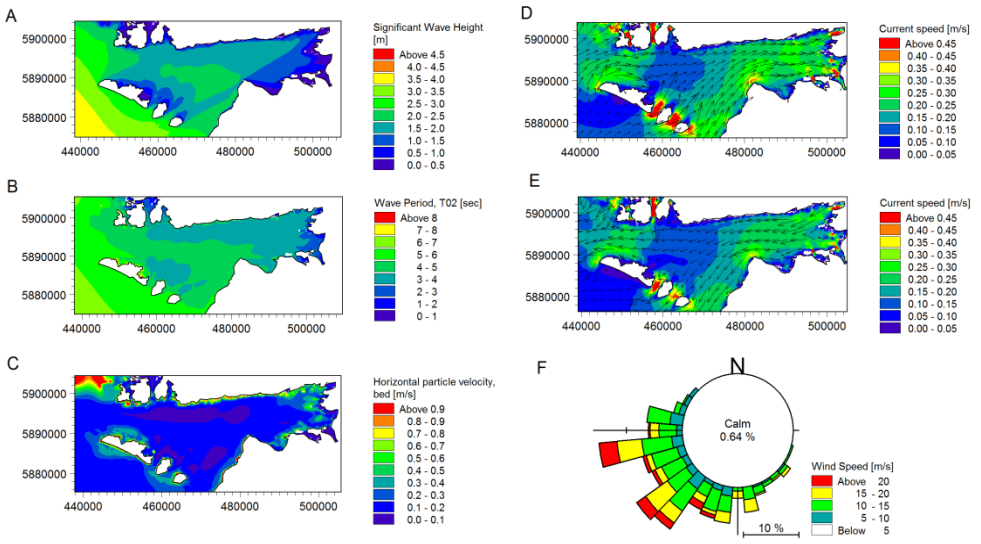

Figure 4.3: Hydrodynamic outputs from winter 2013. Significant wave height (A), wave period (B), horizontal particle velocity at bed (C), depth-averaged current speed (including wave-induced currents) during spring tide flood (D) and spring tide ebb (E), and wind velocity rose at Mace Head over the spring neap cycle (F).

The wave and hydrodynamic model validation (Figure 4.4) demonstrates good fits except for some departures of the modelled wave period from the observed during the most severe storms in December 2013. These are probably due to local gusts of wind at Mace Head that are unrepresentative of the wind-forcing function in the spectral wave model. The bias index or the ratio bias/mean is the non-dimensional mean error, a measure comparing in-situ observations with modelled predictions obtained using DHI's Quality Index tool. The outputs have values of +2% for significant wave height in summer 2007, -15% for significant wave height in winter 2013, -14% for wave period in summer 2007, +14% for wave period in winter 2013 with outliers and +7% for wave period in winter 2013 without outliers, and -2%

for current speed in 1994. The surface elevation gives a fit with a correlation coefficient of 0.99 based upon a bed roughness of 45 $m^{1/3}/s$, equivalent to the reciprocal of the Manning roughness coefficient n (DHI, 2016). Root Mean Square Errors and correlation coefficients can be found in Table 4.3.

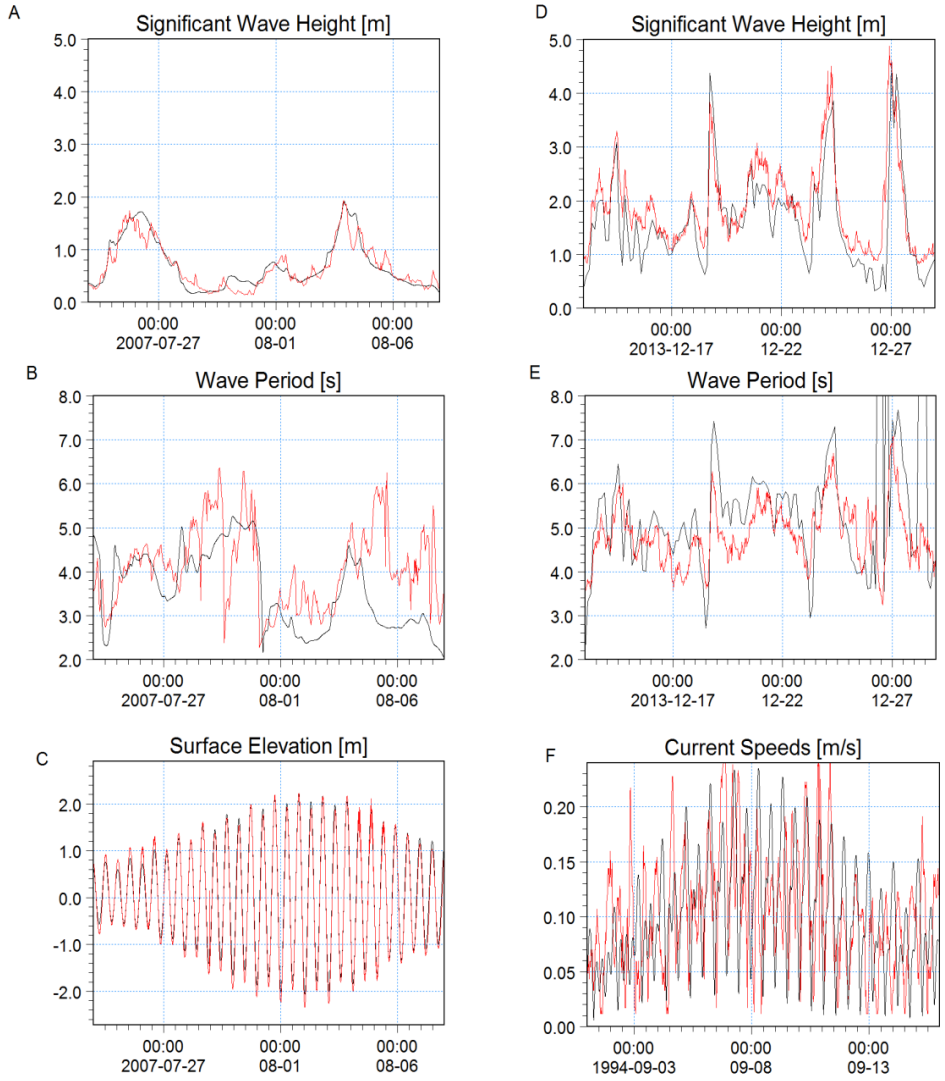

Figure 4.4: Validation of hydrodynamic and wave models with data (red) and theoretical response (black) for significant wave height (A), wave period (B), surface elevation (C) 24th July - 7th August, 2007; significant wave height (D), wave period (E) 15th - 28th December 2013; depth-averaged current speed (F) 1st - 15th September, 1994. The surface elevation was calibrated by reference to the Inishmore tide gauge (-9.6669W, 53.1178 N) which was corrected to same vertical datum (Mean Sea Level-OSGM05) by applying +14.6cm shift (INFOMAR, 2007).

Table 4.3: The Root Mean Square Errors (RMSEs) and correlation coefficients (R^2) for validation of the coupled models

Parameter	RMSE	R^2
SWH (Summer 2007)	0.18 m	0.92
Wave Period (Summer 2007)	1.12 s	0.41
SWH (Winter 2013)	0.53 m	0.86
Wave Period (Winter 2013)	0.73 s	0.66
Current Speed (1994)	0.06 m/s	0.28
Surface Elevation (Summer 2007)	0.14 m	0.99

The shear velocity affects the grain Reynolds number and can be used to characterise the bedload transport rates proportionally. It is a fundamental derived quantity for sediment transport studies as it is the is the square-root of kinematic stress (Sherwood et al., 2006). The peak shear velocities (Figure 4.5), based on the 2DH depth averaged model, are < 0.03 m s^{-1} for the combined wave-currents during the spring-neap cycle in summer 2007 (Figure 4.5B) and up to ~0.08 m s^{-1} during the winter storms in 2013 (Figure 4.5D); the latter is particularly effective for demonstrating the influence of the Aran Islands in shaping the local hydrodynamics of the seafloor. The northern part of the inner bay has a slightly higher shear velocity during storm conditions, a feature relevant for the multibeam backscatter data, presented in the next section.

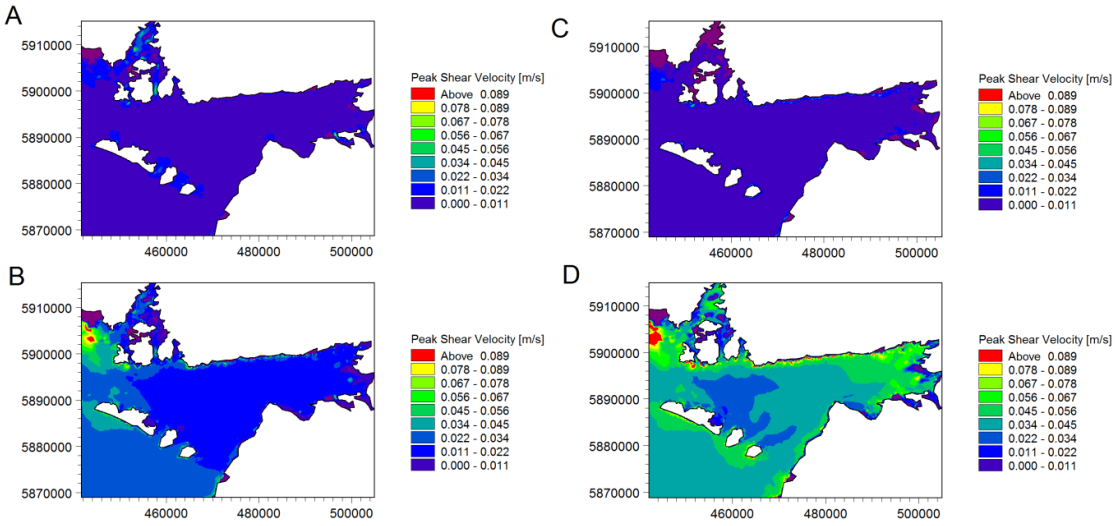

Figure 4.5: Modelled peak depth averaged shear velocity in Galway Bay. Summer 2007 due to currents (A) and combined wave-currents (B), and winter 2013 due to currents (C) and combined wave-currents (D).

Residual currents during summer 2007 (Figure 4.6A) demonstrate an anti-clockwise circulation pattern in Galway Bay, as suggested by previous authors (Booth, 1975; Lei, 1995). Zones of ebb dominance can be identified at the north shore, whereas the south shore and the inner bay show flood dominance. Highest residual currents inside the bay (~0.04 m s^{-1}) in summer 2007 occur south of Rossaveel, an area with maerl beds (Figure 4.6A, see also Figure 4.6C and Section 6.2). During the winter storms of 2013 (Figure 4.6B), the residual currents show anticlockwise circulation, with the presence of two smaller superimposed clockwise gyres northeast of Inisheer. Two gyre features can be observed in the inner Bay with maerl beds at their periphery, indicating that their distribution is the result of current circulation where peak residual current speeds are high. As this feature is only present in storm conditions, this suggests that the wave-induced residual currents are a key force driving maerl distribution. A box plot of the summer 2007 residual currents in maerl and non-maerl areas (Figure 4.6C) confirms a preference of maerl to be located where there are high residual currents; the equivalent box plot for winter 2013 (Section 6.2) does not discriminate maerl and non-maerl areas because the residual currents are all high and both maerl and quartz sediments are mobilised.

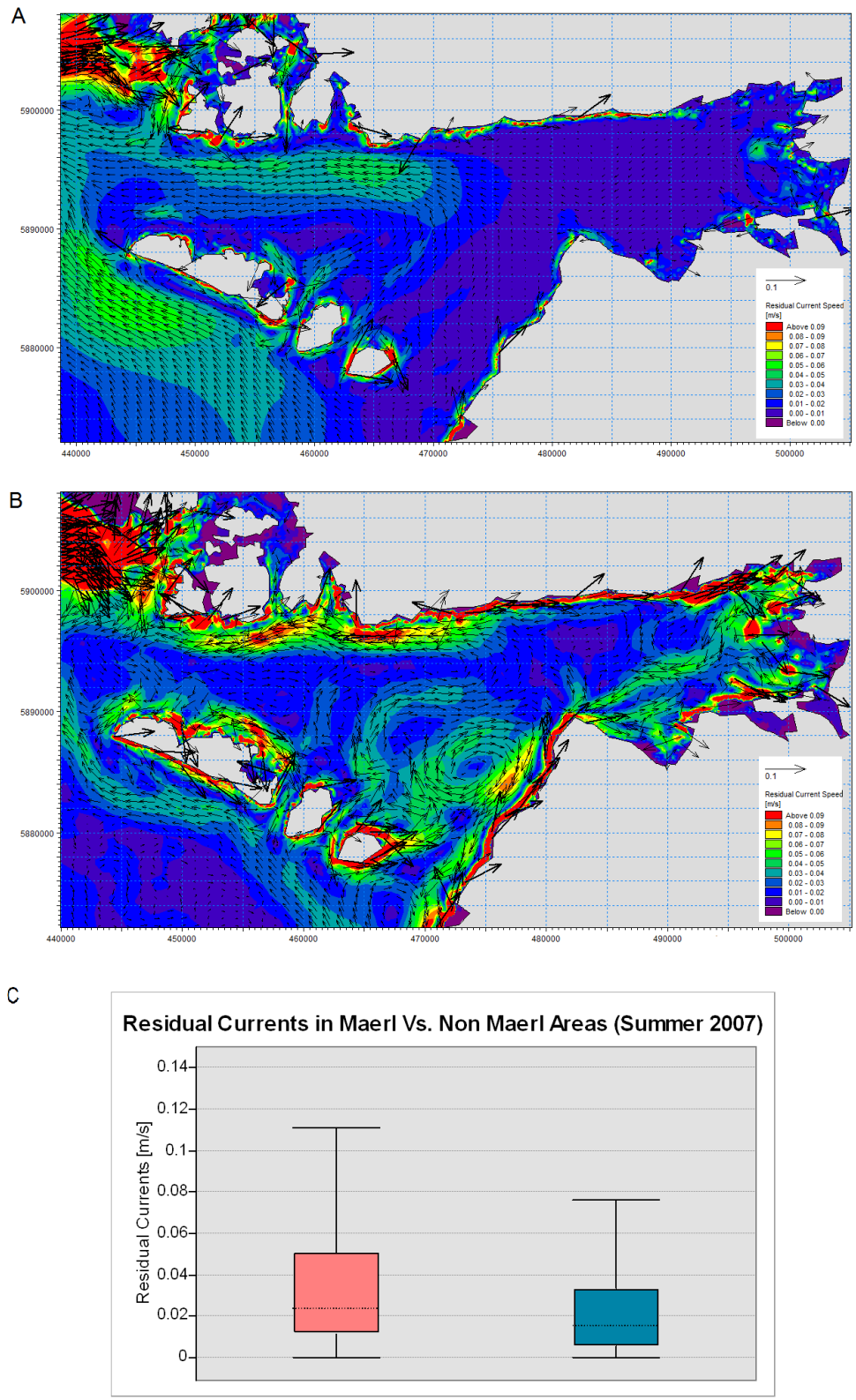

Figure 4.6: Residual currents for the modelling period of summer 2007 (A) and winter 2013 (B), and box plot to show residual currents in maerl areas (pink) and non-maerl areas (blue) during summer 2007 (C).

The Mobility Frequency Index (MFI) is an index which is integrated across a whole spring neap cycle, so it represents a snapshot of the frequency of mobilisation events. It shows that tidally-induced sediment mobility is negligible in summer 2007 and winter 2013 (Figure 4.7A, 4.7D), and demonstrates that Galway Bay is a wave-dominated disturbance regime where the combined wave-current sediment mobility is low to intermediate during the summer and intermediate to high during the winter storm events (Figure 4.7B, 4.7E). The MFI is most influenced by a combination of the combined wave-current regime, critical bed shear stress (Figure 4.7F) and indirectly the grain size distribution (Figure 4.7C). The highest critical bed shear stress values (critical Shields parameter) are in the outer bay and centre of the inner bay and are probably due to flocculation and consolidation of the finest materials (van Rijn, 2007b); the lowest critical bed shear stress values tend to be associated with the maerl beds. Interestingly, the maerl areas have low to intermediate MFI despite their association with low critical bed shear stress. It indicates that high MFI areas will easily mobilise and transport any maerl following erosion of the active layer and suggests that maerl beds are confined to areas below a threshold MFI. It also highlights an important difference between sediment mobility and sediment transport modelling. The latter requires information on the thickness of the active layer of the sediment source whereas the former does not.

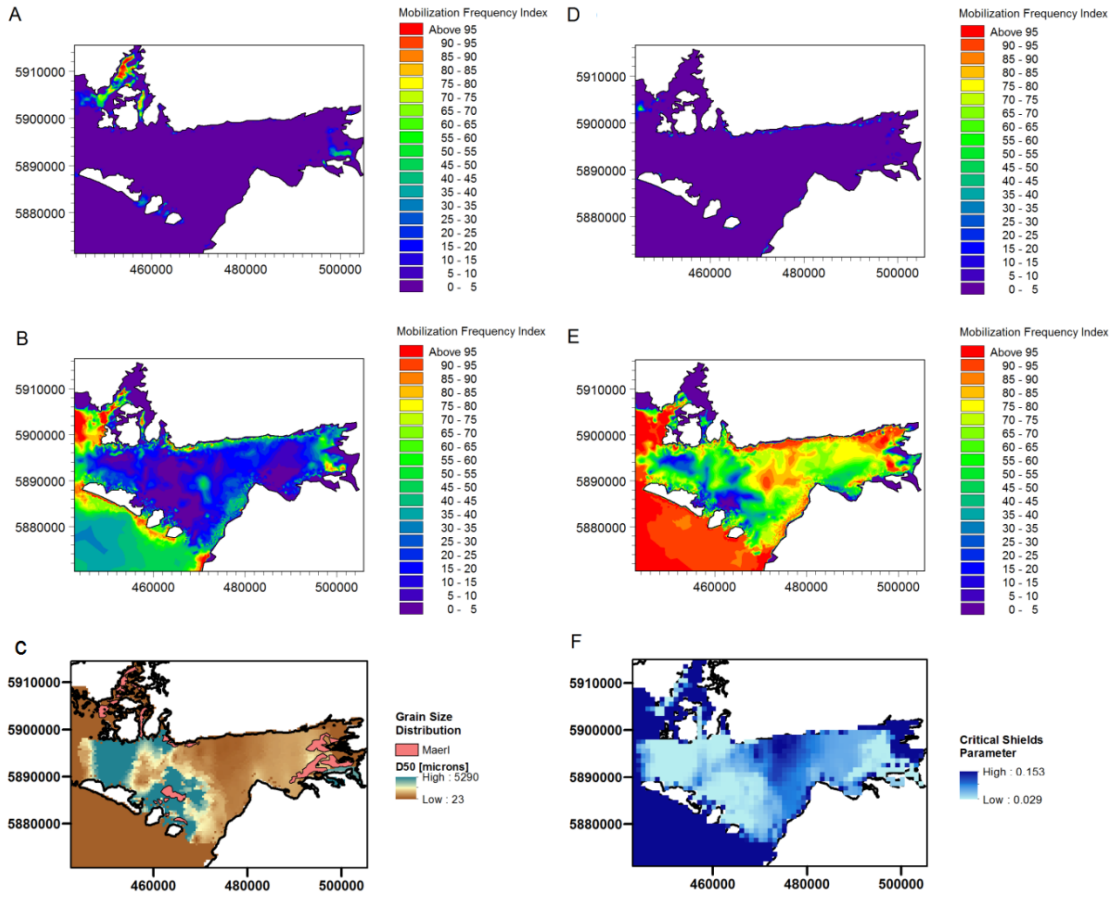

Figure 4.7: Mobilization Frequency Index (MFI) due to currents (A) and combined wave-currents (B) over the spring-neap cycle in summer 2007, and due to currents (D) and combined wave-currents (E) over the spring-neap cycle in winter 2013. Grain size distribution with maerl areas (C) and spatially varying critical Shields parameter (F) have been reproduced from Figure 4.1 to enable comparison.

The Sediment Mobility Index (SMI) for summer 2007 and winter 2013, and multibeam backscatter data acquired in summer 2007 are shown in Figure 4.8. Multibeam backscatter data are independent of the computations for MFI and SMI, and are responsive particularly to seafloor surface roughness (e.g. Yu et al. (2015)) which can act as a proxy for sediment type. There are partial correlations between backscatter strength and SMI. The high backscatter southwest of the Aran Islands is well-correlated with the summer 2007 SMI. A high SMI patch (471000, 5890000 in Figure 4.8A)

can be correlated with high backscatter associated with the edge of rippled scour depressions. The winter SMI distribution, similar to the winter MFI, also shows correlations with the backscatter map. A standard linear correlation analysis within ArcGIS amongst the sediment mobility indices and multibeam backscatter strength is presented in Table 4.4. The results indicate that the multibeam backscatter strength is most correlated with peak sediment mobility occurring during storm conditions in winter.

Table 4.4: Key correlation coefficients (R^2) between sediment mobility indices and backscatter strength

Correlation	Summer 2007	Winter 2013
MFI and Backscatter	0.611	0.804
SMI and Backscatter	0.611	0.798

The winter storms lead to the mobilization of fine sand and siliciclastic muds in the centre of the bay where there is the highest sediment mobility. This suggests that the peak combined wave current sediment mobility during extreme wave conditions is the best hydrodynamic variable governing sediment distribution and is also the best physical surrogate for maerl-siliciclastic sediments. The results show that all the maerl beds have a preference for intermediate mobility environments provided that peak residual current speeds, e.g. those associated with gyres, are high. Rippled scour depressions located northeast of Inishmaan also occur where peak wave-induced residual current speeds are high.

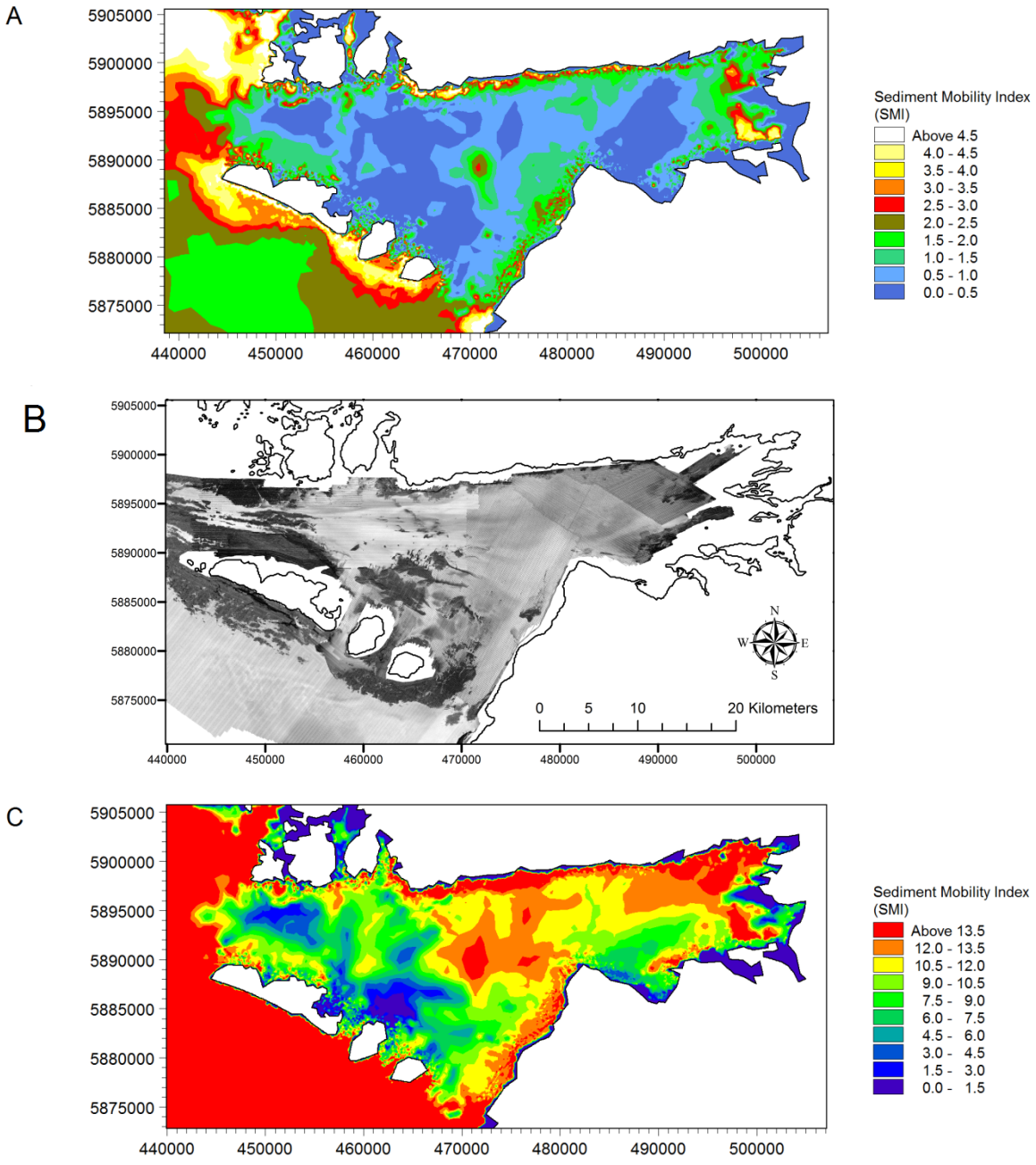

Figure 4.8: Sediment Mobility Index (SMI) for the summer 2007 (A) and multibeam acoustic backscatter (B) with dark areas representing high backscatter and light areas representing low backscatter, and SMI for winter 2013 storms (C). Note the different colour palettes for summer and winter SMI maps to emphasise different SMI levels and facilitate comparisons with the backscatter map.

The sediment transport models give information about the erosion and deposition processes at the seafloor and are not necessarily well-correlated with the sediment distribution. The outputs due to combined wave and currents are summarised as the spatial distribution of seafloor erosion and deposition, and the rate of bed level change for summer 2007 and winter 2013 (Figure 4.9). A deposition patch of fine sediment (mud) in the centre of the bay in summer 2007 (Figure 4.9A) became significantly eroded after the storms of 2013 (Figure 4.9C). There are also significantly higher rates of bed level change adjacent to the coast where there are the highest rates of erosion (Figure 4.9B, 4.9D) and Figure 4.9D shows demonstrable rates of erosion after the winter storms southwest of the Aran Islands and significantly in the inner bay.

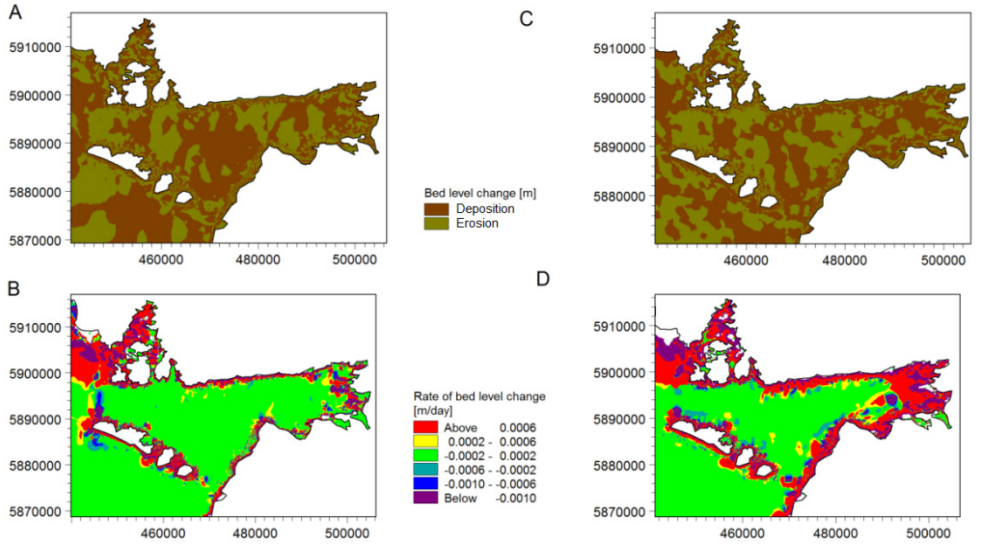

Figure 4.9: Sediment transport model. Erosion (bed level change below 0) and deposition (bed level change above 0) at the seafloor (A) and rate of seafloor level change (B) for summer 2007, and equivalent results for winter 2013 (C) and (D).

The sediment transport total load components vector map with bed level integrated over one spring-neap tidal cycle in 2007 (Figure 4.10A) suggests that sediment is being transported westward out of Galway Bay due to combined wave-currents. Inside of the Aran Islands, there is a lack of sediment transport due to the partial barrier, but during storm conditions, there is a lot more variability in direction (Figure 4.10B) due to extreme wave conditions resulting in variable sediment transport across the bay.

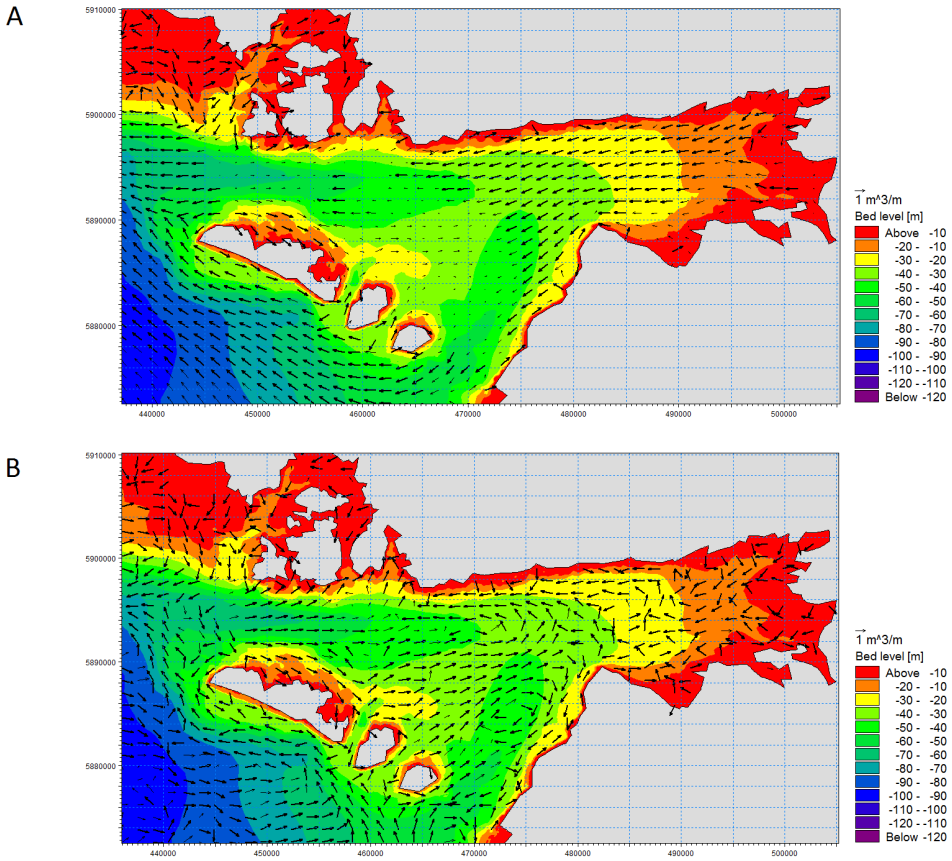

Figure 4.10: Sediment transport vector map of accumulated total load components with bed level over one whole spring-neap tidal cycle in summer 2007 (A) and winter 2013 (B).

4.5. Discussion

The coupled hydrodynamic-wave-sediment transport models have provided a flexible and integrated interpretation of the physical processes occurring at the seafloor. The mobility of siliciclastic and biogenic maerl sediment in Galway Bay demonstrates that storm waves are the dominant driving force for sediment transport, and wave action is significantly more important than benthic currents during periods of calm and storm. Tidal currents are strong enough to mobilise sediment between the Aran Islands and in the bays in the north of Galway Bay (Figures 4.2 and 4.3). The wave climate on the other hand is dynamic and able to mobilise sediments, including maerl, throughout the bay during severe storm conditions. Sediment can be mobilised during severe storms even outside the Aran Islands at > 100m water depth and this is especially significant for structures on or tethered to the seafloor (e.g. salmon farms, wave energy conversion devices).

Harris and Coleman (1998) found that the North Atlantic has the most energetic wave climate globally, with ~0.1 mm diameter quartz sands mobilised at depths of > 200 m, at least once over a three year period. Storm conditions in Galway Bay also mobilise sediment including a zone of mud deposition in the centre of the bay (Figure 4.9C). Harris and Coleman (1998) also observed mobilisation of bioturbated sediment (mud) with high critical bed shear stress on the Australian continental shelf during storms.

Sediment mobility indices show correlations with surficial sediment distribution and multibeam backscatter data, particularly in storm conditions, for areas on the western coast of the Aran Islands (Figure 4.8A, 4.8B). During storm conditions, backscatter also correspond to zones of high - intermediate sediment mobility (Figure 4.8B, 4.8C), such as at the rippled scour depressions northeast of Inishmaan and the area of high backscatter south of the Galway Bay fault line in North Sound. There are also regions of high sediment mobility in the north of the inner bay (Figure 4.8C) which have borders corresponding to backscatter strength gradients (Figure 4.8B). This is likely consequence of the residual current distribution associated with the presence of two gyres in the inner bay during storm

conditions (Figure 4.6B). The depth averaged shear velocity and horizontal particle velocity at the seafloor are useful hydrodynamic variables but do not correlate with the sediment distribution. During storm conditions, the importance of wave orbital velocity becomes less prominent while the normalised bed shear stress for threshold exceedance in the SMI becomes more important because of the greater magnitude of the disturbance events. Therefore, it is suggested that the peak combined wave-current induced sediment mobility during storm conditions is the most important hydrodynamic variable governing sediment and habitat distribution. Residual current gyres are also important for the location of maerl beds and presumably other sediment with low critical Shields parameters.

Sediment mobility modelling provides a useful approach for understanding seafloor dynamics in Galway Bay. Whereas sediment transport models provide information about physical processes, sediment mobility indices provide a picture of the distribution of the frequency and magnitude of threshold exceedance. The advantages of these are that, unlike the MIKE 21™ Sand Transport model, they are not restricted to non-cohesive sediment, and they are easier to use than the Mud Transport model designed for cohesive sediment where flocculation and van der Waals' forces play a significant role (van Rijn, 2007b).

Maerl Sediment Mobility

The combined wave-current sediment mobility during storm situations is the best physical surrogate and hydrodynamic variable for the distribution of maerl. Wave-induced residual currents provide the dominant forces governing maerl distribution and this study indicates that maerl beds are preferentially found in intermediate sediment mobility environments at the periphery of residual current gyres. The upper limit of their hydrodynamic niche occurs where they are in danger of being eroded in the highest mobility environments. This is corroborated by a previous study on the Bonifacio plateau in the western Mediterranean which also demonstrated that maerl beds are located in intermediate mobility environments where they avoid erosion from seafloor currents associated with strong northeast

winds (De Falco et al. (2011). An intermediate mobility environment may also be related to the requirement for clear water for photosynthesis, so ruling out higher mobility environments that increase water turbidity and reduce light penetration (Birkett et al., 1998). The lower limit of the hydrodynamic niche may be governed by the residual currents. The box plot of the residual currents during summer conditions (Figure 4.6C) shows that maerl is found in a wider range of residual currents, with a higher mean (2.40 cm s^{-1}) compared to non-maerl areas (1.55 cm s^{-1}). The MFI 2007 box plot (Section 6.2) corroborates this finding.

Maerl beds are autochthonous biogenic and mobile deposits forming a fragile, complex and patchy habitat. There is evidence for habitat fragmentation where dead maerl beds are located adjacent to live maerl (NPWS, 2013) and this study suggests that this is due to frequent wave-dominated disturbances. This is especially true for the Aran maerl beds, where there is a level of physical patchiness, probably induced by storm waves from different directions, which is than at Carraroe and Muckinish.

The ratio of live to dead maerl is a proxy for the quality of the shallow water benthic habitat (Hall-Spencer et al., 2008; NPWS, 2013). The increased sediment heterogeneity around the dead and live maerl results in significant ecosystem services value for a diversity of flora and fauna (De Grave, 1999; Sheehan et al., 2015). It has also been suggested that edge effects of the maerl bed affects the rate at which organisms can migrate into the maerl (Jason Hall-Spencer, *pers. comm*.), resulting in further biological patchiness of organisms within the maerl habitat. Harris and Hughes (2012) have explored hypotheses for the existence of patchy landscapes associated with re-occurring disturbances affecting areas of the Australian continental shelf.

Implications of Climate Change on Rhodoliths

Hydrodynamic controls of biogenic reef systems are of importance to the associated biodiversity distribution, larval dispersal, fate of pollutants, and response to ocean acidification, as well as the overall response to physical disturbance (Hoeke et al., 2013). A study by Brodie et al. (2014) on the

impact of a high CO_2 world on benthic flora suggests climate-driven increased storminess is one of the factors which leads to a biogeographical shift in the range of free-living non-geniculate calcified red algae, particularly at their northern limit, where they are likely to disappear and be replaced by non-calcified fleshy algae. Maerl structure is also sensitive to the rate (rather than the magnitude) of ocean acidification (Kamenos et al., 2013) which alters its magnesium-calcium ratio (Melbourne et al., 2015; Ragazzola et al., 2016). Both effects suggest that the integrity of maerl beds will be impacted by climate change, particularly during the winter.

Implications for conservation management

Sediment mobility is of relevance to two descriptors in the Marine Strategy Framework Directive: Descriptor 6 '*The sea-floor integrity ensures functioning of the ecosystem*' and Descriptor 7 '*Permanent alteration of hydrographical conditions does not adversely affect the ecosystem*'. Both descriptors must be taken into account for marine spatial planning to minimise environmental degradation in the face of an expanding maritime economy (Flannery, 2011). Maerl is a bioengineer and a biogenic substratum-forming species in need of protection to ensure seafloor integrity of the wider ecosystem (Rice et al., 2012).

In terms of the hydrography, it is possible to utilise sediment mobility indices when quantifying the seafloor exposure of an ecosystem and analyse the impact of the storm events on the seafloor. Long term studies on the recurrence interval of natural disturbance events would enable quantification of the Ecological Disturbance Index (Harris and Hughes, 2012).

Sediment mobility indices can be used to quantify the disturbance regimes of regions of the continental shelf and assign biogeographically representative MPAs which contain both disturbed and undisturbed patches (Harris, 2012b). This research could help assess whether the criteria of *Comprehensiveness, Adequacy and Representativeness* of MPAs (CAR principle of marine conservation) are met in Galway Bay (ANZECC

TFMPA 1999). The first principle asks if the network of MPAs is *Comprehensive* and does it take the full range of ecosystems into account? In Galway Bay, the SACs are protecting differing ranges of maerl habitats such as duned beach systems, live branched maerl beds and more nodular forms, and dead algal gravels. In Galway Bay, the SAC network is comprehensive, with the exception of the Aran maerl areas around Inishmaan and Inisheer. The second principle requires the network to have an *Adequate* level of reservation. In Galway Bay, one could argue that the EU Habitats Directive Annex V level protection of "being subject to management measures" is too low for pristine live maerl beds not subject to anthropogenic disturbance for over a century. Additionally, many rarer species are not protected due to difficulties in species identification. The third principle asks if the protected areas are *Representative* of the biotic diversity of the marine ecosystems. In Galway Bay, one could also argue that preference should be given to live maerl beds which are the most productive and diverse habitats. However, it is important to conserve the entire range of ecosystems and sediment mobility may be a way of regionalizing the seafloor (Porter-Smith et al., 2004) to guarantee representation.

Sediment mobility maps can be used in marine spatial planning to minimise the disturbance of sensitive ecosystems. An understanding of the sediment transport pathways around a region is of great importance for managing conflict associated with anthropogenic activity. For example, the potential location of Europe's largest salmon farm close to the maerl beds at Inisheer could have detrimental effects on maerl habitats (Hall-Spencer et al., 2006; Sanz-Lázaro et al., 2011). Knowledge of sediment transport pathways is critical for understanding transport processes such as dispersal of salmon waste and food remains. Planned harbour expansion in Galway Bay could result in shipping routes near maerl areas in the inner bay and lead to invasive species such as the slipper limpet (*Crepidula fornicata*), introduced through ballast water, out-competing the maerl. This can result in maerl beds becoming smothered with silt (Grall and Hall-Spencer, 2003).

Maerl beds are also associated with habitats that are particularly sensitive to anthropogenic activity such as scallop dredging (Hall-Spencer and Moore, 2000) and commercial extraction (BIOMAERL, 1999). They act as a biological surrogate for species richness and are important for the storage of blue carbon (Maggs, 1983; Harris, 2012c; Burrows et al., 2014). Given the correlations of sediment mobility indices with multibeam backscatter, the incorporation of SMI and MFI into habitat suitability models which use multibeam bathymetry and backscatter, oceanographic and other environmental proxies including light intensity (Reiss et al., 2011; Martin et al., 2014; Mohn et al., 2014) may improve tools for predicting the potential locations of maerl beds and devising conservation management strategies.

5. Conclusions

This thesis has determined a range of hydrodynamic properties of maerl and incorporated the results into coupled hydrodynamic-wave-sediment transport models and sediment mobility models. In Chapter 2, the settling velocity of maerl from three different environments has been experimentally determined as being lower than that of quartz grains with an equivalent sieve diameter. The settling velocity curve at diameters > 2mm for maerl is flat in comparison to the curve for quartz, between 200 - 250 mm s^{-1}. These experimental results are rigorously compared with two theoretical approaches; Dietrich (1982) and that of Ferguson and Church (2004).

The Ferguson and Church (2004) equation for settling velocity has been modified with a fixed constrained C_1 parameter and linearly varying C_2 parameter, which is related to drag coefficient and the grain size dependent roughness. Detailed analysis of the grain shape metrics (caliper elongation, circularity and convexity) reveals that the reciprocal of convexity has a grain-size-dependency, increasing linearly with diameter. This is related to the branch density, especially at the intertidal maerl beds at Muckinish, which have the highest branch density. This results in an increasing drag with grain size, resulting in a lower settling velocity of maerl in comparison with quartz grains of an equivalent sieve diameter. This relationship is also confirmed as the drag coefficient converges to the asymptotic value of the linearly varying C_2 parameter as diameter increases. Comparisons with previous data from Komar and Reimers (1978) show a local minima at Re ~ 220 in maerl settling velocity curves in drag coefficient-Reynolds number space, after which grain shape effects dominate maerl behaviour.

In Chapter 3, the critical bed shear stress of maerl has been determined for three different sedimentary environments (beach, intertidal and open marine) in Galway Bay, west of Ireland. Three techniques (Law of the Wall, Turbulent Kinetic Energy and Reynolds Stress) have been employed in a rotating annular flume and linear flume. Maerl has significantly lower

critical bed shear stress than quartz sediment with the same sieve diameter, primarily due to its highly-irregular grain shape leading to a greater relative grain protrusion of maerl, increasing the drag experienced by individual maerl grains. The lower critical bed shear stress increases the likelihood for suspension. Therefore, maerl is more readily mobilised and transported than quartz sediment, resulting in its preferential transport on beach and open marine environments. The critical Shields parameter is close to the lower boundary of the Shields curve envelope for siliciclastic material for intertidal samples with high inter-grain forces due to convex grain shapes; for beach samples; a small Shields parameter is consistent with easily mobilised, rounded grains.

The LotW method discerns significant differences in the critical Shields parameters amongst maerl samples from three sites with different environmental conditions. The TKE critical bed shear stress estimates provide consistently low critical Shields parameters that are similar for the samples from all three locations. This implies that the TKE method, based on a point sample at one elevation, is not as sensitive as the LotW method, based on sample points at several elevations, for differentiating the effects of maerl grain shape. One-dimensional principal RS critical bed shear stresses were under-estimated due to negative stresses arising from one or both of the other velocity components. Chapters 2 and 3 provided fundamental sediment transport parameters, settling velocity and critical bed shear stress, for an assessment of the spatial distribution of maerl sediment mobility using numerical models of currents, waves and sediment transport in the next chapter.

In Chapter 4, sediment transport of maerl-siliciclastic mixtures in coastal marine environments were examined and dynamic maerl sediment mobility maps were computed for use in conservation management. Regional scale coupled hydrodynamic-wave-sediment transport models in DHI MIKE 21™ FM were validated during calm summer and winter severe storm conditions. Wave induced radiation stresses were coupled to model the wave-induced currents and combined wave-current sediment transport. Models were

utilised to obtain two sediment mobility indices; the Mobilization Frequency Index; based on the frequency of threshold exceedance of the Shields criterion and the Sediment Mobility Index; based on the magnitude and frequency of threshold exceedance. A combination of forcing factors (combined wave-current flow) and sediment hydrodynamic properties affect the seafloor disturbance regime. Maerl is present in areas at the periphery of a residual current gyre during storm conditions. This is also likely to affect the lower limit of the hydrodynamic niche of maerl, with maerl being absent to areas with the lowest residual currents.

Sediment mobility can be partially correlated with multibeam backscatter. The peak combined wave-current induced sediment mobility during storm conditions was identified as the key hydrodynamic parameter governing sediment distribution in Galway Bay. Furthermore, it was argued that the Mobilization Frequency Index during storm conditions is a physical surrogate for maerl, which is able to survive in intermediate mobility environments, free from silt deposition (so photosynthesis is possible) and without the threat of being eroded by high combined-wave current related shear stresses. Wave-induced residual currents are likely to be a key force driving maerl distribution. This study is of importance to a range of scientific disciplines including biological conservation and essential for engineering problems related to the seafloor. Sediment mobility maps provide useful integrated physical oceanographic and sediment dynamics information to inform robust marine spatial planning.

Recommendations for Further Research

There is scope for further research in all three parts of this study. Firstly, the modified Ferguson and Church (2004) universal equation for settling velocity, with linearly varying C_2 parameter could be corroborated with independent data of branched maerl from other study sites. This would allow an exploration of the propensity of maerl to form banks of a high percentage maerl to quartz sand observed in Galway Bay (Chapter 2).

The critical bed shear stress experiments in Chapter 3 were conducted on natural sediment mixtures rather than individual grain size fractions and could be repeated for individual grain size fractions. The effects of differing grain size and shape in mixtures lead to selective transport (Buffington, 1999) so experiments could be conducted to quantify a correction factor to account for the hiding and exposure effect of fine sediment from flow by larger highly-irregular maerl particles (Egiazaroff, 1965; Day, 1980; Buffington and Montgomery, 1997; van Rijn, 2007c). Experiments with improved measurement techniques could also consider the effect of oscillatory flow (waves) on maerl sediment mobility and non-linear effects of wave-current interactions on the benthic boundary layer. The process of maerl dune formation could then be quantified to allow for predictions of field-scale processes using scaling laws (Hughes, 1993).

The peak combined-wave current induced Mobilization Frequency Index was suggested as the best physical surrogate for maerl-siliciclastic mixtures. This study has been able to study two end member "snapshots" of the dynamic sediment mobility continuum. Further studies comparing the variability of the MFI index could be made for different time periods. Following this, it can be an important hydrodynamic variable to include in habitat suitability models to predict the distribution of maerl in areas where distribution is unknown. These predictions will also require ancillary data on the light intensity limits of maerl (where present) as well as a spatially varying map of depth of the euphotic zone (where absent).

The long term wave climate could be analysed to model storminess in the next 50-100 years. The recurrence interval of storm events could be studied in detail and compared with timescales of ecological succession of maerl and other benthic species to quantify the Ecological Disturbance Index. This could utilise the DHI Climate Change Toolbox, which models the impact of Intergovernmental Panel on Climate Change (IPCC) scenarios on the regional hydrodynamic model.

This work could be extended to include impact scenarios of ocean acidification on maerl with varying structural integrity. It would also require conceptual models of the life cycle of a rhodolith as a carbonate grain (Folk and Roubles, 1964) to account for grain abrasion, erosion and disintegration. Unlike quartz grains that are relatively hard and difficult to fracture in the natural environment, many carbonate grains are soft and easily broken down when mobilised.

Recommendations for Maerl Conservation and Marine Spatial Planning

- Maerl prefers intermediate sediment mobility environments, with an intermediate combined wave – current benthic disturbance regime.
- Maerl is present in areas at the periphery of wave-induced residual current gyres during storm conditions.
- It is able to survive with low turbidity so it is able to photosynthesize, but not be eroded by the strongest storm events.
- In Galway Bay, the dominant hydrodynamic factors affecting the distribution of surficial sediment (including maerl) is the peak combined wave-current induced sediment mobility during storm conditions.
- Anthropogenic activity, e.g. salmon farms, needs to be avoided, in accordance to existing environmental legislation.
- Maerl has potential to form part of representative networks of Marine Protected Areas (MPAs), to protect against increasing anthropogenic activity and increased storminess as a result of climate change.
- The protected areas with maerl are Comprehensive and Representative, however the level of protection is considered to be Inadequate.
- Commercial extraction of maerl needs to be banned in Ireland as it is a non-renewable resource with low recoverability, suggested by their preference for intermediate disturbance regimes and slow growth rates (Grall and Hall-Spencer, 2003).
- In Europe, protection of maerl should include *Lithothamnion glaciale* to Annex V of the Habitats Directive (Birkett et al., 1998).

6. Appendices

6.1. Appendix 1- Paper 2

6.1.1. Pangaea Database

Three Data files and two videos in a zip file can be found at the following link: http://doi.pangaea.de/10.1594/PANGAEA.825359

6.1.2. Summary of Error Analysis

The error analysis suggests that errors are consistent with those in previous literature. The TKE shear stress measurements give the smallest precision errors of 2%-6%; the LotW shear stress errors are 9%-39%. The precision errors of the shear velocity and the Shields parameter derived from the TKE method based on triplicate time series are smaller than previously determined estimates of 20%-30% (Biron et al. 2004) and 10%-37% (Wilcock 1996).The precision errors in the RS and LotW measurements are consistent with previously reported results, i.e. ~ 10% for the Carraroe samples, ~ 34% for Aran and ~ 13% for Muckinish. These result in an error in the critical bed shear stress of ~ 20%, 25% and 68% respectively, probably due to the propagation of error in a poorly defined logarithmic layer and turbulent interference in the Aran sample. An additional propagation of error into the derived quantities stems from errors in the estimation of sediment density and median grain size. The LotW critical Shields parameter is especially low for the Aran sample probably as a result of its less well defined logarithmic layer at Aran (where the coefficient of determination for the linear relationship between velocity and logarithm of elevation above the bed is $r^2 = 0.92$ compared to $r^2 = 0.99$ for Carraroe and Muckinish); its higher grain size, poor sorting and the flow field in the linear flume may also be responsible for an underestimation of its critical Shields parameter. Other general sources of error include imperfect log-linearity of the velocity profile, errors in measured velocities, errors in the elevation measurement and errors in measuring the bed elevation (Wilcock 1996). For example, a rotation of 2.5º of the ADV in the rotating annular flume leads to a 2.2 mm error in the elevation.

6.1.3. TKE and Reynolds Stress Errors

The TKE shear stress errors, TI errors, TKE shear velocity errors, one dimensional Reynolds Stress errors, three dimensional Reynolds Stress errors, RS shear velocity and Shields parameter errors were obtained using the triplicate measurements.

Table 6.1: TKE and RS triplicates, and Shields parameters with errors, for Carraroe.

Carraroe	TKE shear stress	RS	Shields parameter TKE	Shields parameter RS
1	0.4620	2.0090	0.012	0.050
2	0.4467	1.8888	0.011	0.047
3	0.4620	1.9837	0.012	0.050
Average	**0.4569**	**1.9605**	**0.011**	**0.049**
Precision	0.009 (± 2%)	0.063 (± 3%)	0.0002 (±2%)	0.002 (±3%)

Table 6.2: TKE and RS triplicates, and Shields parameters with errors, for Aran.

Aran	TKE shear stress	RS	Shields parameter TKE	Shields parameter RS
1	0.7936	-0.3946	0.007	Negative RS
2	0.9056	-0.6369	0.009	Negative RS
3	0.8082	-0.5264	0.008	Negative RS
Average	**0.8358**	**-0.5193**	**0.008**	Negative RS
Precision	0.0609(±7%)	0.1213(±23%)	0.0006 (±7%)	Negative RS

Table 6.3: TKE and RS triplicates, and Shields parameters with errors, for Muckinish.

Muckinish	TKE shear stress	RS	Shields Parameter TKE	Shields Parameter RS
1	0.7537	3.1416	0.012	0.050
2	0.7530	3.1612	0.012	0.050
3	0.8358	3.4806	0.013	0.055
Average	**0.7808**	**3.2612**	**0.012**	**0.051**
Precision	0.048(± 6%)	0.190(±6%)	0.0007(±6.1%)	0.003(±5.8%)

6.1.4. Sensitivity to Elevation

A sensitivity analysis has been carried out to determine the sensitivity of the Shields parameter to the choice of bed elevation for the TKE and point-based RS measurements. We have chosen an elevation of 10% of the flow depth for our study to be consistent with the recommendation of Biron et al. (1998).

Table 6.4: Sensitivity analysis due to choice of bed elevation for Carraroe TKE.

Bed Elevation ± 0.2 cm	% flow depth	TKE shear stress	Shields parameter
3.5	13.5	0.454 ± 0.014	0.011 (-0.3%)
3.2	12.4	0.431 ± 0.029	0.011 (-5.3%)
2.67 (present study)	**10.4**	**0.455 ± 0.009**	**0.011**
2.3	9.0	0.476 ± 0.011	0.012 (4.6%)
2.1	8.1	0.521 ± 0.018	0.013 (14.5%)
2	7.8	0.521 ± 0.012	0.013 (14.5%)

Table 6.5: Sensitivity analysis due to choice of bed elevation for Aran TKE.

Bed Elevation ± 0.1 cm	% flow depth	TKE shear stress	Shields parameter
3.5(5.5)	22	0.595 ± 0.042	0.006(-28.8%)
3 (5)	20	0.663± 0.037	0.006(-20.7%)
2.5(4.5)	18	0.668 ± 0.043	0.006(-20.1%)
2 (4)	16	0.697 ± 0.055	0.007(-16.7%)
1.5 (3.5)	14	0.749 ± 0.044	0.007(-10.3%)
1 (3)	12	0.829 ± 0.034	0.008 (-0.8%)
0.5 (**2.5**) **(present study)**	**10**	**0.836 ± 0.061**	**0.008**

Table 6.6: Sensitivity analysis due to choice of bed elevation for Muckinish TKE.

Bed Elevation ± 0.2 cm	% flow depth	TKE Shear Stress	Shields parameter
3.5	13.5	0.657 ± 0.044	0.010 (-15.8%)
3.2	12.4	0.650 ± 0.025	0.010(-16.8%)
2.67 (present study)	**10.4**	**0.781 ± 0.048**	**0.012**
2.3	9.0	0.840± 0.071	0.013(+7.6%)
2.1	8.1	1.029± 0.020	0.016(31.8%)
2	7.8	1.120 ± 0.026	0.018(43.5%)

Table 6.7: Sensitivity analysis due to choice of bed elevation for Carraroe RS. Aran RS values are negative so the Shields parameter was not obtained using this technique.

Bed Elevation ± 0.2 cm	% flow depth	RS	Shields Parameter
3.5	13.5	0.207 ± 0.043	0.005 (-17.3%)
3.2	12.4	0.252 ± 0.115	0.006 (0.5%)
2.67 (present study)	**10.4**	**0.250 ± 0.045**	**0.006**
2.3	9.0	0.267 ± 0.015	0.007 (6.5%)
2.1	8.1	0.191 ± 0.067	0.005 (-23.6%)
2	7.8	0.190 ± 0.033	0.005 (-23.9%)

Table 6.8: Sensitivity analysis due to choice of bed elevation for Muckinish RS.

Bed Elevation ± 0.2 cm	% flow depth	RS	Shields parameter
3.5	13.5	0.448 ± 0.196	0.007 (133.3%)
3.2	12.4	0.416 ± 0.202	0.007 (116.6%)
2.67 (present study)	**10.4**	**0.192 ± 0.030**	**0.003**
2.3	9.0	0.119 ± 0.082	0.002 (-37.8%)
2.1	8.1	0.273 ± 0.131	0.004 (42.3%)
2	7.8	0.453 ± 0.164	0.007 (136.1%)

6.1.5. Extrapolation and Analysis of the Principal Reynolds Stress

Biron et al. (2004) details two methods to obtain the critical bed shear stress via the RS parameter; the point measurement of principle Reynolds stress within the logarithmic constant stress layer and the Reynolds extrapolation method. The total shear stress estimated from the latter method is the sum of the Reynolds stress and viscous stresses:

$$\tau_{RS} = -\overline{u'}\overline{w'} + \nu\frac{\delta\overline{u}}{\delta z} \qquad (6.1)$$

In the case of the total bed shear stress, when z corresponds to 0, principle Reynolds stress at the bed can be determined by extrapolation of the principal Reynolds stress profile from 0.2 < z/H <0.7, in the region where viscous stress play a negligible role. Therefore in (11), the viscous stress can equate to zero and it is possible to determine the critical bed shear stress (at threshold conditions). In this study we have employed both these methods, ultimately choosing the point measurement of Reynolds stress obtained at 0.1 of the flow depth as the most appropriate measure. In our case, we attempted extrapolation of RS profiles from only 0.2 < z/H < 0.4 of the flow depth giving unrealistic estimates and therefore we feel the point measurement of Reynolds Stress is more reliable. An example of RS extrapolation for Muckinish has been included below. Extrapolation of the principal Reynolds Stress profile gave values which were too low, negative and unrealistic in the case of the Muckinish sample. This is suggested to be due to only < 40 % of the flow depth being sampled, rather than 70%.

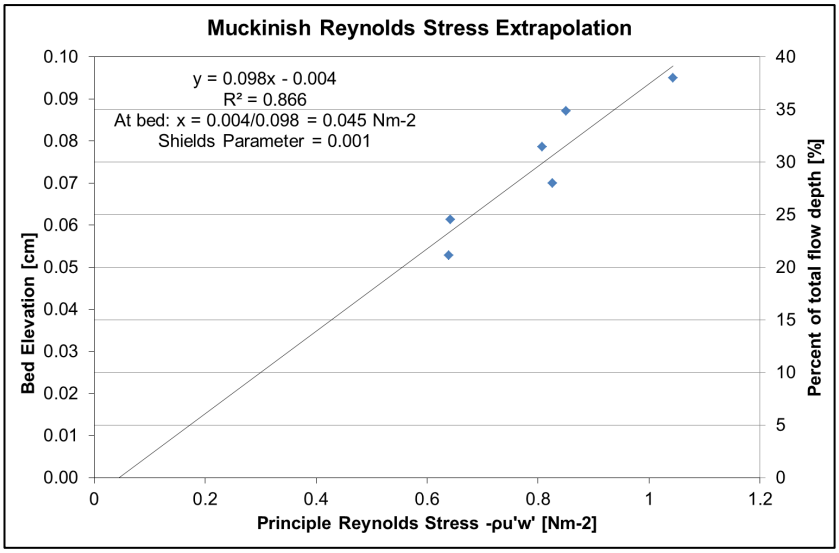

Figure 6.1: Extrapolation and Analysis of the Principal Reynolds Stress for Muckinish intertidal sample.

Table 6.9: The quadrants for the points at 0.1 of the flow depth at threshold conditions are a useful way of identifying the dominant turbulent process at the point.

	u'	**w'**	**Turbulence Process**	$-\rho(\overline{u'w'})$
Quadrant 1	Positive	Positive	Outward Interaction	Negative
Quadrant 2	Negative	Positive	Ejections	Positive
Quadrant 3	Negative	Negative	Inward Interaction	Negative
Quadrant 4	Positive	Negative	Sweeps	Positive

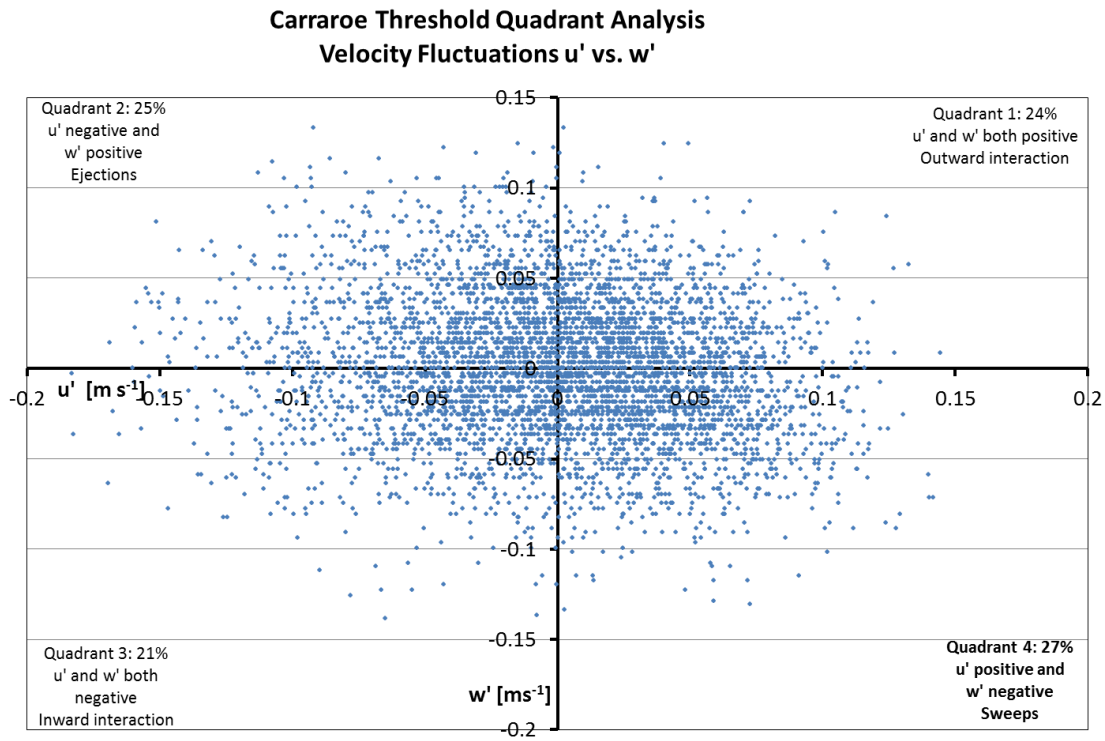

Figure 6.2: Carraroe Threshold Quadrant Analysis

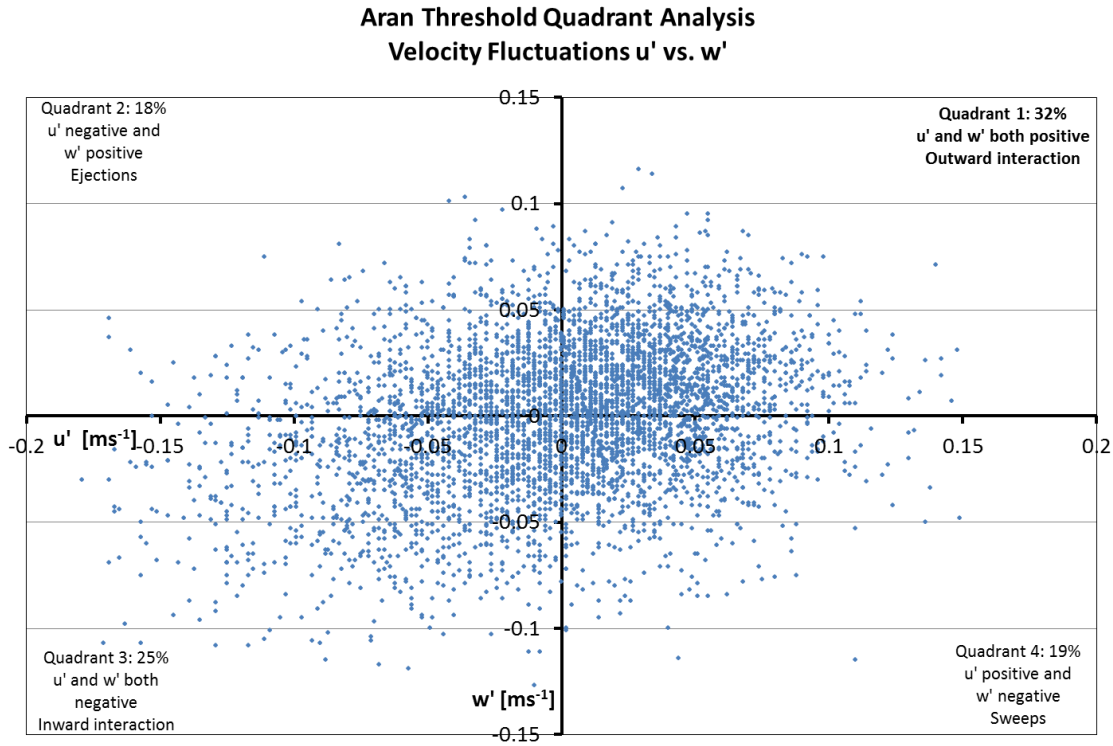

Figure 6.3: Carraroe Threshold Quadrant Analysis

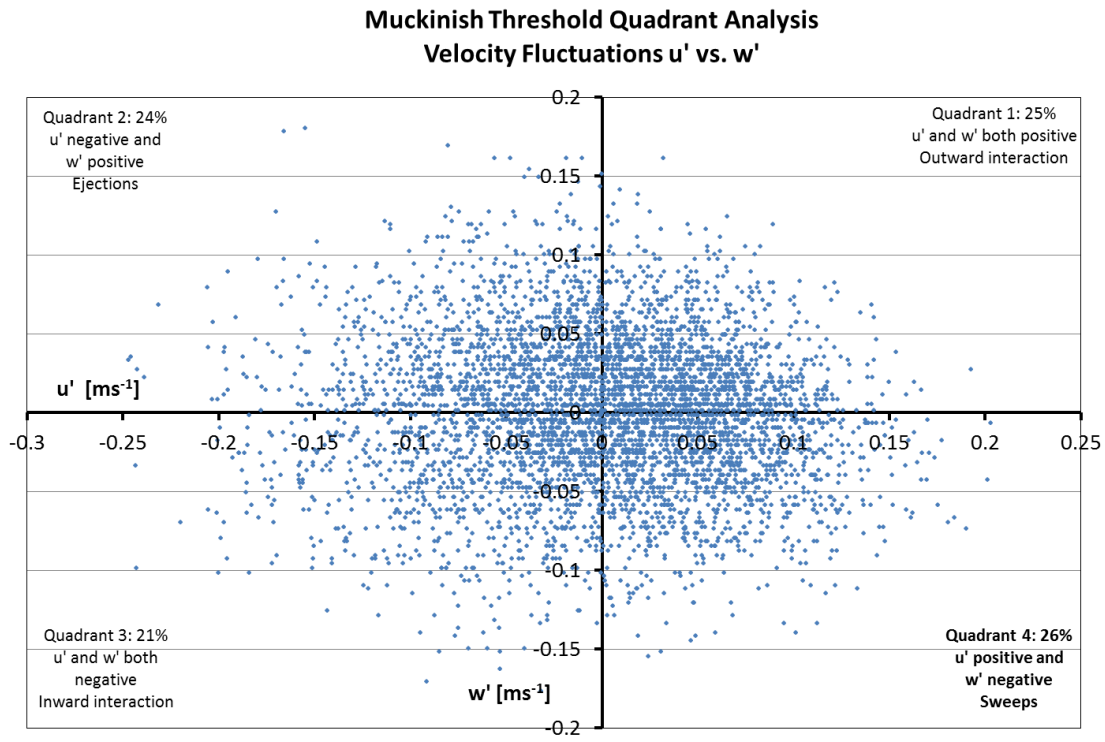

Figure 6.4: Carraroe Threshold Quadrant Analysis

6.1.6. Law of the Wall (LotW) with Replicates

This section illustrates the three LotW replicates of velocity (m/s) versus the natural logarithm of elevation (m) for each sample and demonstrates the errors in the gradient and intercept. The average gradient is determined by two methods (1) a linear regression of the average of the three velocities at each elevation with the logarithm of the elevation, and (2) a linear regression of all velocity points versus logarithm of elevation for each of the samples. In this study we have chosen Method 1 (bold font).

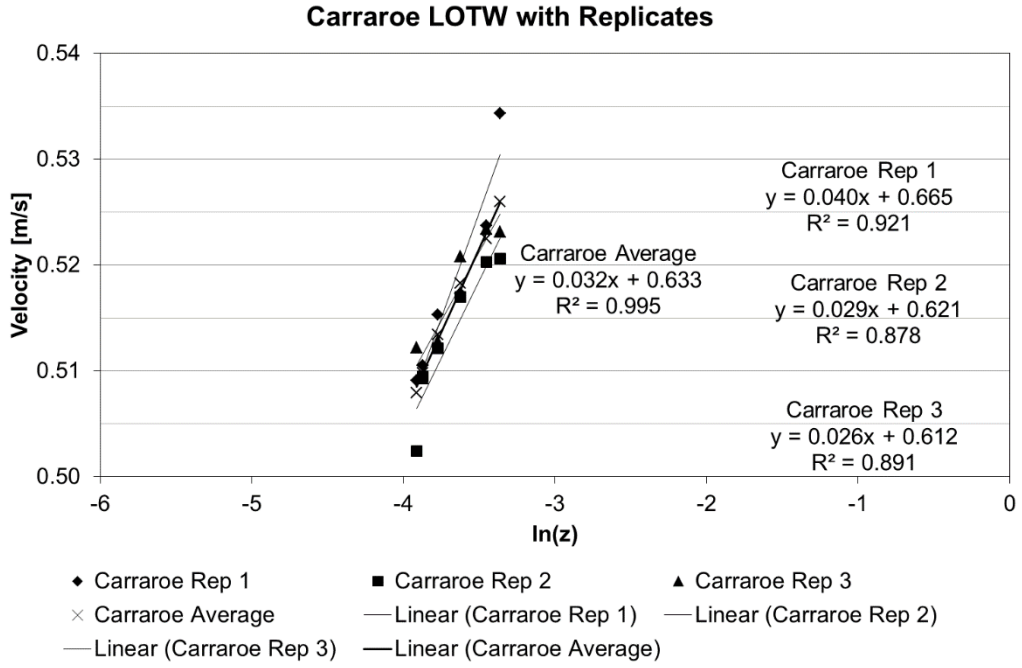

Figure 6.5: Carraroe Law of the wall with replicates.

Table 6.10: Precision errors using the law of the wall methodology at Carraroe.

Carraroe	Gradient	Shear Velocity U* (cm s^{-1})	Critical Shear Stress	Shields parameter
Replicate 1	0.040	1.60	0.26	0.006
Replicate 2	0.029	1.18	0.14	0.003
Replicate 3	0.026	1.04	0.11	0.003
Average (2)	0.032	1.27	0.16	0.004
Average (1)	**0.032**	**1.27**	**0.16**	**0.004**
Precision		**0.29 (±23%)**	**0.06 (±39%)**	**0.002 (±39%)**

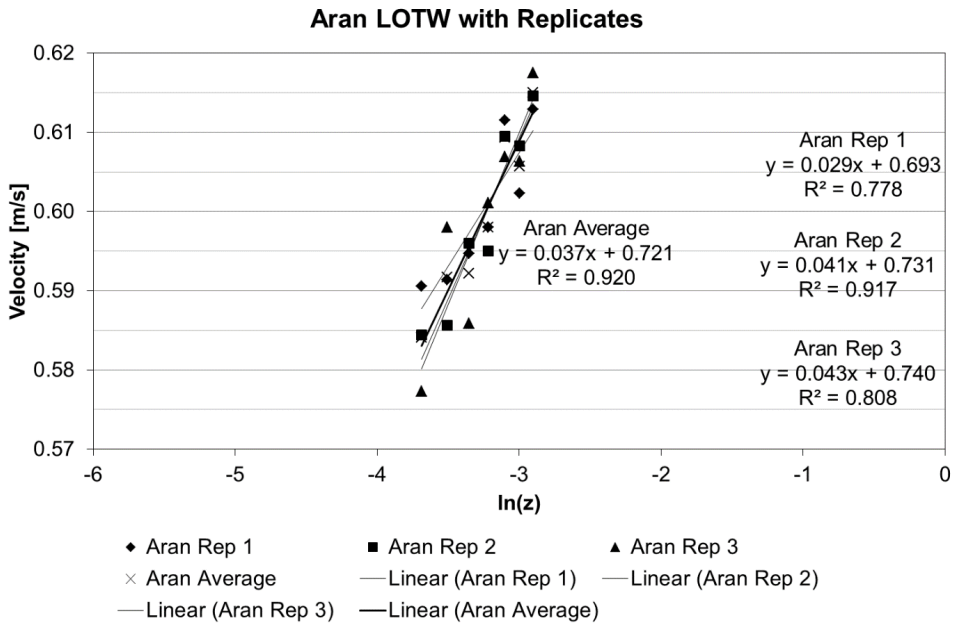

Figure 6.6: Aran Law of the wall with replicates

Table 6.11: Precision errors using the law of the wall methodology at Aran.

Aran	Gradient	Shear Velocity U* (cm s^{-1})	Critical Shear Stress	Shields parameter
Replicate 1	0.029	1.14	0.13	0.001
Replicate 2	0.041	1.62	0.26	0.002
Replicate 3	0.043	1.73	0.30	0.003
Average (2)	0.037	1.50	0.22	0.002
Average (1)	**0.037**	**1.50**	**0.22**	**0.002**
Precision		**0.31(±21%)**	**0.07(±33%)**	**0.001(±33%)**

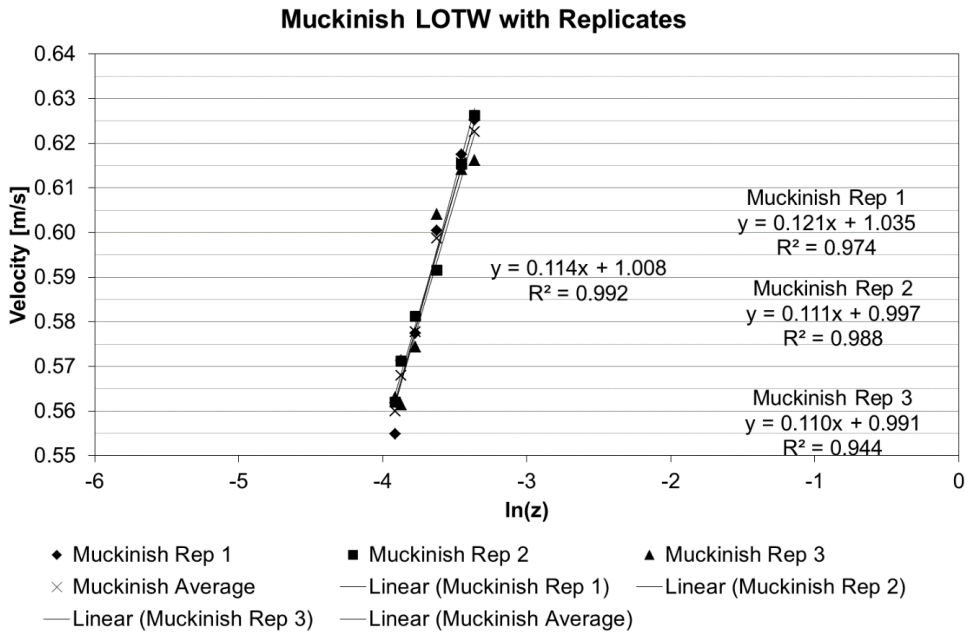

Figure 6.7: Muckinish law of the wall with replicates.

Table 6.12: Precision errors using the law of the wall methodology at Muckinish.

Muckinish	Gradient	Shear Velocity U* (cm s^{-1})	Critical Shear Stress	Shields parameter
Replicate 1	0.121	4.84	2.34	0.037
Replicate 2	0.111	4.43	1.96	0.031
Replicate 3	0.110	4.39	1.93	0.030
Average (2)	0.114	4.55	2.07	0.033
Average (1)	**0.114**	**4.55**	**2.07**	**0.033**
Precision		**0.25 (±5.5%)**	**0.19 (±9.1%)**	**0.003 (±9.1%)**

6.1.7. Law of the Wall Error using Wilkinson (1983)

Wilkinson (1983) was used to obtain the accuracy of the bed shear stress, $\delta\tau$ and shear velocity, δu_* for the LotW measurements based upon the estimated error in the gradient δm:

$$\delta\tau = 2u_*\rho\kappa\delta m \quad \text{(1a)}$$

$$\delta m = \frac{t}{\sqrt{(N-2)}}\frac{\sigma_y}{\sigma_x}\sqrt{(1-r^2)} \quad \text{(1b)}$$

Carraroe:

$$\delta m = \frac{2.776}{\sqrt{(6-2)}}\frac{0.00718}{0.2253}\sqrt{(1-0.9947)} = 0.0032$$

$$\delta u_* = 0.129\ cm\ s^{-1} \quad (10.2\%)$$

$$\delta\tau = 0.033\ N\ m^{-2} \quad (20.3\%)$$

Aran:

$$\delta m = \frac{2.571}{\sqrt{(6-2)}}\frac{0.0110}{0.2825}\sqrt{(1-0.9198)} = 0.0127$$

$$\delta u_* = 0.509\ cms^{-1} \quad (34.0\%)$$

$$\delta\tau = 0.152\ N\ m^{-2} \quad (68.1\%)$$

Muckinish:

$$\delta m = \frac{2.776}{\sqrt{(6-2)}}\frac{0.02581}{0.2253}\sqrt{(1-0.9920)} = 0.0142$$

$$\delta u_* = 0.569\ cms^{-1} \quad (12.5\%)$$

$$\delta\tau = 0.518\ N\ m^{-2} \quad (25.0\%)$$

The percentage errors in the shear velocity and bed shear stress are ±10.2% and ±20.3% respectively for Carraroe, ±34.0% and ±68.1% for Aran, and ±12.5% and ±25% for Muckinish.

6.1.8. Grain Size Distribution

SIEVING ERROR: -0.2%

SM8: Grain Size Distribution

SAMPLE IDENTITY: **Carraroe**

SAMPLE TYPE: Unimodal, Moderately Well Sorted TEXTURAL GROUP: Sandy Gravel

SEDIMENT NAME: Sandy Very Fine Gravel

	µm		GRAIN SIZE DISTRIBUTION	
MODE 1:	2400.0	-1.243	GRAVEL: 72.1%	COARSE SAND: 0.0%
MODE 2:			SAND: 27.8%	MEDIUM SAND: 0.0%
MODE 3:			MUD: 0.2%	FINE SAND: 0.0%
D_{10}:	1508.6	-1.991		V FINE SAND: 0.0%
MEDIAN or D_{50}:	2434.9	-1.284	V COARSE GRAVEL: 0.0%	V COARSE SILT: 0.0%
D_{90}:	3975.2	-0.593	COARSE GRAVEL: 0.0%	COARSE SILT: 0.0%
(D_{90} / D_{10}):	2.635	0.298	MEDIUM GRAVEL: 0.6%	MEDIUM SILT: 0.0%
(D_{90} - D_{10}):	2466.6	1.398	FINE GRAVEL: 9.0%	FINE SILT: 0.0%
(D_{75} / D_{25}):	1.676	0.556	V FINE GRAVEL: 62.5%	V FINE SILT: 0.0%
(D_{75} - D_{25}):	1292.0	0.745	V COARSE SAND: 27.8%	CLAY: 0.0%

	METHOD OF MOMENTS			FOLK & WARD METHOD		
	Arithmetic µm	Geometric µm	Logarithmic	Geometric µm	Logarithmic	Description
MEAN ($\bar{x}$):	2732.2	2467.9	-1.303	2450.7	-1.293	Very Fine Gravel
SORTING	1221.5	1.566	0.647	1.484	0.570	Moderately Well Sorted
SKEWNESS (Sk):	2.045	-3.027	3.027	0.076	-0.076	Symmetrical
KURTOSIS (K):	9.643	45.04	45.04	1.036	1.036	Mesokurtic

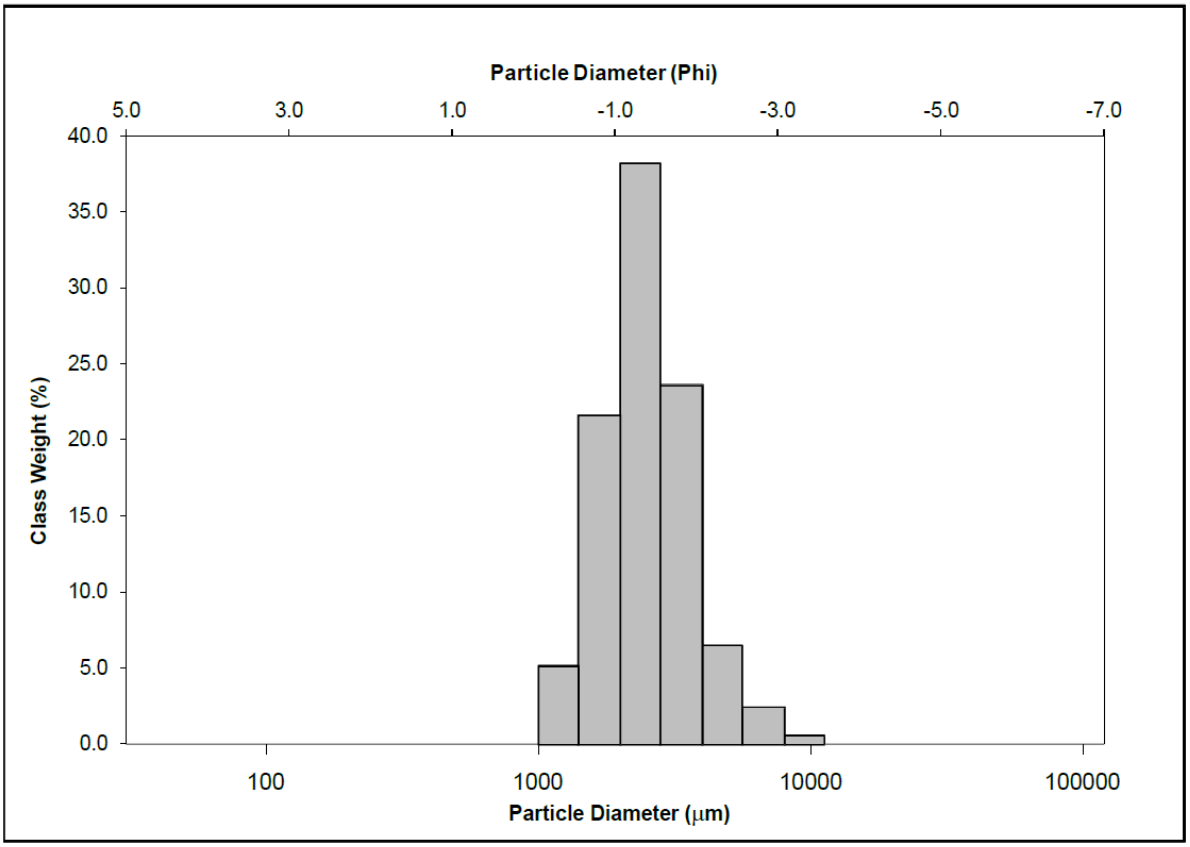

Figure 6.8: Carraroe grain size statistics.

SIEVING ERROR: -0.1%

SAMPLE IDENTITY: **Aran Islands**

SAMPLE TYPE: Polymodal, Poorly Sorted TEXTURAL GROUP: Gravel

SEDIMENT NAME: Coarse Gravel

	μm		GRAIN SIZE DISTRIBUTION			
MODE 1:	26950.0	-4.731	GRAVEL:	81.1%	COARSE SAND:	0.0%
MODE 2:	13600.0	-3.743	SAND:	14.7%	MEDIUM SAND:	0.0%
MODE 3:	2400.0	-1.243	MUD:	4.2%	FINE SAND:	0.0%
D_{10}:	1335.8	-4.782			V FINE SAND:	0.0%
MEDIAN or D_{50}:	7087.4	-2.825	V COARSE GRAVEL:	0.0%	V COARSE SILT:	0.7%
D_{90}:	27516.9	-0.418	COARSE GRAVEL:	25.2%	COARSE SILT:	0.7%
(D_{90} / D_{10}):	20.60	0.087	MEDIUM GRAVEL:	21.3%	MEDIUM SILT:	0.7%
(D_{90} - D_{10}):	26181.0	4.364	FINE GRAVEL:	18.0%	FINE SILT:	0.7%
(D_{75} / D_{25}):	9.197	0.287	V FINE GRAVEL:	16.6%	V FINE SILT:	0.7%
(D_{75} - D_{25}):	20023.5	3.201	V COARSE SAND:	14.6%	CLAY:	0.7%

	METHOD OF MOMENTS			FOLK & WARD METHOD		
	Arithmetic μm	Geometric μm	Logarithmic	Geometric μm	Logarithmic	Description
MEAN ($\bar{x}$):	11315.0	5451.3	-2.447	6811.7	-2.768	Fine Gravel
SORTING	9989.0	5.591	2.483	3.235	1.694	Poorly Sorted
SKEWNESS (Sk):	0.632	-2.191	2.191	-0.096	0.096	Symmetrical
KURTOSIS (K):	1.830	9.113	9.113	0.618	0.618	Very Platykurtic

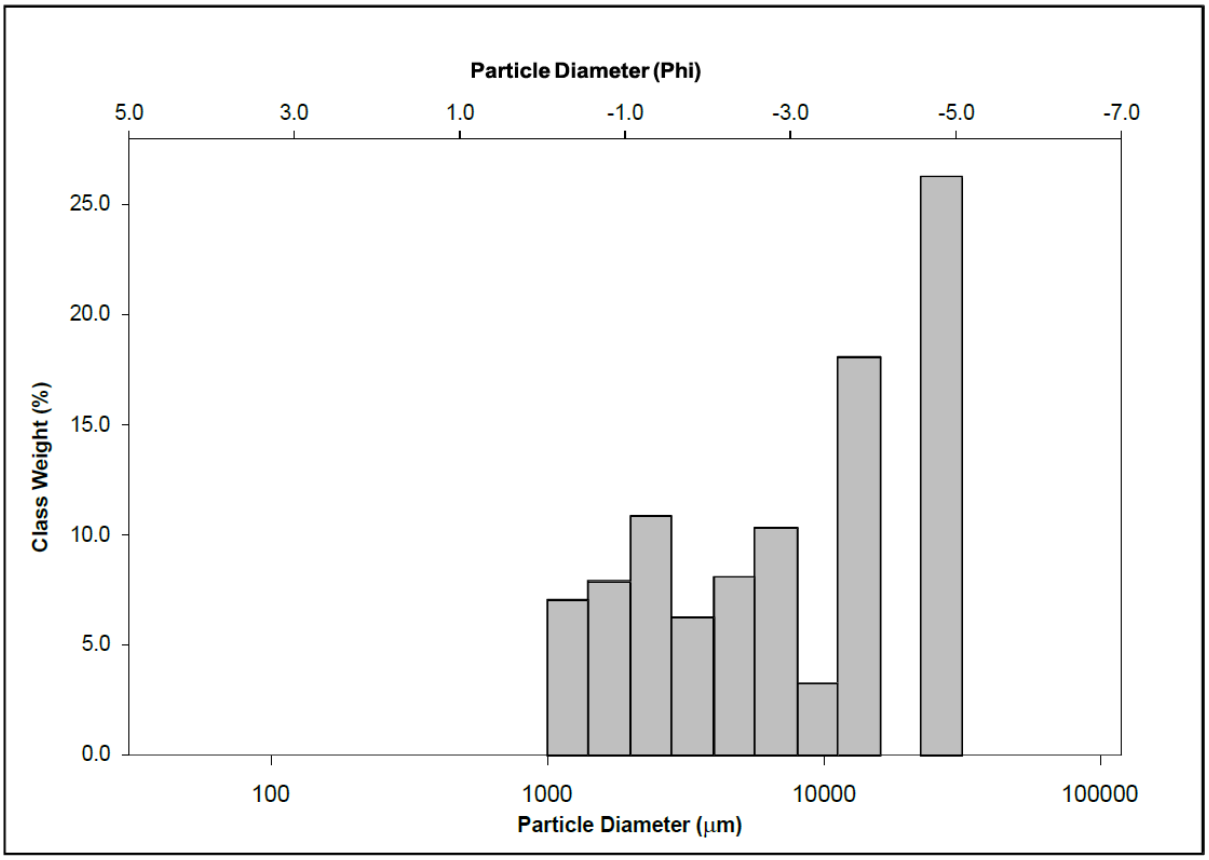

Figure 6.9: Aran grain size statistics.

SIEVING ERROR: 0.3%

SAMPLE IDENTITY: **Muckinish**

SAMPLE TYPE: Unimodal, Moderately Well Sorted TEXTURAL GROUP: Gravel

SEDIMENT NAME: Fine Gravel

	μm		GRAIN SIZE DISTRIBUTION	
MODE 1:	4800.0	-2.243	GRAVEL: 94.9%	COARSE SAND: 0.0%
MODE 2:			SAND: 4.3%	MEDIUM SAND: 0.0%
MODE 3:			MUD: 0.7%	FINE SAND: 0.0%
D_{10}:	2326.5	-2.926		V FINE SAND: 0.0%
MEDIAN or D_{50}:	4654.9	-2.219	V COARSE GRAVEL: 0.0%	V COARSE SILT: 0.1%
D_{90}:	7601.5	-1.218	COARSE GRAVEL: 0.0%	COARSE SILT: 0.1%
(D_{90} / D_{10}):	3.267	0.416	MEDIUM GRAVEL: 5.9%	MEDIUM SILT: 0.1%
(D_{90} - D_{10}):	5275.0	1.708	FINE GRAVEL: 56.9%	FINE SILT: 0.1%
(D_{75} / D_{25}):	1.932	0.642	V FINE GRAVEL: 32.1%	V FINE SILT: 0.1%
(D_{75} - D_{25}):	3037.4	0.950	V COARSE SAND: 4.3%	CLAY: 0.1%

	METHOD OF MOMENTS			FOLK & WARD METHOD		
	Arithmetic μm	Geometric μm	Logarithmic	Geometric μm	Logarithmic	Description
MEAN ($\bar{x}$):	4919.9	4262.9	-2.092	4510.1	-2.173	Fine Gravel
SORTING	2036.4	2.003	1.002	1.569	0.650	Moderately Well Sorted
SKEWNESS (Sk):	0.356	-5.470	5.470	-0.140	0.140	Fine Skewed
KURTOSIS (K):	2.742	49.58	49.58	0.900	0.900	Platykurtic

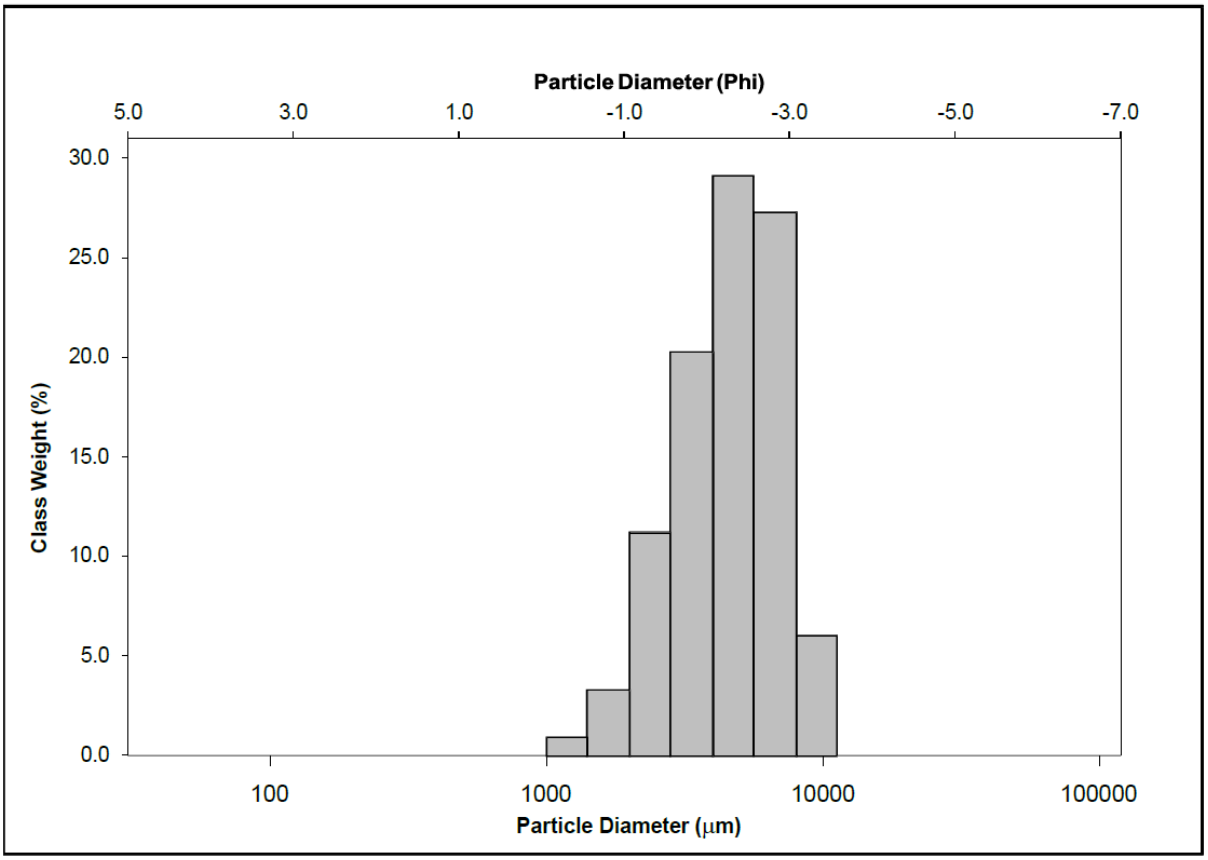

Figure 6.10: Muckinish grain size statistics.

6.2. Appendix 2- Paper 3

6.2.1. Tidal Information- Galway Bay

Datum of predictions are 0.20 cm below Ordinance Datum Dublin (Poolbeg).

Highest Astronomical Tide 17.43 GMT 29th September 2015 (5.74 metres)

Lowest Astronomical Tide 11.30 GMT 21st March 2015 (-0.16 metres)

Lunitidal Interval 4 hrs 51 minutes

Mean Sea Level 2.6 metres

Mean Range Springs 4.5 metres

Mean Range Neaps 1.9 metres

Mean High Water Springs (MHWS) 5.1 metres

Mean Low Water Springs (MLWS) 0.6 metres

Mean High Water Neaps (MHWN) 3.9 metres

Mean Low Water Neaps (MLWN) 2.0 metres

Tide Gauge Information Relating to Levels:

Chart datum Galway is OD Malin Head -2.91

Chart datum Galway is OD Poolbeg -0.2

The Highest Astronomical Tide (HAT) this century is in 2091, only 2mm higher than 2015.

Table 6.13: Date, time and levels of Highest Astronomical Tide in this century in Galway Bay.

Date of HAT	Time	HAT (m)
29/09/2015	17:43	5.74
09/10/2033	17:26	5.74
01/11/2073	05:36	5.74
12/11/2091	05:19	5.76

6.2.2. Computational Mesh

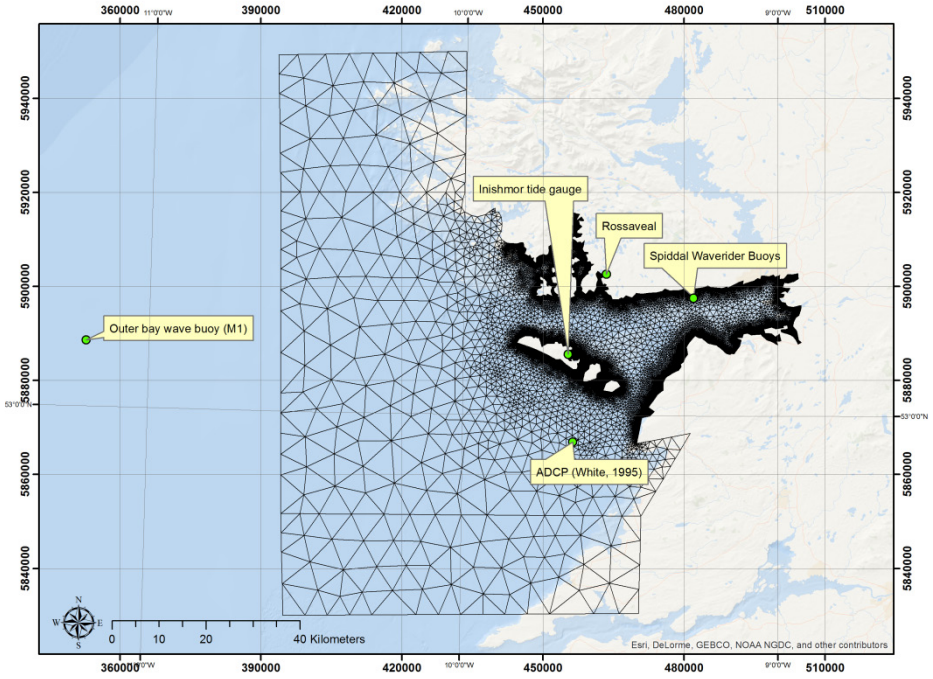

Figure 6.11: Galway Bay computational mesh with locations of ADCP, tide gauge and wave buoys.

6.3.3. Box Plots

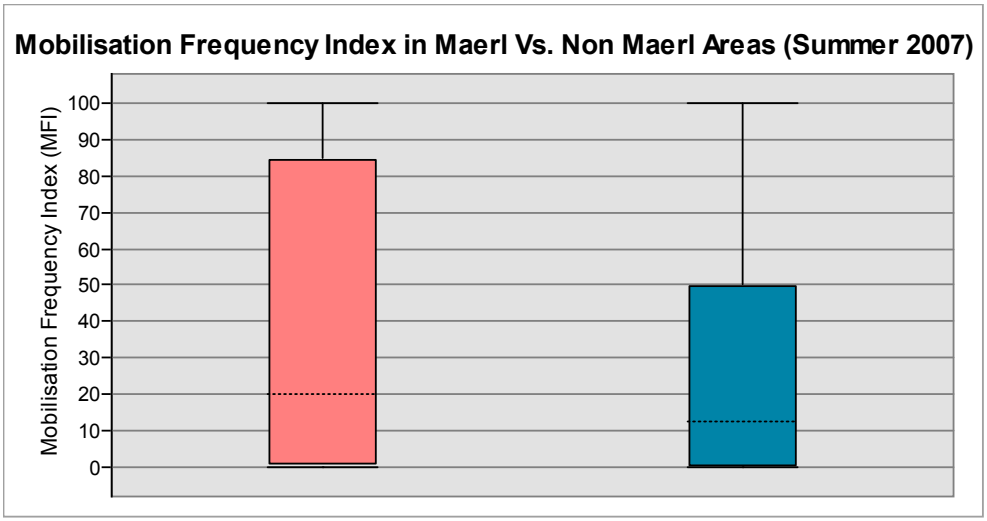

Figure 6.12: Box plot for Mobilisation Frequency Index in maerl and non-maerl areas in summer 2007.

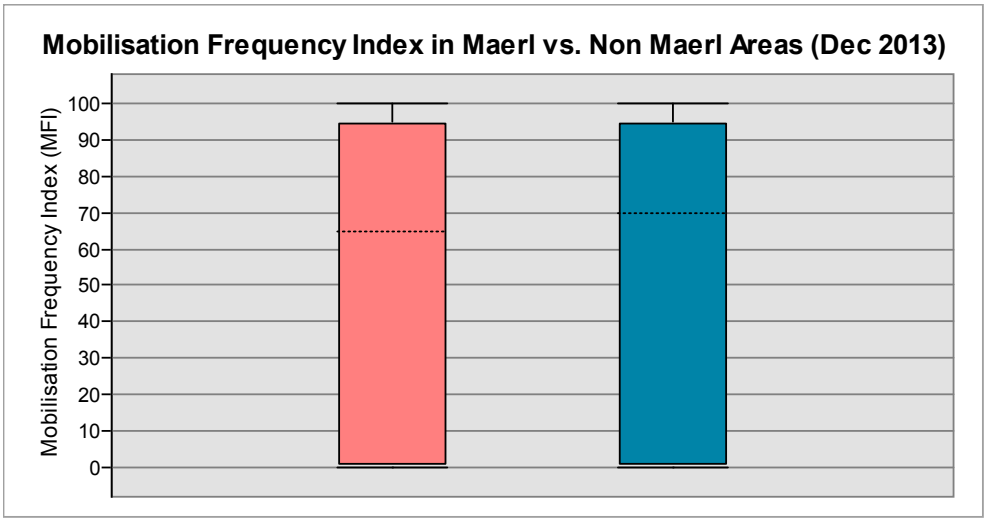

Figure 6.13: Box plot for Mobilisation Frequency Index in maerl and non-maerl areas in winter 2013.

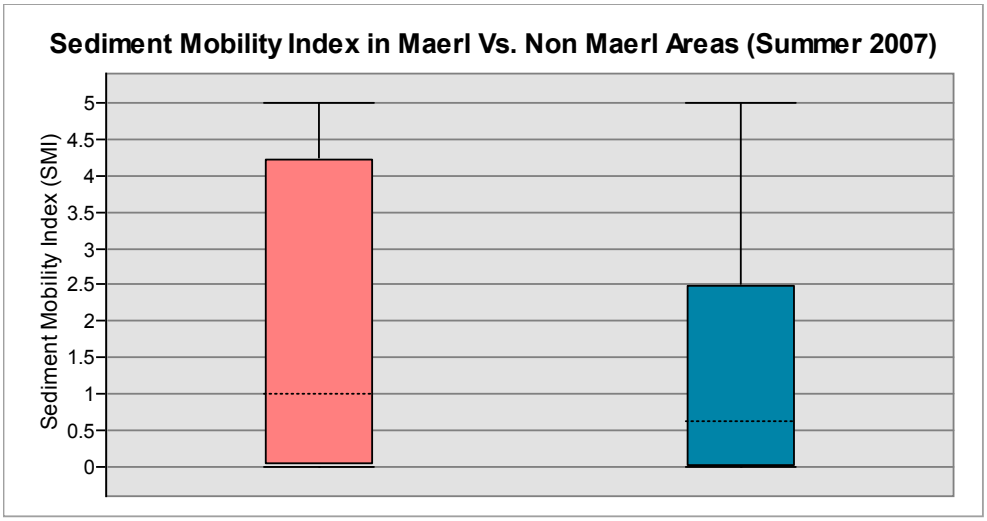

Figure 6.14: Box plot for Sediment Mobility Index in maerl and non-maerl areas in summer 2007.

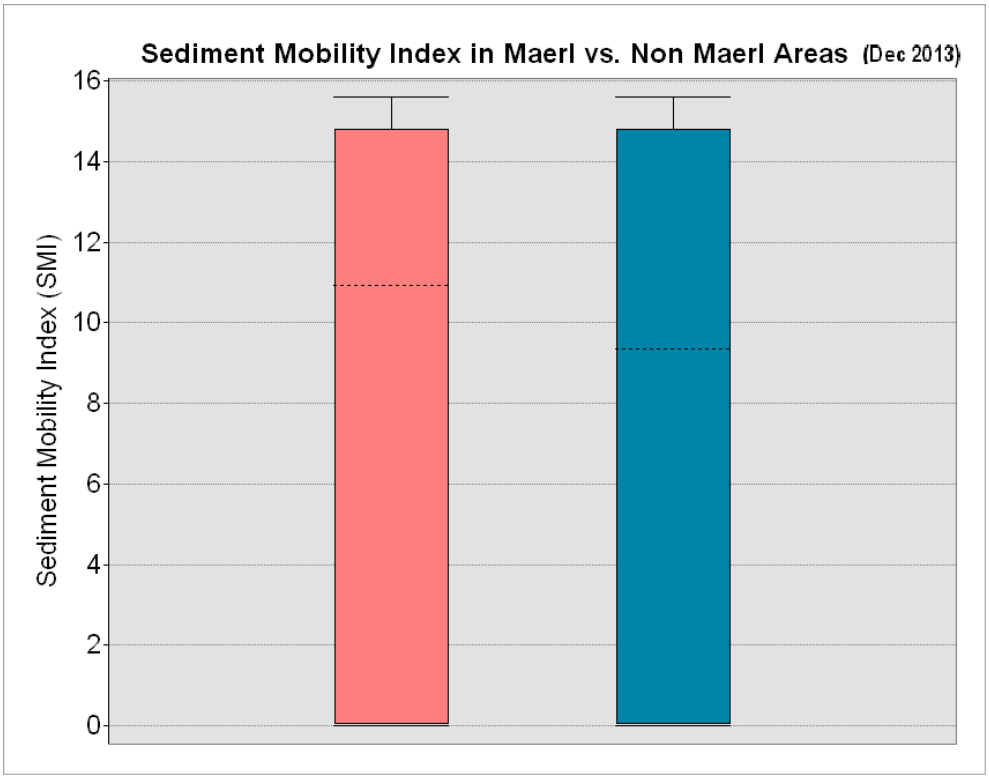

Figure 6.15: Box plot for Sediment Mobility Index in maerl and non-maerl areas in winter 2013.

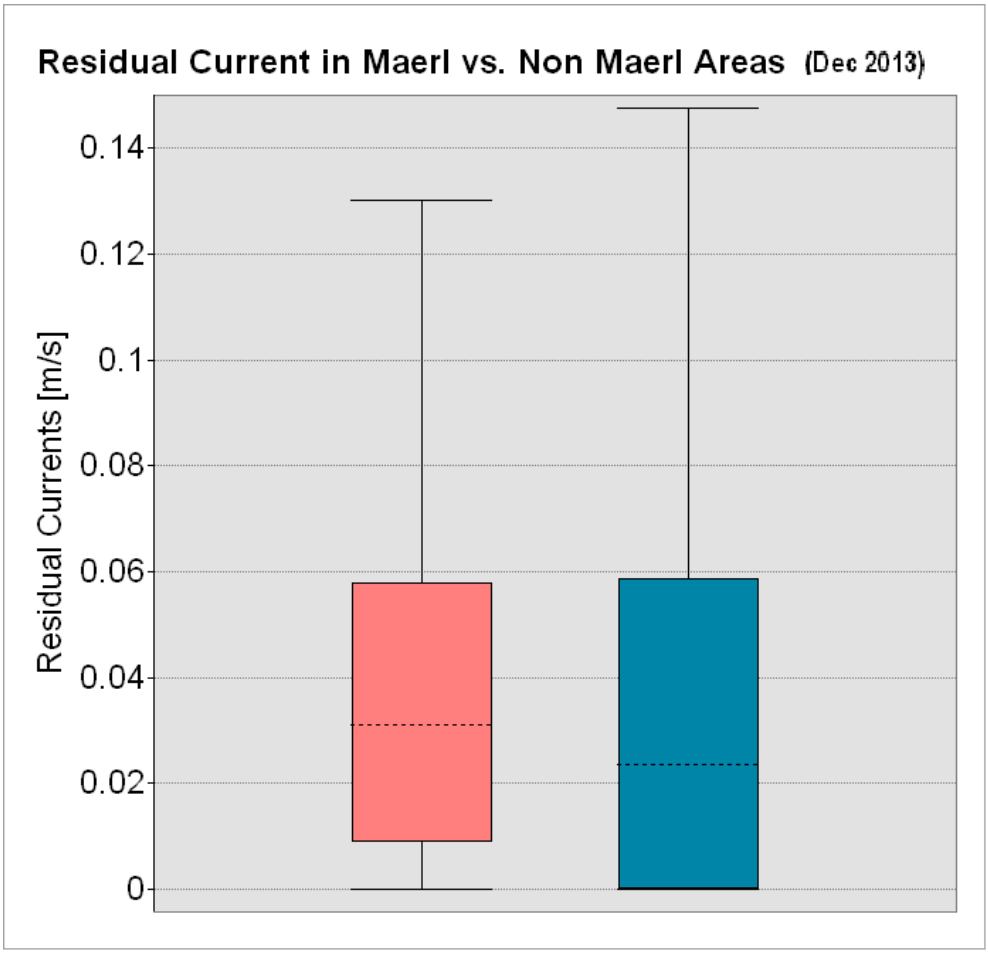

Figure 6.16: Box plot for residual currents in maerl and non-maerl areas in winter 2013.

6.3.4. Sensitivity Analysis

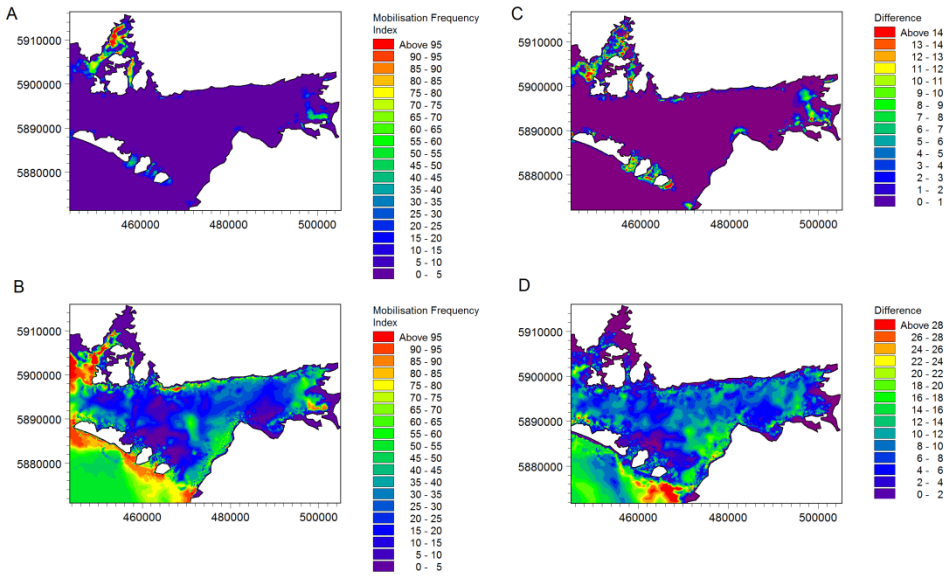

Figure 6.17: Sensitivity results of MFI in 2007 showing the upper bound (MFI + 20% current speed, significant wave height and wave period) for pure currents (A), combined wave currents (B) and the corresponding difference in MFI in comparison to the final results (C and D). Note the difference in combined wave-current situation is greatest in D just south of Inisheer, where there is the highest uncertainty in the final MFI, likely due to the largest significant wave heights.

Table 6.14: The mean and standard deviation of the differences of sediment mobility indices in summer 2007 and upper bound as a result of the sensitivity analysis introducing 20% errors in hydrodynamic parameters.

	MFI Current difference (%)	MFI Combined wave current difference (%)	SMI Difference
Mean	2.18	8.79	1.52
Standard Deviation	4.73	8.21	0.83

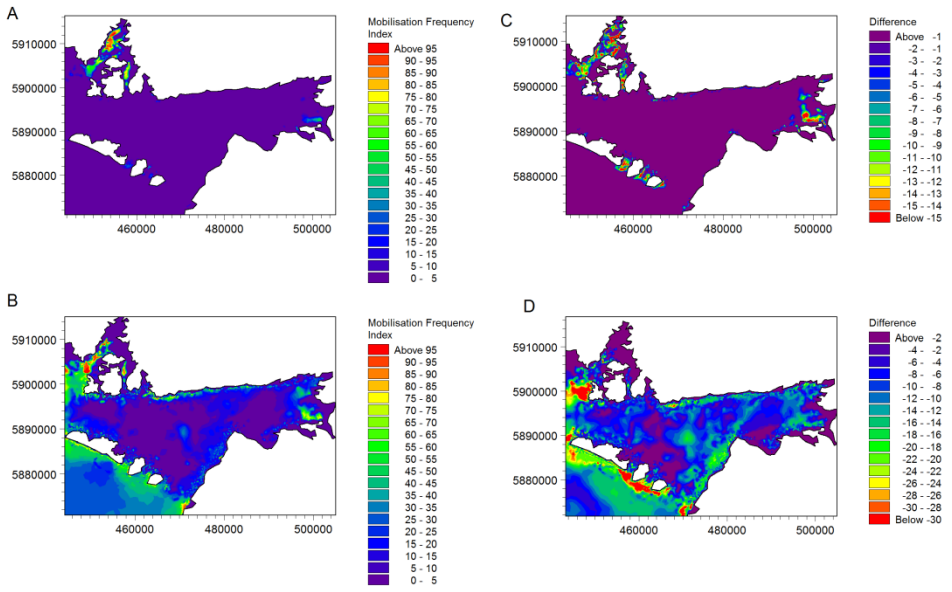

Figure 6.18: Sensitivity results of MFI in 2007 showing the lower bound (MFI - 20% current speed, significant wave height and wave period) for pure currents (A), combined wave currents (B) and the corresponding difference in MFI in comparison to the final results (C and D). Note the difference in combined wave-current situation is greatest in D just west of the Aran Island, where there is the highest uncertainty in the final MFI.

Table 6.15: The mean and standard deviation of the differences of sediment mobility indices in summer 2007 and lower bound as a result of the sensitivity analysis introducing 20% errors in hydrodynamic parameters.

	MFI Current difference (%)	MFI Combined wave current difference (%)	SMI Difference
Mean	-1.95	-13.33	-1.22
Standard Deviation	4.96	10.53	0.84

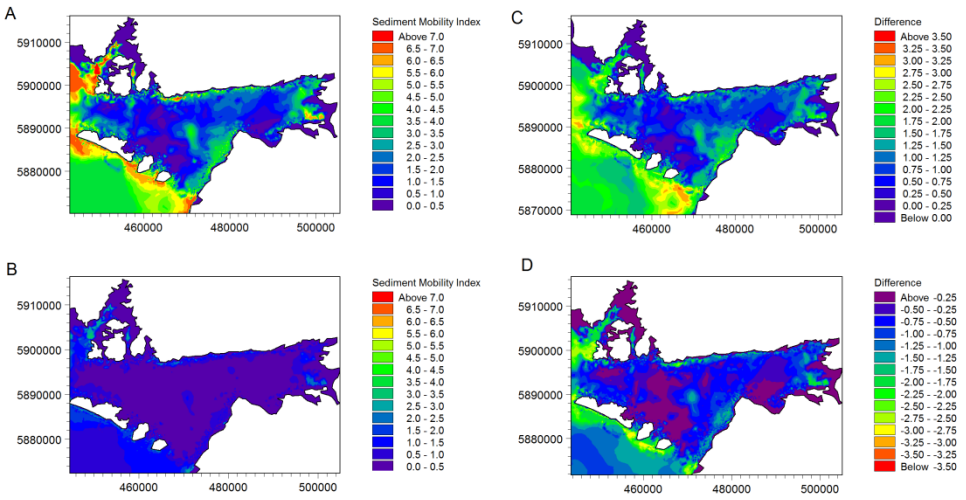

Figure 6.19: Sensitivity results of SMI in 2007 showing the upper and lower bounds (SMI ± 20% current speed, significant wave height and wave period) for combined wave-currents upper bound (A), combined wave-currents lower bound (B) and the corresponding difference in SMI in comparison to the final results (C and D).

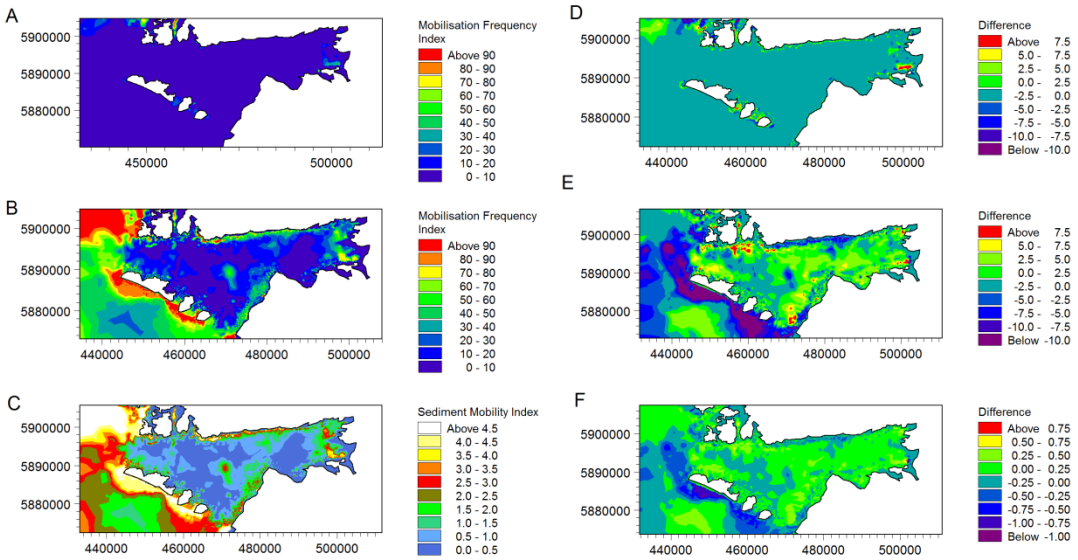

Figure 6.20: Sensitivity results for choice of time interval (10 equal interval time steps in a spring neap cycle) in the sediment mobility calculation. Mobilization Frequency Index (MFI) due to currents (A) and combined wave-currents (B) over the spring-neap cycle in summer 2007, and Sediment Mobility Index (C), with corresponding differences with the final results which used 20 timesteps (D, E and F).

Table 6.16: The mean and standard deviation of the differences as a result of the sensitivity analysis of time interval on sediment mobility indices in summer 2007.

	MFI Current difference (%)	MFI Combined wave current difference (%)	SMI Difference
Mean	-0.27	-2.27	-0.04
Standard Deviation	2.84	7.29	0.34

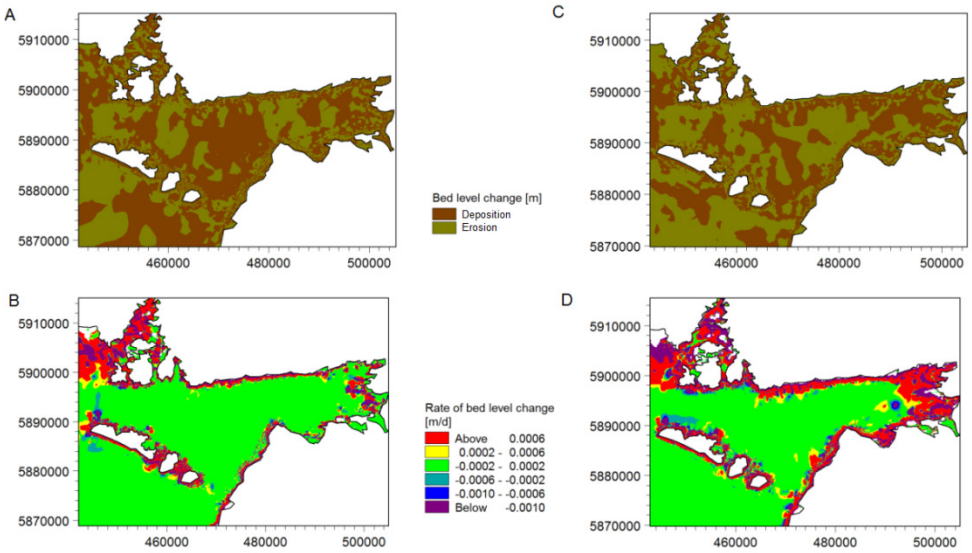

Figure 6.21: Sediment transport model results for quartz with critical shields parameter of 0.06 density 2650 kg m^{-3}. Bed level change shows zones of deposition or erosion in summer 2007 (A) and winter 2013 (C) and Rate of Bed level change in summer 2007 (B) and winter 2013 (D). Results show larger zone of deposition in centre of the bay and smaller zone of erosion, and lower sediment transport rates than maerl due to a higher critical bed shear stress and density of quartz than that of maerl.

7. References

- Adey, W., H., Mc Kibbin, D.L., 1970. Studies on the Maerl Species Phymatolithon calcareum (Pallas) nov. comb. and Lithothamnium coralloides (Crouan) in the Ria de Vigo, Botanica marina, p. 100.
- Adey, W., Halfar, J., Humphreys, A., Suskiewicz, T., Belanger, D., Gagnon, P., Fox, M., 2015. Sub-Arctic Rhodolith Beds Promote Longevity of Crustose Coralline Algal Buildups and their climate archiving potential. PALAIOS 30, 281-293.
- Adey, W.H., Vassar, J.M., 1975. Colonization, succession and growth rates of tropical crustose coralline algae (Rhodophyta, Cryptonemiales). Phycologia 14, 55-69.
- Admiralty, 2015. Galway Bay Tidal Information. The Hydrographer of the Navy, Taunton, Somerset, U.K.
- Aguirre, J., Braga, J.C., Bassi, D., 2017. Rhodoliths and Rhodolith Beds in the Rock Record, in: Riosmena-Rodríguez, R., Nelson, W., Aguirre, J. (Eds.), Rhodolith/Maërl Beds: A Global Perspective. Springer, Boca Raton, pp. 105-138.
- Alcerreca, J.C., Silva, R., Mendoza, E., 2013. Simple settling velocity formula for calcareous sand. Journal of Hydraulic Research 51, 215-219.
- Allen, J.R.L., 1985. Principles of physical sedimentology. The Netherlands, 272pp.
- Amado-Filho, G.M., Moura, R.L., Bastos, A.C., Salgado, L.T., Sumida, P.Y., Guth, A.Z., Francini-Filho, R.B., Pereira-Filho, G.H., Abrantes, D.P., Brasileiro, P.S., Bahia, R.G., Leal, R.N., Kaufman, L., Kleypas, J.A., Farina, M., Thompson, F.L., 2012. Rhodolith Beds Are Major CaCO3 Bio-Factories in the Tropical South West Atlantic. PLoS ONE 7, e35171.
- ANZECC TFMPA 1999. Strategic Plan of Action for the National Representative System of Marine Protected Areas: A Guide for Action by Australian Governments. Australian and New Zealand Environment and Conservation Council Task Force on Marine Protected Areas. Environment Australia, Canberra.
- Ashley, G.M., 1990. Classification of large-scale subaqueous bedforms; a new look at an old problem. Journal of Sedimentary Research 60, 160-172.
- Ayata, S.-D., Ellien, C., Dumas, F., Dubois, S., Thiébaut, É., 2009. Modelling larval dispersal and settlement of the reef-building polychaete Sabellaria alveolata: Role of hydroclimatic processes on the sustainability of biogenic reefs. Continental Shelf Research 29, 1605-1623.
- Barberá, C., Bordehore, C., Borg, J.A., Glémarec, M., Grall, J., Hall-spencer, J.M., De La Huz, C., Lanfranco, E., Lastra, M., Moore, P.G., Mora, J., Pita, M.E., Ramos-Espla, A.A., Rizzo, M., Sanchez-Mata, A., Seva, A., Schembri, P.J., Valle, C., 2003. Conservation and management of northeast Atlantic and Mediterranean maerl beds. Aquatic Conservation: Marine and Freshwater Ecosystems 13, S65.

- Basco, D.R., Coleman, R.A., Center, C.E.R., 1982. Surf zone currents / prepared for U.S. Army, Corps of Engineers, Coastal Engineering Research Center. National Technical Information Service, Operations Division [distributor], Fort Belvoir, VA. USA.
- Bassi, D., Iryu, Y., Nebelsick, J.H., 2012. To be or not to be a fossil rhodolith? Analytical methods for studying fossil rhodolith deposits. Journal of Coastal Research 28, 288-295.
- Basso, D., 1998. Deep rhodolith distribution in the Pontian Islands, Italy: a model for the paleoecology of a temperate sea. Palaeogeography, Palaeoclimatology, Palaeoecology 137, 173-187.
- Basso, D., Babbini, L., Kaleb, S., Bracchi, V.A., Falace, A., 2015. Monitoring deep Mediterranean rhodolith beds. Aquatic Conservation: Marine and Freshwater Ecosystems doi: 10.1002/aqc.2586.
- Bever, A.J., MacWilliams, M.L., 2013. Simulating sediment transport processes in San Pablo Bay using coupled hydrodynamic, wave, and sediment transport models. Marine Geology 345, 235-253.
- BIOMAERL, 1999. BIOMAERL Final Report, Coordinator: P.G. Moore, University Marine Biological Station Millport, Scotland EC Contract no. MAS3-CT95-0020, p. 973.
- Birkett, D.A., Maggs, C.A., Dring, M.J., 1998. Maerl, Volume V: An Overview of Dynamic and Sensitivity Characteristics for Conservation Management of Marine SACs, U.K. Marine SACs Project Scottish Association for Marine Science, Scotland, p. 116.
- Biron, P.M., Lane, S.N., Roy, A.G., Bradbrook, K.F., Richards, K.S., 1998. Sensitivity of bed shear stress estimated from vertical velocity profiles: the problem of sampling resolution. Earth Surface Processes and Landforms 23, 133-139.
- Biron, P.M., Robson, C., Lapointe, M.F., Gaskin, S.J., 2004. Comparing different methods of bed shear stress estimates in simple and complex flow fields. Earth Surface Processes and Landforms 29, 1403-1415.
- Blott, S.J., Pye, K., 2008. Particle shape: A review and new methods of characterization and classification. Sedimentology 55, 31-63.
- Bolaños, R., Tornfeldt Sørensen, J.V., Benetazzo, A., Carniel, S., Sclavo, M., 2014. Modelling ocean currents in the northern Adriatic Sea. Continental Shelf Research 87, 54-72.
- Booij, R., 1994. Measurements of the flow field in a rotating annular flume. Hydraulic and Geotechnical Engineering Division, Faculty of Civil Engineering, Delft University of Technology, The Netherlands, p. 180.
- Booth, D., 1975. The water structure and circulation of Killary Harbour and of Galway Bay. MSc Thesis, Oceanography. University College Galway, Galway, p. 112pp.
- Bosboom, J., Stive, M., 2013. Coastal Dynamics 1. Delft Academic Press (VSSD), The Netherlands, 573pp.

- Bosence, D., Wilson, J., 2003. Maerl growth, carbonate production rates and accumulation rates in the ne atlantic. Aquatic Conservation: Marine and Freshwater Ecosystems 13, S21-S31.
- Bosence, D.W.J., 1976. Ecological studies on two unattached coralline algae from Western Ireland. Palaeontology 19 (2), 365–395.
- Bosence, D.W.J., 1980. Sedimentary facies, production rates and facies models for recent coralline algal gravels, Co. Galway, Ireland. Geological Journal 15, 91-111.
- Bosence, D.W.J., 1983. The occurrence and ecology of recent rhodoliths - A review, in: Peryt, T. (Ed.), Coated Grains. Springer-Verlag, Berlin pp. 225-242.
- Bowden, K.F., Fairbairn, L.A., 1956. Measurements of Turbulent Fluctuations and Reynolds Stresses in a Tidal Current. Proceedings of the Royal Society of London A: Mathematical, Physical and Engineering Sciences 237, 422-438.
- Brodie, J., Williamson, C.J., Smale, D.A., Kamenos, N.A., Mieszkowska, N., Santos, R., Cunliffe, M., Steinke, M., Yesson, C., Anderson, K.M., Asnaghi, V., Brownlee, C., Burdett, H.L., Burrows, M.T., Collins, S., Donohue, P.J.C., Harvey, B., Foggo, A., Noisette, F., Nunes, J., Ragazzola, F., Raven, J.A., Schmidt, D.N., Suggett, D., Teichberg, M., Hall-Spencer, J.M., 2014. The future of the northeast Atlantic benthic flora in a high CO2 world. Ecology and Evolution 4, 2787-2798.
- Brown, J.M., Wolf, J., 2009. Coupled wave and surge modelling for the eastern Irish Sea and implications for model wind-stress. Continental Shelf Research 29, 1329-1342.
- Bucher, D.J., Harriott, V.J., Roberts, L.G., 1998. Skeletal micro-density, porosity and bulk density of acroporid corals. Journal of Experimental Marine Biology and Ecology 228, 117-136.
- Buffington, J., 1999. The Legend of A. F. Shields. Journal of Hydraulic Engineering 125, 376-387.
- Buffington, J.M., Montgomery, D.R., 1997. A systematic analysis of eight decades of incipient motion studies, with special reference to gravel-bedded rivers. Water Resources Research 33, 1993-2029.
- Burgess, C.J., Anderson, J.M., 1983. Rhodoids in Temperate Carbonates from the Cenozoic of New Zealand, in: Peryt, T. (Ed.), Coated Grains. Springer Verlag, Berlin, pp. 243-258.
- Burrows, M.T., Kamenos, N.A., Hughes, D.J., Stahl, H., Howe, J.A., Tett, P., 2014. Assessment of carbon budgets and potential blue carbon stores in Scotland's coastal and marine environment. , Scottish Natural Heritage Commissioned Report No. 761., Edinburgh, p. 90pp.
- Cabioch, J., 1969. Les fonds de maerl de la baie de Morlaix et leur peuplement végétal. Cahiers de biologie marine 10 139 - 161.
- Campos, R.H.S., Dominguez, J.M.L., 2010. Mobility of sediments due to wave action on the continental shelf of the Northern coast of the state of Bahia. Brazilian Journal of Oceanography 58, 57-63.

- CBD, 2016. Convention on Biological Diversity EBSA Website [https://www.cbd.int/ebsa/] Last Accessed: 5th April 2016.
- Celtic Sea Minerals Ltd, 2016. Available at [http://www.celticseaminerals.com/] Last Accessed: 9th October 2016.
- Chadwick, A., Morfett, J., Borthwick, M., 2013. Hydraulics in Civil and Environmental Engineering, Fifth Edition. Taylor & Francis. , Boca Raton, 648pp.
- Cheng, N.S., 1997. Simplified settling velocity formula for sediment particle. Journal of Hydraulic Engineering 123, 149-152.
- Coletti, G., Basso, D., Frixa, A., Corselli, C., 2015. Transported Rhodoliths witness the lost Carbonate factory: a case history from the Miocene Pietra da Cantoni limestone (NW Italy). Rivista Italiana di Paleontologia e Stratigrafia 121:3.
- D'agostini, D.P., Bastos, A.C., Dos Reis, A.T., 2015. The Modern Mixed Carbonate–Siliciclastic Abrolhos Shelf: Implications For A Mixed Depositional Model. Journal of Sedimentary Research 85, 124-139.
- Dalyander, P.S., Butman, B., Sherwood, C.R., Signell, R.P., Wilkin, J.L., 2013. Characterizing wave- and current- induced bottom shear stress: U.S. middle Atlantic continental shelf. Continental Shelf Research 52, 73-86.
- Day, T.J., 1980. A study of the transport of graded sediments. Hydraulics Research Station Technical Report No. IT190, Wallingford, 10pp.
- De Falco, G., De Muro, S., Batzella, T., Cucco, A., 2011. Carbonate sedimentation and hydrodynamic pattern on a modern temperate shelf: The strait of Bonifacio (western Mediterranean). Estuarine, Coastal and Shelf Science 93, 14-26.
- De Grave, S., 1999. The Influence of Sedimentary Heterogeneity on Within Maerl Bed Differences in Infaunal Crustacean Community. Estuarine, Coastal and Shelf Science 49, 153-163.
- De Grave, S., Fazakerley, H., Kelly, L., Guiry, M.D., Ryan, M., Walshe, J., 2000. A study of selected maërl beds in Irish waters and their potential for sustainable extraction., The Marine Institute, Dublin, p. 44.
- De Grave, S., Whitaker, A., 1999. A census of maerl beds in Irish waters. Aquatic Conservation: Marine and Freshwater Ecosystems 9, 303-311.
- De Wit, P.J., 1992. Instruments used in the research on cohesive sediments, Report 8-92. Department of Civil Engineering, Delft University of Technology, Netherlands p. 98pp.
- Dean, W., Dalrymple, R., 2002. Coastal Processes With Engineering Applications. Cambridge University Press. Cambridge. 489pp.
- DHI, 2016. MIKE by DHI. DHI, Denmark.
- Dietrich, W.E., 1982. Settling velocity of natural particles. Water Resources Research 18, 1615-1626.
- Dyer, K.R., 1986. Coastal and Estuarine Sediment Dynamics. John Wiley & Sons Ltd. Chichester. 358pp.

- Egiazaroff, I.V., 1965. Calculation of Nonuniform Sediment Concentration. Journal of Hydraulic Engineering, 91, 225–247.
- Elsäßer, B., Fariñas-Franco, J.M., Wilson, C.D., Kregting, L., Roberts, D., 2013. Identifying optimal sites for natural recovery and restoration of impacted biogenic habitats in a special area of conservation using hydrodynamic and habitat suitability modelling. Journal of Sea Research 77, 11-21.
- Fenton, J.D., Abbott, J.E., 1977. Initial Movement of Grains on a Stream Bed: The Effect of Relative Protrusion. Proceedings of the Royal Society of London. A. Mathematical and Physical Sciences 352, 523-537.
- Fenton, J.D., McKee, W.D., 1990. On calculating the lengths of water waves. Coastal Engineering 14, 499-513.
- Ferguson, R.I., Church, M., 2004. A simple universal equation for grain settling velocity. Journal of Sedimentary Research 74, 933-937.
- Fernandes, L., 1988. A study of the oceanography of Galway Bay, mid-western coastal waters (Galway Bay to Tralee Bay), Shannon Estuary and the River Shannon plume. PhD thesis. University College Galway. 229pp.
- Flannery, W., 2011. Marine spatial planning from an Irish perspective: towards best practice in integrated maritime governance, School of Geography and Archaeology. PhD thesis. National University of Ireland, Galway, Ireland. 188pp.
- Folk, R.L., Robles, R., 1964. Carbonate Sands of Isla Perez, Alacran Reef Complex, Yucaten. The Journal of Geology 72, 255-292.
- Foster, M.S., 2001. Rhodoliths: Between rocks and soft places. Journal of Phycology 37, 659-667.
- Fredsøe, J., 1984. Turbulent Boundary Layer in Wave-current Motion. Journal of Hydraulic Engineering 110, 1103-1120.
- Fredsøe, J., Deigaard, R., 1992. Mechanics of Coastal Sediment Transport. World Scientific, New Jersey, 369pp.
- Gherardi, D.F.M., Bosence, D.W.J., 1999. Modeling of the Ecological Succession of Encrusting Organisms in Recent Coralline-Algal Frameworks from Atol Das Rocas, Brazil. PALAIOS 14, 145-158.
- Gibbs, R.J., 1972. The accuracy of particle-size analysis utilizing settling tubes. Journal of Sedimentary Petrology 42, 141-145.
- Goring, D.G., Nikora, V.I., 2002. Despiking Acoustic Doppler Velocimeter Data. Journal of Hydraulic Engineering 128, 117-126.
- Grall, J., Glemarec, M., 1997. Biodiversite des fonds de maerl en Bretagne: approche fonctionnelle et impacts anthropiques. Vie et Milieu 47(4), 339-349.
- Grall, J., Hall-Spencer, J.M., 2003. Problems facing maerl conservation in Brittany. Aquatic Conservation: Marine and Freshwater Ecosystems 13, S55-S64.
- Griffin, J.D., Hemer, M.A., Jones, B.G., 2008. Mobility of sediment grain size distributions on a wave dominated continental shelf, southeastern Australia. Marine Geology 252, 13-23.

- Guisan, A., Zimmermann, N.E., 2000. Predictive habitat distribution models in ecology. Ecological Modelling 135, 147-186.
- Hall-Spencer, J., 1998. Conservation issues relating to maerl beds as habitats for molluscs. Journal of Conchology 36, 271-286.
- Hall-Spencer, J., 2005. Ban on maerl extraction, News. Marine Pollution Bulletin 50, 121-124.
- Hall-Spencer, J., Kelly, J., Maggs, C., 2008. Assessment of maerl beds in the OSPAR area and the development of a monitoring program, Unpublished report available at [https://www.npws.ie/sites/default/files/publications/pdf/Hall-Spencer_et_al_2008_OSPAR_maerl.pdf] 34pp.
- Hall-Spencer, J., White, N., Gillespie, E., Gillham, K., Foggo, A., 2006. Impact of fish farms on maerl beds in strongly tidal areas. Marine Ecology Progress Series 326, 1-9.
- Hall-Spencer, J.M., 1994. Biological studies on nongeniculate Corallinaceae, PhD thesis. University of London, UK, 269pp.
- Hall-Spencer, J.M., 1995. The effects of scallop dredging on maerl beds in the Firth of Clyde. Porcupine Newsletter 6 (1), 16-27.
- Hall-Spencer, J.M., Atkinson, R.J.A., 1999. Upogebia deltaura (Crustacea: Thalassinidea) in Clyde Sea maerl beds, Scotland. Journal of the Marine Biological Association of the United Kingdom 79, 871-880.
- Hall-Spencer, J.M., Grall, J., Moore, P.G., Atkinson, R.J.A., 2003. Bivalve fishing and maerl-bed conservation in France and the UK—retrospect and prospect. Aquatic Conservation: Marine and Freshwater Ecosystems 13, S33-S41.
- Hall-Spencer, J.M., Kelly, J., Maggs, C.A., 2010. Background document for maerl beds. OSPAR Commission, London, Publication 491/2010, ISBN 978-1-907390-32-6, p. 36
- Hall-Spencer, J.M., Moore, P.G., 2000. Scallop dredging has profound, long-term impacts on maerl habitats. ICES Journal of Marine Science: Journal du Conseil 57, 1407-1415.
- Hallermeier, R.J., 1981. Terminal settling velocity of commonly occurring sand grains. Sedimentology 28, 859-865.
- Harris, P.T., 2012a. Biogeography, Benthic Ecology, and Habitat Classification Schemes, in: Harris, P.T., Baker, E.K. (Eds.), Seafloor geomorphology as benthic habitat GeoHAB Atlas of Seafloor Geomorphic Features and Benthic Habitats. Elsevier Insights, London, pp. 61-91.
- Harris, P.T., 2012b. On Seabed Disturbance, Marine Ecological Succession and Applications for Environmental Management: A Physical Sedimentological Perspective, in: Li, M.Z., Sherwood, C.R., Hill, P.R. (Eds.), Sediments, Morphology and Sedimentary Processes on Continental Shelves: Advances in Technologies, Research, and Applications John Wiley & Sons, Ltd, Chichester, pp. 387-404.
- Harris, P.T., 2012c. Surrogacy, in: Harris, P.T., Baker, E.K. (Eds.), Seafloor geomorphology as benthic habitat GeoHAB Atlas of

Seafloor Geomorphic Features and Benthic Habitats. Elsevier Insights, London, pp. 93-108.
- Harris, P.T., Coleman, R., 1998. Estimating global shelf sediment mobility due to swell waves. Marine Geology 150, 171-177.
- Harris, P.T., Hughes, M.G., 2012. Predicted benthic disturbance regimes on the Australian continental shelf: a modelling approach. Marine Ecology Progress Series 449, 13-25.
- Harris, P.T., Tsuji, Y., Marshall, J.F., Davies, P.J., Honda, N., Matsuda, H., 1996. Sand and rhodolith-gravel entrainment on the mid- to outer-shelf under a western boundary current: Fraser Island continental shelf, eastern Australia. Marine Geology 129, 313-330.
- Heathershaw, A.D., Thorne, P.D., 1985. Sea-bed noises reveal role of turbulent bursting phenomenon in sediment transport by tidal currents. Nature 316, 339-342.
- Hemer, M.A., 2006. The magnitude and frequency of combined flow bed shear stress as a measure of exposure on the Australian continental shelf. Continental Shelf Research 26, 1258-1280.
- Hinojosa-Arango, G., Maggs, C.A., Johnson, M.P., 2009. Like a Rolling Stone: The Mobility of Maerl (Corallinaceae) and the Neutrality of the Associated Assemblages. Ecology 90, 517-528.
- Hoeke, R.K., Storlazzi, C.D., Ridd, P.V., 2013. Drivers of circulation in a fringing coral reef embayment: A wave-flow coupled numerical modeling study of Hanalei Bay, Hawaii. Continental Shelf Research 58, 79-95.
- Holthuijsen, L.H., Herman, A., Booij, N., 2003. Phase-decoupled refraction–diffraction for spectral wave models. Coastal Engineering 49, 291-305.
- Hughes, S.A., 1993. Physical Models and Laboratory Techniques in Coastal Engineering. World Scientific, Singapore. 568pp.
- Hurrell, J.W., Deser, C., 2009. North Atlantic climate variability: The role of the North Atlantic Oscillation. Journal of Marine Systems 78, 28-41.
- Idier, D., Romieu, E., Pedreros, R., Oliveros, C., 2010. A simple method to analyse non-cohesive sediment mobility in coastal environment. Continental Shelf Research 30, 365-377.
- INFOMAR, 2007. INFOMAR Survey Report: Leg CV07_01, Zone 1, Galway Bay, Geological Survey of Ireland.
- INFOMAR, 2016. [http://www.infomar.ie] Last Accessed: 5th April 2016.
- James, N.P., 1997. The Cool-Water Carbonate Depositional Realm, Cool-Water Carbonates. SEPM Society for Sedimentary Geology, pp. 1-20.
- Jamieson, E.C., Post, G., Rennie, C.D., 2010. Spatial variability of three-dimensional Reynolds stresses in a developing channel bend. Earth Surface Processes and Landforms 35, 1029-1043.
- Janke, N.C., 1966. Effect of shape upon the settling velocity of regular convex geometric particles. Journal of Sedimentary Petrology 36, 370-376.

- Johnson, M.E., Baarli, B.G., Cachão, M., da Silva, C.M., Ledesma-Vázquez, J., Mayoral, E.J., Ramalho, R.S., Santos, A., 2012. Rhodoliths, uniformitarianism, and Darwin: Pleistocene and Recent carbonate deposits in the Cape Verde and Canary archipelagos. Palaeogeography, Palaeoclimatology, Palaeoecology 329–330, 83-100.
- Johnson, M.P., Jessopp, M., Mulholland, O.R., McInerney, C., McAllen, R., Allcock, A.L., Crowe, T.P., 2008. What is the future for Marine Protected Areas in Irish waters? Biology and Environment: Proceedings of the Royal Irish Academy 108B, 9-15.
- Jones, O.P., Petersen, O.S., Kofoed-Hansen, H., 2007. Modelling of complex coastal environments: Some considerations for best practise. Coastal Engineering 54, 717-733.
- Joshi, S., Duffy, G.P., Brown, C., 2014. Settling Velocity and Grain Shape of Maërl Biogenic Gravel. Journal of Sedimentary Research 84, 718-727.
- Kamenos, N.A., Burdett, H.L., Aloisio, E., Findlay, H.S., Martin, S., Longbone, C., Dunn, J., Widdicombe, S., Calosi, P., 2013. Coralline algal structure is more sensitive to rate, rather than the magnitude, of ocean acidification. Global Change Biology 19, 3621-3628.
- Kamenos, N.A., Moore, P.G., Hall-Spencer, J.M., 2004a. Nursery-area function of maerl grounds for juvenile queen scallops Aequipecten opercularis and other invertebrates. Marine Ecology Progress Series 274, 183-189.
- Kamenos, N.A., Moore, P.G., Hall-Spencer, J.M., 2004b. Small-scale distribution of juvenile gadoids in shallow inshore waters; what role does maerl play? ICES Journal of Marine Science: Journal du Conseil 61, 422-429.
- Keegan, B., 1972. Benthic studies in Kilkieran Bay and in Galway Bay with particular reference to the Class Bivalvia, PhD thesis, Zoology. University College Galway, Ireland. 259pp.
- Keegan, B., 1974. The macrofauna of maerl substrates of the West coast of Ireland. Cahiers de biologie marine 15, 513–530.
- Keulegan, G.H., 1938. Laws of turbulent flow in open channels. Part of Journal of Research of the Rational Bureau of Standards, Volume 21, December 1938, U. S. Department of Commerce National Bureau of Standards, Research Paper RP1151, 35pp.
- Keylock, C.J., Nishimura, K., Peinke, J., 2012. A classification scheme for turbulence based on the velocity-intermittency structure with an application to near-wall flow and with implications for bed load transport. Journal of Geophysical Research: Earth Surface 117, F01037.
- Kim, S.-C., Friedrichs, C.T., Maa, J.P.-Y., Wright, L.D., 2000. Estimating Bottom Stress in Tidal Boundary Layer from Acoustic Doppler Velocimeter Data. Journal of Hydraulic Engineering 126, 399-406.
- Komar, P., 1974. Boundary layer flow under steady unidirectional currents in: Stanley, D.J., Swift, D.J.P. (Eds.), Marine Sediment

Transport and Environmental Management. John Wiley and Sons. Wiley Interscience, pp. 91-106.
- Komar, P.D., Reimers, C.E., 1978. Grain shape effects on settling rates. Journal of Geology 86, 193-209.
- Komen, G.J., Cavaleri, L., Donelan, M., Hasselmann, K., Hasselmann, S., Janssen, P.A.E.M., 1994. Dynamics and Modelling of Ocean Waves. Cambridge University Press.
- Kostylev, V.E., 2012. Benthic Habitat Mapping from Seabed Acoustic Surveys: Do Implicit Assumptions Hold?, Sediments, Morphology and Sedimentary Processes on Continental Shelves. John Wiley & Sons, Ltd, pp. 405-416.
- Kostylev, V.E., Hannah, C.G., 2007. Process-driven characterization and mapping of seabed habitats. Mapping the Seafloor for Habitat Characterization: Geological Association of Canada, Special Paper 47, 171-184.
- Kramer, H., 1935. Sand mixtures and sand movement in fluvial models. Transactions of American Society of Civil Engineering 100, 798-878.
- Le Roux, J.P., 2003. Wave friction factor as related to the Shields parameter for steady currents. Sedimentary Geology 155, 37-43.
- Lefebvre, A., 2009. Bed roughness over vegetated beds: sonar imaging techniques and effect on unidirectional currents, School of Ocean and Earth Sciences. University of Southampton, p. 212.
- Lei, W., 1995. Three dimensional hydrodynamic modelling in Galway Bay, PhD thesis, Oceanography. National University of Ireland, Galway, Galway, 185pp.
- Lemoine, M., 1910. Repartition et mode de vie du maerl (Lithothamnium calcareum) aux environs de Concarneau (Finistère) Annales de l'Institut Océanographique 1(3): 1-28.
- Li, M.Z., Hannah, C.G., Perrie, W.A., Tang, C.C.L., Prescott, R.H., Greenberg, D.A., 2015. Modelling Seabed Shear Stress, Sediment Mobility and Sediment Transport in the Bay of Fundy. Canadian Journal of Earth Sciences 52(9), 757-775.
- Littler, M.M., Littler, D.S., Blair, S.M., Norris, J.N., 1985. Deepest Known Plant Life Discovered on an Uncharted Seamount. Science 227, 57-59.
- Longuet-Higgins, M.S., Stewart, R.w., 1964. Radiation stresses in water waves; a physical discussion, with applications. Deep Sea Research and Oceanographic Abstracts 11, 529-562.
- Lordan, C., Doyle, J., Sacchetti, F., O'Driscoll, D., Heir, I., Smith, T., Allsop, C., 2007. Aran, Galway Bay and Slyne Head Nephrops Grounds 2006 UWTV Survey Report. Marine Institute Ireland. Available at: [http://hdl.handle.net/10793/305].
- Maggi, F., 2005. Flocculation dynamics of cohesive sediments, PhD thesis, Civil Engineering and Geosciences. Delft University of Technology (TU Delft), The Netherlands, 154pp.
- Maggs, C.A., 1983. A phenological study of the epiflora of two maerl beds in Galway Bay, Botany. University College Galway, Galway, p. 346.

- Malvern, 2013. Image analysis App Note MRK664-01, 4pp. Particle Size and Shape Measurement Using Image Analysis.
- Marrack, E.C., 1999. The relationship between water motion and living rhodolith beds in the southwestern Gulf of California, Mexico. PALAIOS 14, 159-171.
- Martin, C.S., Giannoulaki, M., De Leo, F., Scardi, M., Salomidi, M., Knitweiss, L., Pace, M.L., Garofalo, G., Gristina, M., Ballesteros, E., Bavestrello, G., Belluscio, A., Cebrian, E., Gerakaris, V., Pergent, G., Pergent-Martini, C., Schembri, P.J., Terribile, K., Rizzo, L., Ben Souissi, J., Bonacorsi, M., Guarnieri, G., Krzelj, M., Macic, V., Punzo, E., Valavanis, V., Fraschetti, S., 2014. Coralligenous and maërl habitats: Predictive modelling to identify their spatial distributions across the mediterranean sea. Scientific Reports 4, Article no. 5073, Nature Publications.
- Mason, C., 2011. NMBAQC's Best Practice Guidance. Particle Size Analysis (PSA) for Supporting Biological Analysis. . National Marine Biological AQC Coordinating Committee, p. 72.
- Masselink, G., Castelle, B., Scott, T., Dodet, G., Suanez, S., Jackson, D., Floc'h, F., 2016. Extreme wave activity during 2013/2014 winter and morphological impacts along the Atlantic coast of Europe. Geophysical Research Letters 43, 2015GL067492.
- Masselink, G., Hughes, M.G., Knight, J., 2011. Introduction to Coastal Processes and Geomorphology. Hodder Education, Oxon, 432pp.
- McCabe, A.M., 2008. Glacial geology and geomorphology: the landscapes of Ireland. Dunedin Academic Press, Edinburgh, 274pp.
- Mehta, A.J., Rao, P.V., 1985. Angle of Repose of Selected Bivalve Shell Beds. Journal of Coastal Research 1, 365-374.
- Melbourne, L.A., Griffin, J., Schmidt, D.N., Rayfield, E.J., 2015. Potential and limitations of finite element modelling in assessing structural integrity of coralline algae under future global change. Biogeosciences 12, 5871-5883.
- Met Éireann, 2016. [http://met.ie] Last Accessed: 05 April 2016.
- MI, 2016. Marine Institute Ireland [http://marine.ie] Last Accessed: 05 April 2016.
- Miller, R.L., Byrne, R.J., 1966. The angle of repose for a single grain on a fixed rough bed. Sedimentology 6, 303-314.
- Mitchell, A., 2001. An Investigation into the Maërl Bed Distribution off Swanage, MSc thesis, School of Ocean and Earth Science. University of Southampton, UK, p. 85.
- Mohn, C., Rengstorf, A., White, M., Duineveld, G., Mienis, F., Soetaert, K., Grehan, A., 2014. Linking benthic hydrodynamics and cold-water coral occurrences: A high-resolution model study at three cold-water coral provinces in the NE Atlantic. Progress in Oceanography 122, 92-104.
- Moura, R.L., Amado-Filho, G.M., Moraes, F.C., Brasileiro, P.S., Salomon, P.S., Mahiques, M.M., Bastos, A.C., Almeida, M.G., Silva, J.M., Araujo, B.F., Brito, F.P., Rangel, T.P., Oliveira, B.C.V., Bahia, R.G., Paranhos, R.P., Dias, R.J.S., Siegle, E., Figueiredo,

A.G., Pereira, R.C., Leal, C.V., Hajdu, E., Asp, N.E., Gregoracci, G.B., Neumann-Leitão, S., Yager, P.L., Francini-Filho, R.B., Fróes, A., Campeão, M., Silva, B.S., Moreira, A.P.B., Oliveira, L., Soares, A.C., Araujo, L., Oliveira, N.L., Teixeira, J.B., Valle, R.A.B., Thompson, C.C., Rezende, C.E., Thompson, F.L., 2016. An extensive reef system at the Amazon River mouth. Science Advances 2.

- Mulchrone, K.F., McCarthy, D.J., Meere, P.A., 2013. Mathematica code for image analysis, semi-automatic parameter extraction and strain analysis. Computers and Geosciences 61, 64-70.
- Nalin, R., Basso, D., Massari, F., 2006. Pleistocene coralline algal build-ups (coralligène de plateau) and associated bioclastic deposits in the sedimentary cover of Cutro marine terrace (Calabria, southern Italy). Geological Society, London, Special Publications 255, 11-22.
- NCOF, 2016. [http://www.ncof.co.uk/2G-Wave-Model-Description.html] Last Accessed: 5th April 2016.
- Nebelsick, J.H., Bassi, D., 2000. Diversity, growth forms and taphonomy: key factors controlling the fabric of coralline algae dominated shelf carbonates. Geological Society, London, Special Publications 178, 89-107.
- Nelson, W., D'Archino, R., Neill, K., Farr, T., 2014. Macroalgal Diversity Associated with Rhodolith Beds in Northern New Zealand. Cryptogamie, Algologie 35, 27-47.
- Nelson, W.A., 2009. Calcified macroalgae – critical to coastal ecosystems and vulnerable to change: a review. Marine and Freshwater Research 60, 787-801.
- Nelson, W.A., Neill, K., Farr, T., Barr, N., D'archino, R., Miller, S., Stewart, R., 2012. Rhodolith Beds in Northern New Zealand: Characterisation of Associated Biodiversity and Vulnerability to Environmental Stressors, New Zealand Aquatic Environment and Biodiversity Report No. 99. ISSN 1179-6480 (online) ISBN 978-0-478-40077-9 (online)
- Nicholas, A.P., 2001. Computational fluid dynamics modelling of boundary roughness in gravel-bed rivers: an investigation of the effects of random variability in bed elevation. Earth Surface Processes and Landforms 26, 345-362.
- Nikuradse, J., 1932. Laws of flow in rough pipes, (English translation, NACA Tech. Memo. 1292, Natl. Advis. Comm. For Aeron.,Washington D, .C., 1950.).
- Nolan, G., 2004. Observations of the seasonality in hydrography and current structure on the western Irish Shelf, PhD thesis, Oceanography. National University of Ireland, Galway, Ireland, 216pp.
- NPWS, 2013. National Parks and Wildlife Service, [http://www.npws.ie] Last Accessed: 05 April 2016.
- O'Connor, B., McGrath, D., Koennecker, G., Keegan, B.F., 1993. Benthic Macrofaunal Assemblages of Greater Galway Bay. Biology and Environment: Proceedings of the Royal Irish Academy 93B, 127-136.

- OPW, 2016. River Corrib flow historical data, Office of Public Works.
- Osborn, T., 2016. [https://crudata.uea.ac.uk/~timo/datapages/naoi.htm] Last Accessed: 5th April 2016.
- Paphitis, D., 2001. Sediment movement under unidirectional flows: an assessment of empirical threshold curves. Coastal Engineering 43, 227-245.
- Paphitis, D., Collins, M.B., Nash, L.A., Wallbridge, S., 2002. Settling velocities and entrainment thresholds of biogenic sands (shell fragments) under unidirectional flow. Sedimentology 49, 211-255.
- Peña, V., Bárbara, I., 2010. Seasonal patterns in the maërl community of shallow European Atlantic beds and their use as a baseline for monitoring studies. European Journal of Phycology 45, 327-342.
- Pope, N.D., Widdows, J., Brinsley, M.D., 2006. Estimation of bed shear stress using the turbulent kinetic energy approach—A comparison of annular flume and field data. Continental Shelf Research 26, 959-970.
- Porter-Smith, R., Harris, P.T., Andersen, O.B., Coleman, R., Greenslade, D., Jenkins, C.J., 2004. Classification of the Australian continental shelf based on predicted sediment threshold exceedance from tidal currents and swell waves. Marine Geology 211, 1-20.
- Pracht, M., Lees, A., Leake, B., Feely, M., Long, B., Morris, J., McConnell, B., 2004. Geology of Galway Bay: A geological description to accompany the bedrock geology 1:100,000 map series, sheet 14, Galway Bay. Geological Survey of Ireland (GSI), Dublin, 76pp.
- Pugh, D., Woodworth, P., 2014. Sea-Level Science: Understanding Tides, Surges, Tsunamis and Mean Sea-Level Changes. Cambridge University Press.
- Pugh, R.S., McCave, I.N., 2011. Particle size measurement of diatoms with inference of their properties: Comparison of three techniques. Journal of Sedimentary Research 81, 600-610.
- Pullin, A.S., 2002. Conservation Biology. Cambridge University Press, UK, 358pp.
- Quaranta, F., Tomassetti, L., Vannucci, G., Brandano, M., 2012. Coralline algae as environmental indicators: a case study from the Attard member (Chattian, Malta). Geodiversitas 34, 151-166.
- Ragazzola, F., Foster, L.C., Jones, C.J., Scott, T.B., Fietzke, J., Kilburn, M.R., Schmidt, D.N., 2016. Impact of high CO2 on the geochemistry of the coralline algae Lithothamnion glaciale. Scientific Reports 6, Article no. 20572, Nature Publications.
- Redjah, I., Olivier, F., Tremblay, R., Myrand, B., Pernet, F., Neumeier, U., Chevarie, L., 2010. The importance of turbulent kinetic energy on transport of juvenile clams (Mya arenaria). Aquaculture 307, 20-28.

- Reiss, H., Cunze, S., König, K., Neumann, H., Kröncke, I., 2011. Species distribution modelling of marine benthos: a North Sea case study. Marine Ecology Progress Series 442, 71-86.
- Ren, L., Nash, S., Hartnett, M., 2015. Observation and modeling of tide- and wind-induced surface currents in Galway Bay. Water Science and Engineering 8, 345-352.
- Rice, J., Arvanitidis, C., Borja, A., Frid, C., Hiddink, J.G., Krause, J., Lorance, P., Ragnarsson, S.A., Skold, M., Trabucco, B., Enserink, L., Norkko, A., 2012. Indicators for Sea-floor Integrity under the European Marine Strategy Framework Directive. Ecological Indicators 12, 174-184.
- Riosmena-Rodríguez, R., López-Calderón, J.M., Mariano-Meléndez, E., Sánchez-Rodríguez, A., Fernández-Garcia, C., 2011. Size and Distribution of Rhodolith Beds in the Loreto Marine Park: Their Role in Coastal Processes. Journal of Coastal Research 28:1, 255-260.
- Roden, C.M., Raine, R., 1994. Phytoplankton blooms and a coastal thermocline boundary along the West Coast of Ireland. Estuarine, Coastal and Shelf Science 39, 511-526.
- Sañé, E., Chiocci, F.L., Basso, D., Martorelli, E., In Press. Environmental factors controlling the distribution of rhodoliths: An integrated study based on seafloor sampling, ROV and side scan sonar data, offshore the W-Pontine Archipelago. Continental Shelf Research.
- Sanz-Lázaro, C., Belando, M.D., Marín-Guirao, L., Navarrete-Mier, F., Marín, A., 2011. Relationship between sedimentation rates and benthic impact on Maërl beds derived from fish farming in the Mediterranean. Marine Environmental Research 71, 22-30.
- Schmelter, M.L., Erwin, S.O., Wilcock, P.R., 2012. Accounting for uncertainty in cumulative sediment transport using Bayesian statistics. Geomorphology 175–176, 1-13.
- Sciberras, M., Rizzo, M., Mifsud, J.R., Camilleri, K., Borg, J.A., Lanfranco, E., Schembri, P.J., 2009. Habitat structure and biological characteristics of a maerl bed off the northeastern coast of the Maltese Islands (central Mediterranean). Marine Biodiversity 39, 251-264.
- Scoffin, T.P., 1988. Non-tropical shelf carbonates-modern and ancient The environments of production and deposition of calcareous sediments on the shelf west of Scotland. Sedimentary Geology 60, 107-124.
- Sheehan, E.V., Bridger, D., Attrill, M.J., 2015. The ecosystem service value of living versus dead biogenic reef. Estuarine, Coastal and Shelf Science 154, 248-254.
- Sheng, Y.P., 1989. Consideration of Flow in Rotating Annuil for Sediment Erosion and Deposition Studies. Journal of Coastal Research Special Issue 5, 207-216.
- Sherwood, C.R., Lacy, J.R., Voulgaris, G., 2006. Shear velocity estimates on the inner shelf off Grays Harbor, Washington, USA. Continental Shelf Research 26, 1995-2018.

- Shields, A., 1936. Application of Similarity Principles and Turbulence Research to Bedload Movement (English translation of an original German manuscript). Hydrodynamics Laboratory, California Institute of Technology, California, p. 47.
- Sides, E.M., Picton, B.E., Emblow, C.S., Morrow, C.C., Costello, M.J., 1994. Marine communities of Kilkieran Bay, the Aran Islands and the Skerd Rocks and an assessment of their nature conservation importance, National Parks and Wildlife Service.
- Smith, A.M., Cave, R.R., 2012. Influence of fresh water, nutrients and DOC in two submarine-groundwater-fed estuaries on the west of Ireland. Science of The Total Environment 438, 260-270.
- Smith, D.A., Cheung, K.F., 2003. Settling characteristics of calcareous sand. Journal of Hydraulic Engineering 129, 479-483.
- Smplayer, 2014. SMPlayer Media Software, Soundforge.
- Sørensen, O.R., Kofoed-Hansen, H., Rugbjerg, M., Sørensen, L.S., 2004. Third-generation spectral wave model (MIKE 21 SW) using an unstructured finite volume technique, in: McKee Smith, J. (Ed.), 29th International Conference on Coastal Engineering World Scientific, Lisbon, Portugal
- Soulsby, R.L., 1983. The bottom boundary layer of shelf seas in: Johns, B. (Ed.), Physical Oceanography of Coastal and Shelf Seas. Elsevier, Amsterdam, pp. 189-266.
- Soulsby, R.L., 1997. Dynamics of Marine Sands. Thomas Telford Publications, London. 249pp.
- Steller, D.L., Cáceres-Martínez, C., 2009. Coralline algal rhodoliths enhance larval settlement and early growth of the Pacific calico scallop Argopecten ventricosus. Marine Ecology Progress Series 396, 49-60.
- Steller, D.L., Foster, M.S., 1995. Environmental factors influencing distribution and morphology of rhodoliths in Bahía Concepción, B.C.S., México. Journal of Experimental Marine Biology and Ecology 194, 201-212.
- Steller, D.L., Foster, M.S., Riosmena-Rodríguez, R., 2009. Living rhodolith bed ecosystems in the Gulf of California., in: Johnson, J.M., Ledesma-Vázquez, L. (Eds.), Atlas of Coastal Ecosystems in the Gulf of California. Past and Present. University of Arizona Press, Tucson, Arizona pp. 72-82.
- Steneck, R.S., 1986. The Ecology of Coralline Algal Crusts: Convergent Patterns and Adaptative Strategies. Annual Review of Ecology and Systematics 17, 273-303.
- Stokes, G.G., 1851. On the effect of the internal friction of fluids on the motion of pendulums. Trans. Cambridge Philos. Soc. 9, 8-106.
- Strom, K., Keyvani, A., 2011. An explicit full-range settling velocity equation for mud flocs. Journal of Sedimentary Research 81, 921-934.
- Sutherland, W., Soulsby, R.L., 2011. Sediment Dynamics, in: Frostick, L.E., Mclelland, S.J., Mercer, T.G. (Eds.), Users Guide to Physical Modelling and Experimentation: Experience of the

HYDRALAB Network. IAHR Design Manual. CRC Press, pp. 67-125.
- Syvitski, J.P.M., 1991. Principles, methods, and application of particle size analysis. Cambridge University Press UK, 388pp.
- Taberner, C., Bosence, D.W.J., 1985. Ecological Succession from Corals to Coralline Algae in Eocene Patch Reefs, Northern Spain, in: Toomey, D.F., Nitecki, M.H. (Eds.), Paleoalgology: Contemporary Research and Applications. Springer Berlin Heidelberg, Berlin, Heidelberg, pp. 226-236.
- Thompson, C.E.L., Amos, C.L., Jones, T.E.R., Chaplin, J., 2003. The Manifestation of Fluid-Transmitted Bed Shear Stress in a Smooth Annular Flume-a Comparison of Methods. Journal of Coastal Research 19, 1094-1103.
- Thompson, C.E.L., Amos, C.L., Lecouturier, M., Jones, T.E.R., 2004. Flow deceleration as a method of determining drag coefficient over roughened flat beds. Journal of Geophysical Research: Oceans 109, C03001.
- Titschack, J., Nelson, C.S., Beck, T.I.M., Freiwald, A., Radtke, U., 2008. Sedimentary evolution of a Late Pleistocene temperate red algal reef (Coralligène) on Rhodes, Greece: correlation with global sea-level fluctuations. Sedimentology 55, 1747-1776.
- Van Der Meulen, A., 1988. Fall velocity of coral sand. Report Geopro 1988.01, Utrecht, the Netherlands.
- Van Rijn, L., 1993. Principles of Sediment Transport in Rivers, Estuaries and Coastal Seas, Aqua Publications, The Netherlands, p. 700.
- van Rijn, L.C., 2007a. Unified view of sediment transport by currents and waves. I: Initiation of motion, bed roughness, and bed-load transport. Journal of Hydraulic Engineering 133, 649-667.
- van Rijn, L.C., 2007b. Unified view of sediment transport by currents and waves. II: Suspended transport. Journal of Hydraulic Engineering 133, 668-689.
- van Rijn, L.C., 2007c. Unified view of sediment transport by currents and waves. III: Graded beds. Journal of Hydraulic Engineering 133, 761-775.
- Varoni, V.A., 1964. Measurements of critical shear stress for entraining fine sediments in a boundary layer. Keck Laboratory, Hydraulics Water Resources, California Institute Technology, p. 47.
- Wahl, T., 2000. Analysing ADV Data Using WinADV, Joint Conference on Water Resources Engineering and Water Resources Planning and Management, Minneapolis, Minnesota, p. 10.
- Warner, J.C., Sherwood, C.R., Signell, R.P., Harris, C.K., Arango, H.G., 2008. Development of a three-dimensional, regional, coupled wave, current, and sediment-transport model. Computers & Geosciences 34, 1284-1306.
- Weill, P., Mouazé, D., Tessier, B., Brun-Cottan, J.C., 2010. Hydrodynamic behaviour of coarse bioclastic sand from shelly cheniers. Earth Surface Processes and Landforms 35, 1642-1654.

- White, M., 1995. Tidal Dynamics of Galway Bay and associated 2-layer flow., in: Keegan, B.F., O'Connor, R. (Eds.), Irish Marine Science, Proceedings of Irish Marine Science Symposium. Galway University Press, Galway, Ireland.
- Wiberg, P.L., Sherwood, C.R., 2008. Calculating wave-generated bottom orbital velocities from surface-wave parameters. Computers & Geosciences 34, 1243-1262.
- Wiberg, P.L., Smith, J.D., 1987. Calculations of the critical shear stress for motion of uniform and heterogeneous sediments. Water Resources Research 23, 1471-1480.
- Wilcock, P.R., 1996. Estimating Local Bed Shear Stress from Velocity Observations. Water Resources Research 32, 3361-3366.
- Wilcock, P.R., 2001. Toward a practical method for estimating sediment-transport rates in gravel-bed rivers. Earth Surface Processes and Landforms 26, 1395-1408.
- Wilkinson, R.H., 1983. A method for evaluating statistical errors associated with logarithmic velocity profiles. Geo-Marine Letters 3, 49-52.
- Wilson, S., Blake, C., Berges, J.A., Maggs, C.A., 2004. Environmental tolerances of free-living coralline algae (maerl): implications for European marine conservation. Biological Conservation 120, 279-289.
- Winterwerp, J.C., Kranenburg, C., 2002. Fine Sediment Dynamics in the Marine Environment. Elsevier Science.
- Woelkerling, W., Irvine, L., Harvey, A., 1993. Growth-forms in Non-geniculate Coralline Red Algae (Coralliinales, Rhodophyta). Australian Systematic Botany 6, 277-293.
- Wolfman, 2013. Component Measurements Tools Guide. Wolfman Mathematica 9 documentation centre, Wolfman Research Available at [http://reference.wolfram.com/language/ref/ComponentMeasurements.html].
- Yang, Z., Baptista, A., Darland, J., 2000. Numerical modeling of flow characteristics in a rotating annular flume. Dynamics of Atmospheres and Oceans 31, 271-294.
- Young, I.R., 1999. Wind Generated Ocean Waves. Elsevier, Amstedam, 287pp.
- Yu, J., Henrys, S.A., Brown, C., Marsh, I., Duffy, G., 2015. A combined boundary integral and Lambert's Law method for modelling multibeam backscatter data from the seafloor. Continental Shelf Research 103, 60-69.